

Heterogeneous Flow in Interstellar Medium and Star Formation

by

Shule Li

A dissertation submitted to University of Rochester in conformity with the
requirements for the degree of Doctor of Philosophy.

Rochester, New York

August, 2014

© Shule Li 2014

All rights reserved

Abstract

Interfaces between hot and cold magnetized plasmas exist in various astrophysical contexts, for example where hot outflows impinge on an ambient interstellar medium (ISM). It is of interest to understand how the structure of the magnetic field spanning the interface affects the temporal evolution of the temperature gradient. Here we explore the relation between the magnetic field topology and the heat transfer rate by adding various fractions of tangled vs. ordered field across a hot-cold interface allow the system to evolve to a steady state. We find a simple mathematical relation for the rate of heat conduction as a function of the initial ratio of ordered to tangled field across the interface. We discuss potential implications for the astrophysical context of magnetized wind blown bubbles (WBB) around evolved stars.

We study the interaction of strong shock waves with magnetized clumps. Previous numerical work focused on the simplified scenario in which shocked clumps are immersed in a globally uniform magnetic field that extends through both the clump and the ambient medium. Here we consider the complementary circumstance in which the field is completely self-contained within the clumps. This could arise naturally during clump formation via dynamical or thermal instabilities for example as magnetic field pinches off from the ambient medium. Using our AMR MHD code AstroBEAR, we carry out a series of simulations with magnetized clumps that have different self-contained magnetic field configurations. We find that the clump and magnetic evolution are sensitive to the fraction of magnetic field aligned with versus perpendicular to the shock normal. The relative strength of magnetic pressure and tension in the different field configurations allows us to analytically understand the

different cases of post-shock evolution. We also show how turbulence and the mixing it implies depends of the initial field configuration and suggest ways in which observed shock-clump morphology may be used as a proxy for identifying internal field topologies a posteriori.

Star formation can be triggered by compression from wind or supernova driven shock waves that sweep over molecular clouds. Because these shocks will likely contain processed elements, triggered star formation has been proposed as an explanation for short lived radioactive isotopes (SLRI) in the Solar System. Previous studies have tracked the triggering event to the earliest phases of collapse and have focused on the shock properties required for both successful star formation and mixing of SLRI's. In this paper, we use Adaptive Mesh Refinement (AMR) simulation methods, including sink particles, to simulate the full collapse and subsequent evolution of a stable Bonnor-Ebert sphere subjected to a shock and post-shock wind. We track the flow of the cloud material after a star (a sink particle) has formed. For non-rotating clouds we find robust triggered collapse and little bound circumstellar material remaining around the post-shock collapsed core. When we add initial cloud rotation we observe the formation of disks around the collapsed core which then interact with the post-shock flow. Our results indicate that these circumstellar disks are massive enough to form planets and are long-lived, in spite of the ablation driven by post-shock flow ram pressure. As a function of the initial conditions, we also track the time evolution of the accretion rates and particle mixing between between the ambient wind and cloud material. The latter is maximized for cases of highest mach number.

Contents

Abstract	ii
List of Figures	vi
List of Tables	x
1 Introduction	1
2 AstroBEAR: Parallel MHD Code with Adaptive Mesh Refinement and Multiphysics	8
2.1 Brief Introduction of AstroBEAR	8
2.2 Multiphysics: Radiative Cooling and Thermal Conduction	10
2.3 Multiphysics: Self Gravity and Sink Particles	12
2.4 Multiphysics: Non-ideal MHD: Resistivity	13
3 Multiphysics Tests	18
3.1 Test of MHD Heat Conduction	18
3.2 Test of Self Gravity with Sink Particle	23
3.3 Test of Resistive MHD	23
4 Magnetized Thermal Conduction in Wind Blown Bubbles	26
4.1 Introduction	26
4.2 Problem Description and Analytical Model	28
4.3 Simulation Setup	31
4.4 Simulation Results	35
4.5 Discussion	40
4.6 Concluding Remarks	50
5 MHD Shock-Clump Evolution with Self-Contained Magnetic Fields	53
5.1 Introduction	53
5.2 Problem Description and Simulation Setup	56
5.3 Simulation Results	63

5.3.1	Shocked clumps with a self-contained strong ordered field . . .	63
5.3.2	Shocked clumps with a weak self-contained ordered field . . .	69
5.4	Mathematical Model and Analysis	77
5.4.1	Modeling the Compression Phase	80
5.4.2	Expansion Phase	84
5.4.3	Geometrical Factor of Magnetic Repelling Force α	85
5.4.4	Correction in the Shape Factor e	86
5.4.5	Mixing of Clump and Ambient Material	88
5.5	Concluding Remarks	90
6	Triggered Star Formation	92
6.1	Introduction	92
6.2	Initial Simulation Setup	95
6.3	Simulation Results	97
6.4	Quantitative Discussion	102
6.4.1	Triggering time	102
6.4.2	Asymptotic Stellar Mass	103
6.4.3	Accretion Rates	104
6.4.4	Circumstellar Bound Mass and Disk Survival	106
6.5	Concluding Remarks	107
7	Resistive Shock-clump interaction and its Lab Astrophysics Implication	109
7.1	Introduction	109
7.2	Initial Setup	110
7.3	Results for Constant Magnetic Reynolds Number	112
7.4	Results for Realistic Resistivity	116
7.5	Concluding Remarks	117
8	Summary	121
8.1	Numerics	121
8.2	Magnetic Field Regulated Heat Conduction Through Hot-cold Interfaces	124
8.3	Shock-clump interaction with contained magnetic field	125
8.4	Triggered Star Formation	126
8.5	Resistive Shock-clump interaction	129
8.6	Concluding Remarks	131

List of Figures

2.1	computation stencil for diffusive current and magnetic field calculation.	16
3.1	Field line evolution of magneto-thermal instability. (a): initial state. (b): $t = 75\tau_s$. (c): $t = 150\tau_s$. (d): $t = 250\tau_s$.	19
3.2	(a): $\ln v_y$ against evolution time in τ_s . (b): calculated growth rate against evolution time in computational units. Initially the growth rate is stable around the theoretical value 0.4 and then decreases sharply after $t = 200$, which indicates the evolution has entered the nonlinear regime.	20
3.3	(a): evolution of mean kinetic energy. (b): evolution of mean magnetic energy.	21
3.4	Density and magnetic field distribution for Sweet-Parker test.	24
3.5	Normalized kinetic energy and magnetic field distribution for Sweet-Parker outflow.	25
4.1	The initial and steady state field configuration. (a): the initial field forms complete loops that only allows heat transfer within the interaction region. (b): the steady state field reconnects itself so that it allows heat transfer between regions deeply into the hot and cold areas.	30
4.2	Evolution of temperature distribution with $R = 0.0$. The cuts are at (a): $t = 0.0$, the initial state, (b): $t = 0.4$, (c): $t = 0.8$, (d): $t = 1.2$, the steady state.	36
4.3	Evolution of density distribution with $R = 0.0$. The cuts are at (a): $t = 0.0$, the initial state, (b): $t = 0.4$, (c): $t = 0.8$, (d): $t = 1.2$, the steady state.	37
4.4	Evolution of temperature distribution with $R = 0.4$. The cuts are at (a): $t = 0.0$, the initial state, (b): $t = 0.4$, (c): $t = 0.8$, (d): $t = 1.2$, the steady state.	38
4.5	Evolution of temperature distribution with $R = 1.0$. The cuts are at (a): $t = 0.0$, the initial state, (b): $t = 0.4$, (c): $t = 0.8$, (d): $t = 1.2$, the steady state.	39

4.6	Evolution of mean cut temperature averaged on y direction with different R values labeled by different colors. The cuts are at (a): $t = 0.0$, the initial state, (b): $t = 0.4$, (c): $t = 0.8$, (d): $t = 1.2$, the steady state.	41
4.7	(a) top left: time evolution of mean heat flux at the interface, (b) top right: time evolution of average temperature difference between the hot and cold regions, (c) bottom left: time evolution of interface width, (d) bottom right: time evolution of the mean value of $ \nabla \times \mathbf{B} $.	42
4.8	(a) Comparison of averaged heat flux for situation with field loops filling up the entire domain and situation with field loops only fill the interaction region. (b) Comparison of averaged heat flux for situations with different tangled field length scale.	44
4.9	(a) Comparison on evolution of local field energy in terms of B_x and B_y . Circles corresponds to the $B_x^2/2$ curve, stars corresponds to the $B_y^2/2$ curve. The different colors denote various R values. (b) Eccentricity of the ellipses constructed by assigning the mean values of local $ B_x $ and $ B_y $ to the major and minor axes, respectively. The set of curves show different evolution patterns for different R values.	46
4.10	heat transfer rate observed in the simulation compared with the analytic model.	48
5.1	The initial setup of the clump simulations. The actual domain is four times as long on x as on y and z. The upcoming planar shock is at the left edge of the domain, propagating rightward along the x axis. The stripes on the clump surface denote a self-contained toroidal magnetic field with its axis aligned with x axis inside the clump.	57
5.2	The initial setup of the clump magnetic field. The actual domain is four times as long on x as on y and z. The first letter denotes the field configuration: T for toroidal only; P for poloidal only. The second letter denotes the field orientation with respect to the shock propagation direction: A for aligned; P for perpendicular. The blue arrow denotes the shock direction.	60
5.3	Case of strong toroidal only, aligned with shock normal. Evolution of clump material at 1, 2 and 3.5 clump crushing time. The color indicates clump material concentration, normalized by initial value.	66
5.4	Case of strong toroidal only, perpendicular to shock propagation direction. Evolution of clump material at 1, 2 and 3.5 clump crushing time. The color indicates clump material concentration, normalized by initial value.	67
5.5	Case of strong poloidal only, aligned with shock normal. Evolution of clump material at 1, 2 and 3.5 clump crushing time. The color indicates clump material concentration, normalized by initial value.	70

5.6	Case of strong poloidal only, perpendicular to shock propagation direction. Evolution of clump material at 1, 2 and 3.5 clump crushing time. The color indicates clump material concentration, normalized by initial value.	71
5.7	Case of weak toroidal only, perpendicular to shock propagation direction. Evolution of clump material at 1, 2 and 3.5 clump crushing time. The color indicates clump material concentration, normalized by initial value.	73
5.8	Case of weak toroidal only, perpendicular to shock propagation direction. Evolution of clump material at 1, 2 and 3.5 clump crushing time. The color indicates clump material concentration, normalized by initial value.	74
5.9	Case of weak poloidal only, aligned with shock normal. Evolution of clump material at 1, 2 and 3.5 clump crushing time. The color indicates clump material concentration, normalized by initial value.	75
5.10	Case of weak poloidal only, perpendicular to shock propagation direction. Evolution of clump material at 1, 2 and 3.5 clump crushing time. The color indicates clump material concentration, normalized by initial value.	76
5.11	Snapshot of shocked clumps cutthrough the center of the domain, at $t = 2.5\tau_{cc}$, for the TAW and PAW cases. The upper panel corresponds to the density, the lower panel corresponds to $1/\beta$	77
5.12	Snapshot of shocked clumps cutthrough the center of the domain, at $t = 2\tau_{cc}$. The four panels correspond to the TA, TP, PA, PP cases from top to bottom, respectively. The upper half part of each panel shows the clump density, the lower half part shows the magnetic pressure in pseudocolor.	78
5.13	Global quantities of the strong self-contained field case: (a) Time evolution of kinetic energy contained in the clump material in computation units, indicating how much energy has transferred from wind into clump. (b) Time evolution of total magnetic energy.	79
5.14	Global quantities of the weak self-contained field case: (a) Time evolution of kinetic energy contained in the clump material in computation units, indicating how much energy has transferred from wind into clump. (b) Time evolution of total magnetic energy.	79
5.15	Wind-clump mixing ratio for the strong self-contained field case: (a) at τ_{cc} . (b) at $3\tau_{cc}$. The color codings and their corresponding simulations are labeled in the plot	89
5.16	Wind-clump mixing ratio for the weak self-contained field case: (a) at τ_{cc} . (b) at $3\tau_{cc}$. The color codings and their corresponding simulations are labeled in the plot	89

6.1	Column Density Evolution for Case R1: (a) 0.3 million yrs; (b) 0.5 million yrs; (c) 0.85 million yrs	99
6.2	Post-triggering evolution at 0.6 million years: (a) Case N; (b) Case N'; (c) Case R1; (d) Case R2.	100
6.3	Case R1: 3D volume rendering of the disk formed by triggering at 0.6 million years.	101
6.4	Time Evolution of Stellar Mass, Accretion Rate, Wind Material Mixing Ratio and Bound Mass	102
7.1	Initial setup for shock-clump interaction with Spitzer resistivity. (a) density distribution, (b) temperature distribution with radiation pre-heating.	113
7.2	Shocked behavior of the target with horizontal magnetic field at different magnetic Reynolds number R_m as marked.	114
7.3	Shocked behavior of the target with vertical magnetic field at different magnetic Reynolds number R_m as marked.	114
7.4	Shocked behavior of the target with vertical magnetic field and Spitzer resistivity at different magnetic β	118
7.5	Shocked behavior of wire (top down). The wire has 20A surface current running out of the plane. This produces a toroidal magnetic field around $20T$ at the wire surface. Top: non-magnetized; bottom: magnetized. The magneto-pause is caused by the shifting of the stagnation point by magnetic pressure.	120
8.1	Realistic supernova blast wave structure. Red: density; Green: velocity; Blue: temperature.	128

List of Tables

4.1	Scaling of Simulation Parameters	51
5.1	Simulation Setups	59
6.1	Simulation Setups	96

Chapter 1

Introduction

Supersonic flows are common throughout the universe, and the shock waves they produce play key roles in shaping the structure and evolution of astronomical objects on both large and small scales. Magnetic field, as well as other multiphysics processes such as radiative cooling and heat conduction, are important in determining the forming and the evolution of structures such as hot-cold interfaces, clumps and jets. Blast wave from supernova is believed to be powering the forming of star clusters such as Eta Carinae, Cygnus loop, and so on. For interstellar flows, it is usually the case that the flow itself carries complicated density, temperature and magnetic structures. For instance, radiative cooling results in fragmented shells in supernova blast wave that is considerably colder and denser than the wind behind it, interstellar shocks travelling through clumpy regions in a molecular cloud carry with them density inhomogeneities in the form of clumps with inherent magnetic field structure on the length scales comparable or smaller than that of the clumps. These flows can be named in general as interstellar heterogeneous flows because of their structural inhomogeneity. It is important to study these flows numerically as they result in numerous observable phenomena that give clue to many grand challenge problems of astrophysics. One example being the observed structures of young stellar objects (YSO), another being star formation efficiency of shock triggered star forming region.

The computational astrophysics group at University of Rochester has developed a parallel MHD code AstroBEAR with adaptive mesh refinement (AMR), which allows

efficient distribution of computation resources to resolve most desired features from an Eulerian grid simulation. As part of the thesis work involves developing features for AstroBEAR, in chapter 2, we briefly walkthrough the key features developed that will be used in the simulations presented in later chapters. It has been the recent trend to look into multiphysics details of complex processes in the field of numerical astrophysics. Many important problems have demonstrated themselves to be only meaningful when such physics processes beside ideal MHD are considered. One example being the star formation problem in which the self gravitational force of the interstellar gas is essential to allow collapse to happen. In AstroBEAR, we model various multiphysics processes using operator-splitting method: a method in which the multiphysics solver is separated from the ideal MHD solver. Chapter 2 gives an indepth look into the multiphysics components of AstroBEAR: section 2.2 discusses cooling and heating effects, section 2.3 discusses self gravity and sink particle, section 2.4 discusses resistivity in non-ideal MHD.

In this thesis, we harness the power of the parallel AMR MHD capability of AstroBEAR, to study some of the properties of heterogeneous flows of interest. One of such problem is the thermal conduction through interfaces between hot and cold plasmas. The motivating example of such an object occurs in wind blown bubbles (WBB) of evolved stars where magnetized hot supersonic outflow shock heats the cooler ambient magnetized interstellar medium. In such a scenario, the heat flow carried by the electrons are usually confined to be only along the magnetic field lines due to the relatively small electron gyro-radius with respect to the electron mean free path. Such heat flux regulated by magnetic field may be used to explain the lower than expected shell temperature from observations such as Zhekov et al 1998 and Imamura et al 2000. Zhekov et al 2000 has done pioneering work on the subject of WBB heating, as they found the heating rate of the WBB shell under spherical symmetric hydrodynamics simulations to be higher than expected. However, as evidenced by previous research such as Blackman et al 2009, magnetized gas has considerably different heating property based on the regulated heat conduction. It is then possible to explain the low heat transfer efficiency between the cold shell and the hot reservoir by including magnetic field.

A second example is the unexpected slow mass deposition rate of the cooling flows in some galaxy cores which might be inhibited by a restricted thermal conduction (Rosner & Tucker (1989), Balbus & Reynolds (2008), Mikellides et al. (2011)). In the intracluster medium (ICM), the tangled magnetic field can potentially produce a strongly anisotropic thermal conductivity that may significantly influence temperature and density profiles (Chandran & Maron (2004); Maron et al. (2004); Narayan & Medvedev (2001), Mikellides et al. (2011)).

In our WBB study, we set up simulations of hot bubble-cold shell with tangled magnetic field that has a length scale smaller than that of the interface itself. We focus on the impact of magnetic field regulation on the heat flux, and the possibility of a slow-down effect on the heating of the shell as a result of magnetic field geometry. The thermal conduction solver is described in detail in Section 2.2, the test for thermal conduction solver is discussed in Section 3.1. The thermal conduction through magnetized hot cold interfaces as those in WBB is discussed in chapter 4.

Within our own galaxy, matter overabundances are found in molecular clouds, and within these clouds matter further is distributed unevenly in the star-forming regions known as molecular cloud cores. Clumps of material exist on smaller scales as well. This heterogeneous distribution of matter is required, of course, for star and planet formation. On the other hand, energetic sources such as YSOs, planetary nebulae (PNe), and supernovae inject kinetic energy back into their environments in the form of winds, jets, and shocks. On larger cosmological scales galaxies are clustered implying the early evolution of the Universe involved heterogeneous or "clumpy" flows as well. The central regions of active galaxies with their supermassive blackholes are also expected to be home to extensive regions of heterogeneous density distributions with strong incident winds and shocks. Thus understanding how the former (clumps) and latter (winds, jets, and shocks) interact remains a central problem for astrophysics. Since dynamically significant magnetic fields are expected to thread much of the plasma in the interstellar and intergalactic medium the role of magnetic forces on shock clump interactions is also of considerable interest. Earlier studies have focused on the problem of uniform magnetic field extending through the entire space, where magnetic field is found to be important in determining the shocked morphology of the

clumps as in Maclow et al 1994, Jones et al 1996. However, magnetic field with length scale comparable to the clumps are observed in many situations, Herbig-Haro (HH) objects for instance, are believed to contain non-uniform, tangled magnetic field on small length scale. Furthermore, the magnetized clump objects can now be produced in laboratory astrophysics (Lebedev et al 2012), as the lab astrophysical magnetized jets produced on MAGPIE contains small scale clumpy regions, whose mechanism is related to magnetic tower launching (Huarte-Espinosa et al 2012, Lebedev et al 2012). The magnetic structure inside the clump can significantly change the evolution of the shocked behavior compared to the uniform field cases: as the stretch of the uniform field plays a key role in determining the shocked clump morphology, such stretch may not be present in the contained field scenario. The uniform field studies also oversimplifies the importance of the field geometry inside the clump. Intuitively, simple confined magnetic field configurations as pure toroidal or poloidal give significantly different field pressure and tension distribution throughout the clump, which will likely alter the response to the incoming shock. In chapter 5, we present simulations with various magnetic field geometry contained inside the clump, with mathematical models that help us predict the shocked behavior of such magnetized clumps.

The problem of star formation is one of the grand challenge problems in theoretical astrophysics. Stars can be formed from a variety of mechanism, such as gravitational instabilities in molecular cloud. One of such mechanism is shock triggering: when shock from a supernova blast wave or AGB wind runs through globules that are otherwise in gravitational hydrodynamic equilibrium, collapse can be triggered by the compression from shock (Boss et al 1998). The shock triggering mechanism has one key consequence different from instability triggering, as it allows exotic elements processed through supernova blast to be injected into the formed star and its stellar surroundings. This opens opportunity to explain the relatively high dilution ratio (defined as the observed element number density) of short-lived radioactive isotopes (SLRI) found in the Solar System: about 10^{-3} in terms of dilution ratio according to observational studies such as Takahashi et al 2008. It is not realistic to expect such high dilution ratio can be entirely self-produced through collapse mechanism such as gravitational instabilities. However, if triggered star formation is assumed, it is

possible to trigger the collapse of a globule of about $1M_{\odot}$ to form a star while injecting exotic material from the post shock wind at the same time. Boss et al 2008 and Boss et al 2010 have studied the requirement of the shock speed and thickness to allow such collapse and injection to happen at the same time. The most important conclusion from their series of studies on this subject is that when shock speed and thickness are “correctly tuned”, the successful triggering and injection can happen at the same time. In their previous studies, Boss et al do not follow the evolution of collapse till the formation of the star. Such subsequent evolution can be important especially if one wants to answer the question of whether disk formation is possible in a triggered scenario, as well as how much post shock material can be injected into the disk. Another unanswered question is the importance of the structure of the blast wave as the shock-wind structure used in the series of papers by Boss et al are not what people expect from theoretical studies on supernova blast wave structures. Finally, the importance of the magnetic field in such scenario is almost entirely new territory. It is intuitively more plausible to consider MHD instead of pure hydrodynamics as the shocked globules are likely highly magnetized. In section 2.3, we present the self gravity and sink particle treatment in AstroBEAR. In section 3.2, we present the numerical tests for self gravity and sink particle solvers. In chapter 6, we use the sink particle capability of AstroBEAR2.0 to study for the first time the shock-induced triggering of a stable Bonnor-Ebert cloud following the long-term evolution of the flow after a star has formed. We confirm that under certain shock conditions, star can be formed during such triggering. We track the subsequent flow pattern after the triggering event, and demonstrate that with initial clump rotation, disk formation is possible during triggering.

Laboratory astrophysics has become an integral part of astrophysics study. Researchers are now able to produce targets in laboratory environments that are scalable to real astrophysics objects, such as stellar jets and accretion disks (Lebedev et al 2010). The shock-clump interaction model has become one of the showcasing problem in lab astrophysics because of its broad relevance: many important problems can be casted as a shock-clump interaction problem. The shock-clump problem spawns many subproblems which can be readily studied in the lab by changing the setup or

target, such as the shocked behavior of multiple clumps (Hartigan et al 2009), the importance of magnetic fields (Hartigan et al 2013), the shocked behavior of pillars, and so on. Such laboratory efforts tie back to many numerical studies on shocked clumps that can be traced back to the 1970s (refs here). Our group collaborates with Lab of Laser Energetics (LLE) to explore the problem of magnetized shock-clump interaction on both experimental and numerical fronts. Magnetic fields generated in the MIFEDS system have now reached a strength where fields in the postshock gas should be strong enough to influence the flow dynamics. Experiments of shocked magnetized clumps at LLE will open the door to this complex, exciting, and astrophysically relevant world of magnetized shocks by providing the first important tests of both experimental and astrophysical numerical codes in the 3-D MHD regime. In order to relate the MHD shock-clump simulations to the experiments, one significant drawback of the existing numerical simulations on MHD shocked clumps is that the resistivity is not taken into consideration. While this may be a valid assumption under astrophysical environments as the magnetic Reynolds number $R_m = VL/\eta$, where V and L are the typical flow speed and length scale, and η is the magnetic diffusivity, satisfies $R_m \gg 1$ as the length scale is large. In addition, in the astrophysical environment of shock-clump interaction, the post shock flow is usually in very high temperature region which renders η extremely low based on Spitzer relation $\eta \propto T^{-3/2}$. However, the laboratory astrophysics usually involves resistivity of the instruments/plasma that cannot be ignored under a much smaller length scale. While there have been numerous studies that implements multiphysics processes in such MHD problem, such as Fragile et al 2005 with radiative cooling, Orlando et al 2010 with thermal conduction, there has been no previous study that explores the effects of magnetic diffusion. To tackle the problem of non-ideal MHD shock-clump interaction, and to provide guidance to the design of lab instrumentation, we have run simulations on 3-D MHD clumps with global uniform magnetic field with both ideal and resistive MHD (non-trivial magnetic Reynolds number) and demonstrated that the resistivity is indeed an important factor when designing such an experiment. The resistive solver is one of the key multiphysics components of AstroBEAR. We have done Sweet-Parker problem and magnetic island formation problem to demon-

strate it's working in AMR (Section 3.3). The resistive MHD solver is described in section 2.4, the Sweet-Parker test of AstroBEAR is discussed in chapter 3.3 and the non-ideal MHD shock-clump interaction simulations are presented in chapter 7.

Chapter 2

AstroBEAR: Parallel MHD Code with Adaptive Mesh Refinement and Multiphysics

2.1 Brief Introduction of AstroBEAR

For simulations discussed in this thesis work, we use the AstroBEAR 2.0 code, developed in-house by the computational astrophysics group. AstroBEAR is a magnetohydrodynamics code with multi-physics capabilities that include self-gravity, non-ideal equation of state (EOS), and micro-physics such as heat conduction, resistivity and radiation transfer. AstroBEAR is parallelized to run on modern architectures with dedicated resources for scientific computing. AstroBEAR has shown excellent scaling up to tens of thousands of processors on major computation clusters since version 2.0, and has been featured as core part in many research papers published by the group as well as its collaborators. As the computational aspect comprises an integral part of the thesis research, we present here some of the key features that are developed for version 2.0 that are used in the thesis research.

Adaptive Mesh Refinement (AMR), has become increasingly important in computational astrophysics nowadays. AMR allows researchers to vary resolution (number of computation zones per unit length) in one computation grid, thus able to focus

resources on points of interest. This allows a much greater dynamic range for the computation than fixed grid: for example, in star formation simulation, one may have a star formation simulation that has hundreds of stars formed in one computation grid while still have high enough resolution around the vicinity of each star to resolve accretion flow. In shock-clump simulations, one may have highly resolved clump surface and downstream instability pattern while keep the total running time reasonable.

The AstroBEAR code is a parallel AMR Eulerian hydrodynamics code with capabilities for MHD in two- and three-dimensions. Further details on AstroBEAR may be found in Cunningham et al (2009), Carroll-Nellenback et al (2013) and at <https://clover.pas.rochester.edu/trac/astrobear>. Besides the several schemes of varying order available for the user to solve the ideal MHD equations, it also employs implicit and explicit matrix solvers to solve multiphysics problems such as self gravity and heat conduction by operator splitting.

For the ideal MHD, AstroBEAR solves the following equations based on exact or approximate Riemann solver based on user choice, with second or third order reconstruction scheme such as Godunov method or piecewise linear method, along with constrained transport to enforce divergence free condition:

$$\frac{\partial \rho}{\partial t} + \nabla \cdot (\rho \mathbf{v}) = 0, \quad (2.1)$$

$$\frac{\partial(\rho \mathbf{v})}{\partial t} + \nabla \cdot [\rho \mathbf{v} \mathbf{v} + (p + \frac{B^2}{8\pi})\mathbf{I} - \frac{\mathbf{B}\mathbf{B}}{4\pi}] = 0, \quad (2.2)$$

$$\frac{\partial \mathbf{B}}{\partial t} + \nabla \times (\mathbf{v} \times \mathbf{B}) = 0, \quad (2.3)$$

$$\frac{\partial E}{\partial t} + \nabla \cdot [\mathbf{v}(E + p + \frac{B^2}{8\pi}) - \frac{\mathbf{B}(\mathbf{B} \cdot \mathbf{v})}{8\pi}] = 0, \quad (2.4)$$

where ρ , n , \mathbf{v} , \mathbf{B} and p are the density, particle number density, velocity, magnetic field, and pressure, and E denotes the total energy density given by

$$E = \epsilon + p \frac{\mathbf{v} \cdot \mathbf{v}}{2} + \frac{\mathbf{B} \cdot \mathbf{B}}{8\pi}, \quad (2.5)$$

where the internal energy ϵ is given by

$$\epsilon = \frac{p}{\gamma - 1} \quad (2.6)$$

For the simulations presented in this thesis, we choose to solve the fluid equations with the MUSCL (Monotone Upstream-centered Schemes for Conservation Laws) primitive method using TVD (Total Variation Diminishing) preserving Runge-Kutta temporal interpolation. The magnetic field equation is solved on the basis of electromotive force (emf) and subject to constrained-transport algorithm to keep the divergence-free property.

2.2 Multiphysics: Radiative Cooling and Thermal Conduction

The energy equation in the previous section maybe modified when cooling or heating process is involved. With radiative cooling, the energy equation 2.4 should change to the following form:

$$\frac{\partial E}{\partial t} + \nabla \cdot [\mathbf{v}(E + p + \frac{B^2}{8\pi}) - \frac{\mathbf{B}(\mathbf{B} \cdot \mathbf{v})}{8\pi}] - \Lambda(n, T) = 0, \quad (2.7)$$

We denote the radiative cooling by a function of number density and temperature: $\Lambda(\rho, T)$. In our simulations, we implement the Dalgarno McCray cooling table as it is more realistic comparing to simple analytic cooling functions [Dalgarno & McCray (1972)]. The gas is allowed to cool to a floor temperature and then cooling is turned off. For chapter 5, we define our parameter regime as “weakly cooling” so that the region inside the clump can get cooled and hold up together but the dynamics will be mostly come from the interaction between the incoming shock and the self-contained magnetic field. This means that we require the cooling time scale behind the transmitted shock to be smaller than the clump crushing time scale by a factor of less than 10. As we are more interested in the dynamics of the interaction mentioned above, the employment of a different cooling table or cooling floor temperature will result in similar conclusions if the “weakly cooling” assumption is maintained.

With thermal conduction, we assume that the heat flux is confined to be parallel to the magnetic field lines. This assumption applies only when the ratio of electron gyro-radius to field gradient scales is small. Under this assumption, the heat flux

parallel to field lines can be written as

$$Q = -\kappa_{\parallel}(\nabla T)_{\parallel}, \quad (2.8)$$

where the subscript \parallel indicates parallel to the magnetic field, and κ_{\parallel} is the classical Spitzer heat conductivity: $\kappa_{\parallel} = \kappa_c T^{2.5}$, with $\kappa_c = 2 \times 10^{-18} \text{ cm s g}^{-1} \text{ K}^{-2.5}$. We take κ_{\parallel} to be a constant throughout our simulations and so hereafter write it simply as κ . With the added thermal conduction, we change the energy equation to the following form:

$$\frac{\partial E}{\partial t} + \nabla \cdot [\mathbf{v}(E + p + \frac{B^2}{8\pi}) - \frac{\mathbf{B}(\mathbf{B} \cdot \mathbf{v})}{8\pi}] + \nabla \cdot Q = 0, \quad (2.9)$$

In the implicit solver, we convert equation 2.7 to an operator splitted form on temperature:

$$nk_B \frac{\partial T}{\partial t} + \nabla \cdot Q = 0, \quad (2.10)$$

where number density n is assumed to be time independent during the implicit thermal conduction step. Note that from equation 2.8, we know that equation 3.5 can be solved by finite differencing to obtain a temperature distribution $T(\mathbf{x}, t)$. The difficulty in explicit solver mainly comes from the fact that Q depends on the second order differentiation of T , which results in a dependence of $\Delta t \propto \Delta x^2$ from stability requirement: the explicit time step is a quadratic function on the grid resolution. This leads to unreasonably small time steps for simulations with high resolutions. For the implicit solver, however, we modify the stability requirement to a physical requirement since it is unconditionally stable numerically: $\Delta t \propto (\nabla Q)^{-1}$ where ∇Q can be computed on each zone face. The physical requirement constrains the simulation code to take cautious time steps so that change of temperature gradient is properly resolved.

For constant heat conduction as used in chapter 4, equation 3.5 can be solved by turning it directly into the finite difference form, and compute the matrix as well as the right hand side vector elements. The matrix and the right hand side vector is then input into the linear solver package HYPRE, to obtain a solution under certain numerical tolerance (10^{-6} for the simulations presented in chapter 4).

Nonlinear heat conduction where $\kappa = T^{2.5}$, it is impossible to turn equation 3.5 into a linear system without approximations. In AstroBEAR, we implement Crank-Nicholsson scheme in which any nonlinear function in T is turned into a linear function by Taylor expanding such function to the first order. The unknown T only appears in linear term after the approximation, while its Taylor coefficients may involve nonlinear terms of T from a previous time step.

2.3 Multiphysics: Self Gravity and Sink Particles

With self-gravity, the momentum and energy equations 2.2 and 2.4 change to the following form:

$$\frac{\partial(\rho\mathbf{v})}{\partial t} + \nabla \cdot [\rho\mathbf{v}\mathbf{v} + (p + \frac{B^2}{8\pi})\mathbf{I} - \frac{\mathbf{B}\mathbf{B}}{4\pi}] = -\rho\nabla\phi, \quad (2.11)$$

$$\frac{\partial E}{\partial t} + \nabla \cdot [\mathbf{v}(E + p + \frac{B^2}{8\pi}) - \frac{\mathbf{B}(\mathbf{B} \cdot \mathbf{v})}{8\pi}] = -\rho\mathbf{v} \cdot \nabla\phi, \quad (2.12)$$

where ϕ denotes the gravitational potential of the gas. At each step of simulation, we solve ϕ based on the source function from the density distribution:

$$\nabla^2\phi = 4\pi G\rho. \quad (2.13)$$

ϕ is then fed into equations ?? and ?? as an external source term. Equation 2.13 is solved implicitly using linear solver package HYPRE developed by Lawrence Livermore National Lab, which incorporates parallel AMR grid. Multiple linear solvers and preconditioners are available in the HYPRE package, in the simulations of this thesis, we choose to use the PCG solver whenever such linear solver is required.

When treating collapse problems, it is sometimes convenient to abstract a dense, collapsing region as a particle separated from the gas in the computation grid. This treatment allows us to treat such region as a point gravity object that can accrete gas from its surroundings while remain in momentum and energy exchange with its surrounding gas. The facility of sink particle is a way to approximate star forming regions without resolving extremely small Jean's length (Truelove et al 1994). A sink particle algorithm comprises two parts: (1) the computational condition to create such

a particle and (2) the accretion algorithm that the particle accretes surrounding gas. In AstroBEAR, the particle creation is based on the following conditions (Federrath et al 2010): (1) highest level of refinement: for if it is not on the highest level, the computation should try further refining such a region instead of “giving up” and declare a particle. (2) converging flow: this requires a check for $\nabla \cdot \mathbf{v} < 0$. (3) local density maximum. This check is tweaked from Federrath’s original criterion, which requires a gravitational potential minimum. (4) Jeans criterion. (5) energy bound check: requires total energy to be less than zero. (5) not in an accretion zone of an existing particle. The accretion zone is a fixed size cube surrounding a particle such that density in such a region is allowed to surpass the threshold density set by Jeans criterion. We implement several different particle accretion algorithm such as that described in Federrath et al 2010. For the simulations used in chapter 6, we employ the accretion algorithm in Krumholz et al 2006, which imposes Bondi accretion rate. The reasoning for such treatment is discussed in detail in chapter 6.

2.4 Multiphysics: Non-ideal MHD: Resistivity

In lab astrophysics, it is often the case that the Magnetic Reynolds number (defined by the ratio between magnetic diffusion time scale and the convective time scale of the field lines) cannot be approximated as infinity. It is therefore important to model the magnetic field diffusion when the simulation is used as a guidance to the lab astrophysics instrumentation design.

Under operator-splitting, we can treat the magnetic diffusion separately from the fluid equation. The resistive part can be written as:

$$\frac{\partial \mathbf{B}}{\partial t} = \nabla \times (\eta \nabla \times \mathbf{B}) \quad (2.14)$$

The magnetic diffusivity η is a function of temperature according to Spitzer 1961. When the field configuration in equilibrium is subject to strong diffusion, heating would occur and suppress the local resistivity and thus the diffusivity. By expanding equation 2.14, we have the following form:

$$\frac{\partial \mathbf{B}}{\partial t} = \eta \nabla^2 \mathbf{B} + \nabla \eta \times (\nabla \times \mathbf{B}) \quad (2.15)$$

The second term of the above expression on the right hand side depends on all of the three components of \mathbf{B} . So we end up with equations in which the time variance of B_x , B_y and B_z depending on each other. By fitting this equation into a linear solver, we get a coefficient matrix that is not a tri-diagonal matrix, and sometimes even ill-conditioned. However, To study the lab astrophysics simulations presented in chapter 7, the magnetic Reynolds number is much greater than 1. For such cases where resistive speed is slow, we can use explicit solver to treat the problem since implementing explicit stability condition will not result in significant slow down of the solver.

One may wonder if it is possible to throw away the second term on the right hand side of the diffusion equation to just let the diffusivity to vary with position but ignore its own spacial variation. This would give us a form of resistive MHD similar to that of the thermal diffusion case but with temperature dependence built in:

$$\frac{\partial \mathbf{B}}{\partial t} = \eta(T) \nabla^2 \mathbf{B} \quad (2.16)$$

Unfortunately, this does not work because the diffusion equation itself has to be divergence free. When treating constant resistivity, such approximation can satisfy this requirement as long as the divergence and the Laplacian are commutable. However, if resistivity has spatial distribution, we end up getting:

$$\frac{\partial \mathbf{B}}{\partial t} = \eta \nabla^2 (\nabla \cdot \mathbf{B}) + (\nabla \eta \cdot \nabla) \mathbf{B} \quad (2.17)$$

The first term on the right hand side is zero but the second term is not, especially at sharp temperature fronts where ∇T is large. Therefore the linear approximation only works under "slowly varying temperature" situation.

In AstoBEAR, we explicitly calculate the resistivity induced current on the cell edges, following equation:

$$\mathbf{J} = \eta \nabla \times \mathbf{B} \quad (2.18)$$

The stencil for this explicit solver is a 3×3 cube surrounding the cell we want to update. The magnetic field are vectors pointing to either x , y or z direction, centered on the cell faces. Its curl therefore reside on the cell edges. Figure 2.1 is an example on

calculating the diffusive current on the x direction, notice that the red arrow is where we are calculating the diffusive current, the green arrows are where the magnetic field originally resides.

Since the resistivity solver is explicit, its time step should base on stability requirement from equation 2.16. For fast magnetic diffusion cases, one may prefer implicit solver as such stability requirement can be a quadratic function of the resolution. However, we note that the diffusion equation 2.16 is not completely divergence free under finite differencing. After solving the linear system set by equation 2.16, we need to solve another linear system for the magnetic field so that any divergence caused by the error from solving equation 2.16 can be removed. Because its complicated nature, implicit resistivity is not included in AstroBEAR.

In the case of resistive MHD, energy can be dissipated in the form of Joule heat, comparing to the infinite conductivity case, where the voltage inside the fluid is everywhere zero, and no heat is generated by the current. If we dot the resistive induction equation with the magnetic field \mathbf{B} , we obtain the time evolution equation for magnetic energy:

$$\partial(B^2)/\partial t + \nabla \cdot \mathbf{S} = -\mathbf{J} \cdot \mathbf{E} = -j^2/\eta \quad (2.19)$$

where $\mathbf{S} = \mathbf{J} \times \mathbf{B}$ is the magnetic energy flux caused by resistive diffusion and $j = |\mathbf{J}|$ is the magnitude of the diffusive current. In this equation, the \mathbf{S} term accounts for the redistribution of magnetic energy (and thus the redistribution of total energy), and the last term accounts for the loss of magnetic energy due to reconnection. The total energy change for the resistive step is therefore:

$$\partial\epsilon/\partial t + \nabla \cdot \mathbf{S} = 0 \quad (2.20)$$

Here the j^2/η dissipation term is absent because the dissipation of magnetic energy does not change the total energy: the loss of magnetic energy is converted into thermal energy. In the algorithm, the energy flux as a result of magnetic diffusion needs to be calculated explicitly using:

$$\mathbf{S} = \mathbf{J} \times \mathbf{B} \quad (2.21)$$

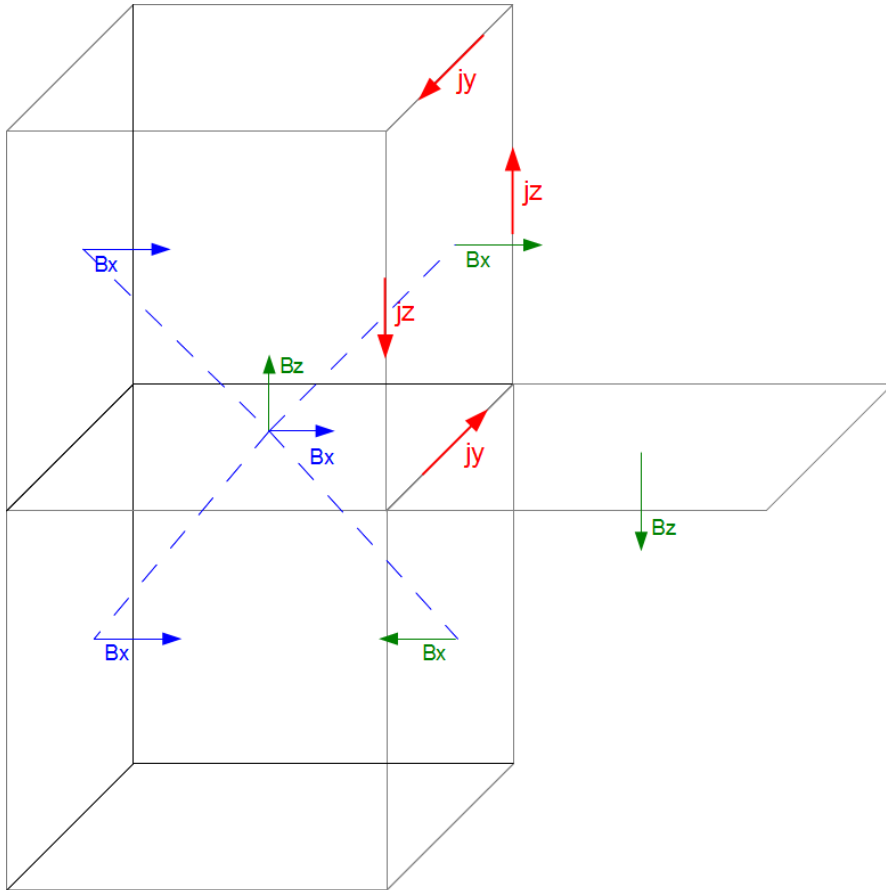


Figure 2.1 computation stencil for diffusive current and magnetic field calculation.

The energy fluxes reside on the cell faces while the diffusive currents reside on the cell edges. We therefore need to compute a face average of the diffusive current as well as the magnetic field components which are not normal to the face using the surrounding edges. In figure 2.1, the blue arrows connected by dashed lines are what are used to compute the energy flux. The magnetic field can be updated from the diffusive currents by:

$$\frac{\partial \mathbf{B}}{\partial t} = \nabla \times \mathbf{J} \quad (2.22)$$

Chapter 3

Multiphysics Tests

3.1 Test of MHD Heat Conduction

In this chapter, we introduce the numerical tests on the thermal conduction, self gravity and resistivity components of AstroBEAR.

The MHD solver and the linear thermal diffusion solver are verified by well-known tests such as the field loop convection problem and the Gaussian diffusion problem separately. As a comprehensive test that involves both MHD and thermal diffusion, we use the magneto-thermal instability (MTI) problem to test the accuracy of the ASTROBEAR code with anisotropic heat conduction (Parrish & Stone (2005), Cunningham et al (2009)). The problem involves setting up a 2-D temperature profile with uniform gravity pointing on the y direction. The domain is square with length of 0.1 in computational units. The temperature and density profiles are:

$$T = T_0 (1 - y/y_0) \tag{3.1}$$

$$\rho = \rho_0 (1 - y/y_0)^2 \tag{3.2}$$

with $y_0 = 3$. The pressure profile is set up so that a hydrostatic balance may be achieved with uniform gravity with gravitational acceleration $g = 1$ in computational units. We also set $T_0 = 1$ and $\rho_0 = 1$ in computational units. There is a uniform magnetic field on the x direction with field strength $B_0 = 1.0 \times 10^{-3}$ in computational

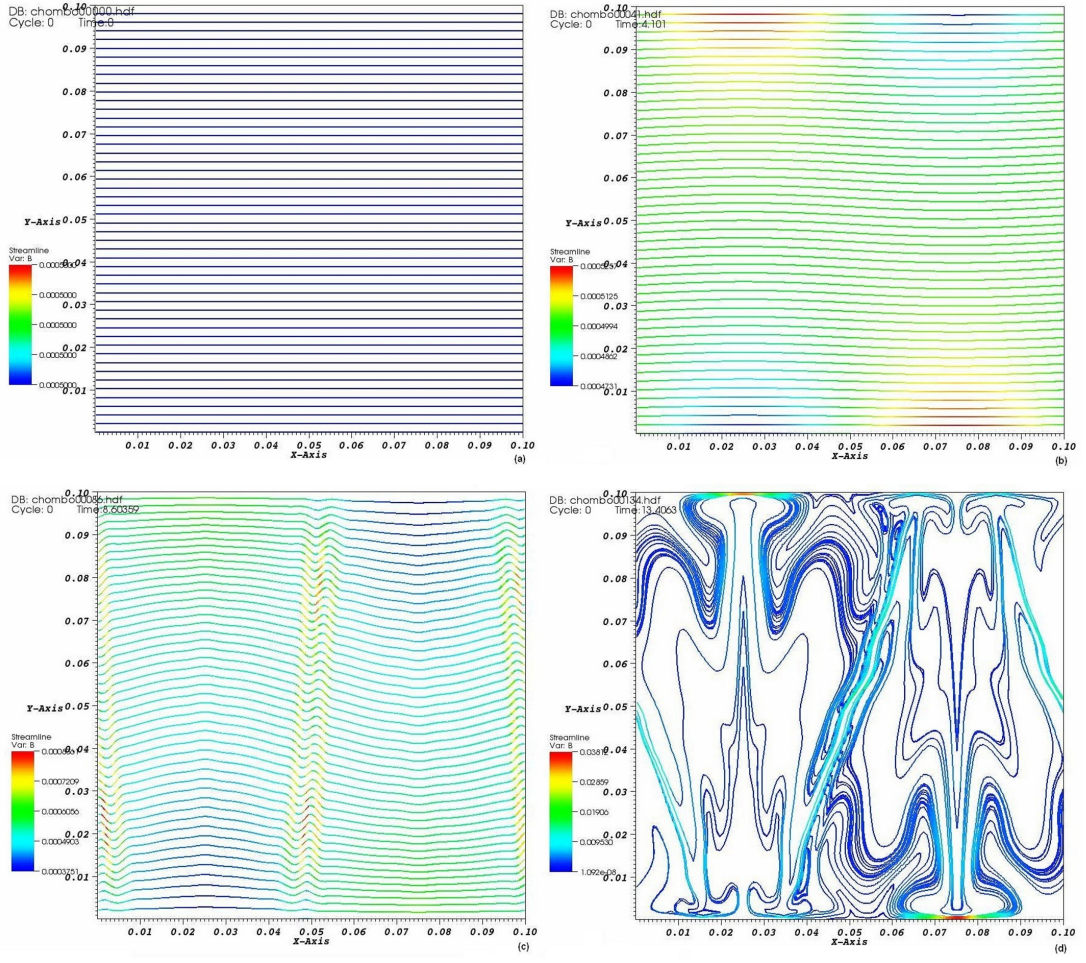


Figure 3.1 Field line evolution of magneto-thermal instability. (a): initial state. (b): $t = 75\tau_s$. (c): $t = 150\tau_s$. (d): $t = 250\tau_s$.

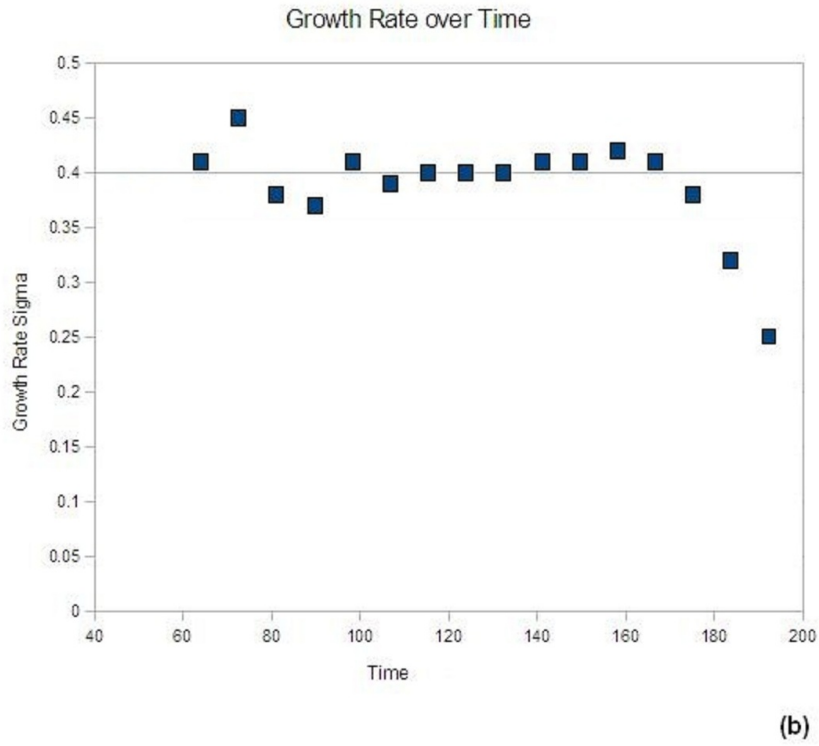
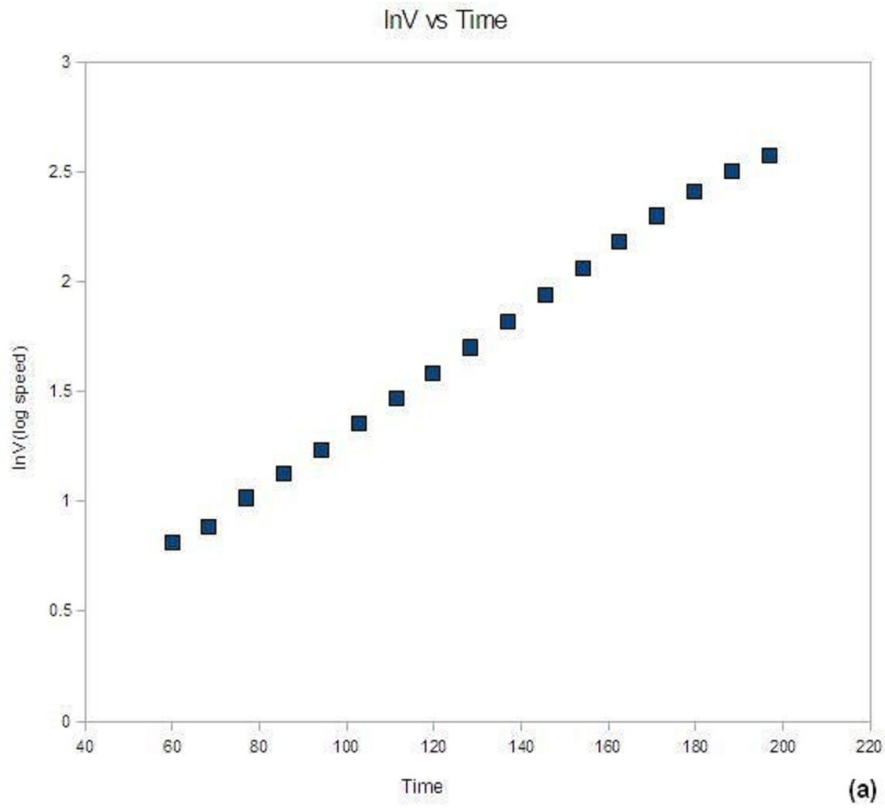


Figure 3.2 (a): $\ln v_y$ against evolution time in τ_s . (b): calculated growth rate against evolution time in computational units. Initially the growth rate is stable around the theoretical value 0.4 and then decreases sharply after $t = 200$, which indicates the evolution has entered the nonlinear regime.

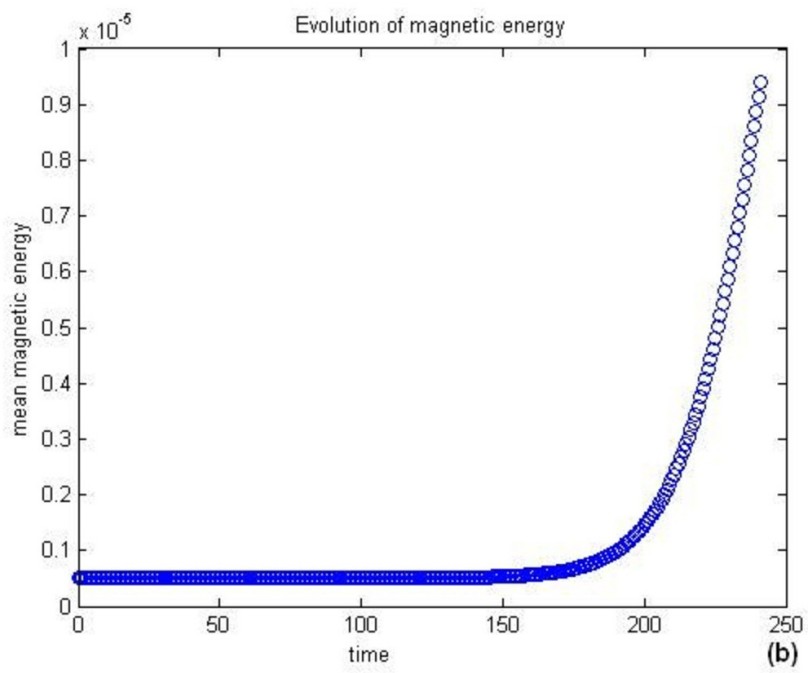
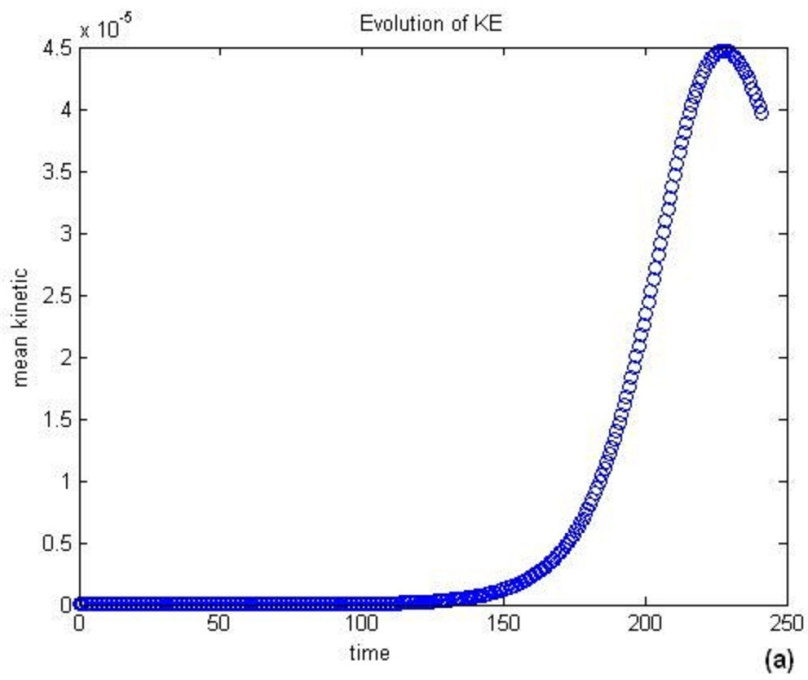


Figure 3.3 (a): evolution of mean kinetic energy. (b): evolution of mean magnetic energy.

units. The anisotropic heat conductivity is set to be $\kappa = 1 \times 10^{-4}$ in computational units. We use the pressure equilibrium condition for the top and bottom boundaries, that is, the pressure in the ghost cells are set so that its gradient balances the gravitational force. On the x direction, we use the periodic boundary condition.

Initially, the domain is in pressure equilibrium. We then seed a small velocity perturbation:

$$v_{per} = v_0 \sin(n \pi x / \lambda) \quad (3.3)$$

with $v_0 = 1 \times 10^{-6}$ and $\lambda = 0.5$. This perturbation will cause the fluid elements to have a tiny oscillation on y axis as well as the field lines. Once the field lines are slightly bent, they open up channels for heat to transfer on the y direction thus allowing the heat on the lower half of the domain to flow to the upper half. It can be shown that this process has a positive feedback so that once the heat exchange happens, more channels will be opened up for heat conduction. Therefore this process forms an instability whose growth rate can be verified according to the linear instability growth theory. We use τ_s to denote the sound crossing time for the initial state. Figure 3.1 shows the time evolution of the field lines at various stages in our MTI simulation.

We study the MTI growth rate by considering the acceleration of the fluid elements. The mean speed on the y direction for the fluid should follow the exponential growth:

$$v_y = v_{per} e^{\gamma t} \quad (3.4)$$

where v_{per} is the strength of the initial velocity perturbation applied, γ denotes the growth rate in the linear regime. We obtain the growth rate γ by plotting $\ln v_y$ against the evolution time and then measuring the local slope through a certain time span. The $\ln v_y$ vs t curve is plotted in figure 3.2(a), which shows a nice linear relation. We plot the growth rate against evolution time. It should be stable around the theoretical value 0.4 initially and then decrease sharply due to the nonlinear effect. Figure 3.2(b) shows that the simulation meets our expectation well.

We also look at the energy evolution in the linear regime. The mean kinetic energy should first stay stable and then enter into an exponential growing phase until it hits

a cap at around $t = 200$ which denotes the starting of the nonlinear phase. The evolution of magnetic energy should follow similar pattern as to the kinetic energy evolution, but lagged behind. In figure 3.3, we plot the time evolution of the mean kinetic and magnetic energy evolutions. The results confirms the physical intuition quite well.

3.2 Test of Self Gravity with Sink Particle

3.3 Test of Resistive MHD

One famous problem to test the non-ideal MHD is the Sweet-Parker problem. In such problem, the initial fluid is held at sheer pinch quasi-equilibrium. The fluid is then perturbed by either adding a vertical velocity distribution or by increasing the resistivity at the center of the pinch. The initial magnetic field distribution is given by:

$$B_y(x) = b_0 \tanh(x/a) \quad (3.5)$$

where in computational units we choose field amplitude $b_0 = 1$ and length scale $a = 0.5$. The density profile is chosen so that the pressure equilibrium can be maintained with constant temperature:

$$\rho(x) = \rho_0 / \cosh^2(x/a) + \rho_c \quad (3.6)$$

where $\rho_0 = 1$ is the density contrast, $\rho_c = 1$ is the background density. The temperature is set to be constant at 0.5 in computational unit.

The test domain is set to be $-6.4 < x < 6.4$ and $-12.8 < y < 12.8$, with resolution of 480×960 and two levels of AMR. The boundaries are all transparent. The initial profile is plotted in figure 3.4..

The initial state is in pressure equilibrium though unstable. As stated before, there are two ways to generate instabilities. The first way is to artificially increase the resistivity at the center of the domain. This increase will result in a higher reconnection, which will eventually bend magnetic field. This creates an X point at

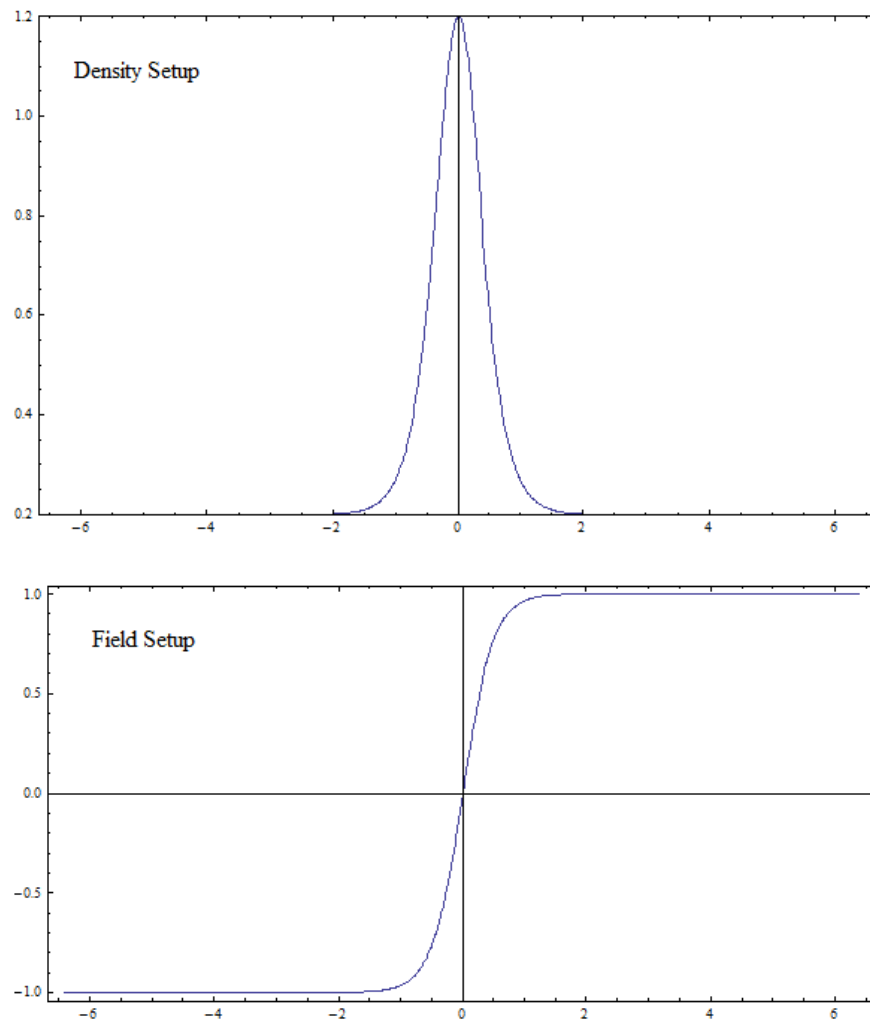


Figure 3.4 Density and magnetic field distribution for Swee-Parker test.

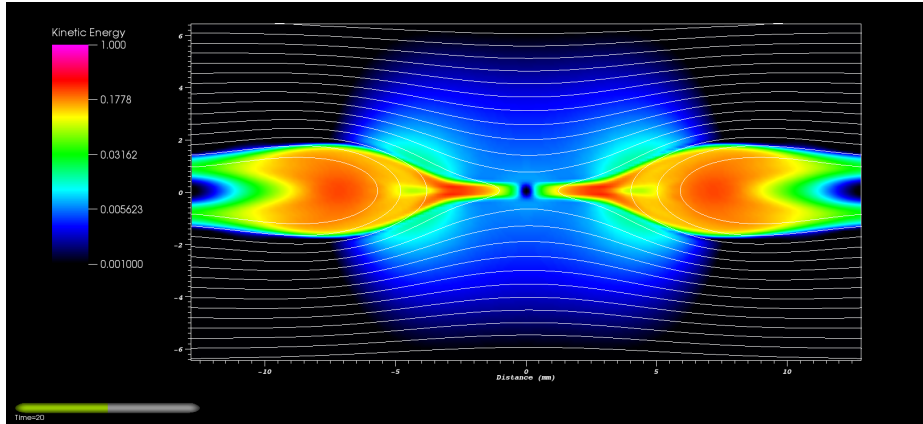


Figure 3.5 Normalized kinetic energy and magnetic field distribution for Sweet-Parker outflow.

the center where field lines continue to come in and reconnect because of the lower field pressure at the center. The reconnection heat will drive outflows out of the X point, parallel to the direction of the sheer pinch. The box surrounding the X point where the outflows (Petschek shock) come out of is called the "Sweet-Parker Box". Figure 3.5 shows the Sweet-Parker flow from a reconnection spot at the center. Colored variable is the kinetic energy in log scale, magnetic field is illustrated by white streamlines.

The measured outflow has Alfvenic Mach 1, which is consistent with theoretical value.

Chapter 4

Magnetized Thermal Conduction in Wind Blown Bubbles

4.1 Introduction

Interfaces between hot and cold plasmas can occur in astrophysics where understanding the rate of thermal conduction may be an important part of the astrophysical phenomenology. One example occurs in wind blown bubbles (WBB) of evolved stars where magnetized hot supersonic outflow shock heats the cooler ambient magnetized interstellar medium. For such WBB, there are examples where the presumed shock heated bubble is cooler than expected if only radiative cooling is considered (Zhekov et al. (2011)). A possible explanation is that heat loss through the interface of hot bubble into the cold shell via thermal conduction reduces the temperature of the hot bubble (Zhekov & Park (1998), Zhekov & Myasnikov (2000)). However the source of heat into the cold side of the interface will continuously evaporate material there and potentially induce interface instabilities and mass mixing (Stone & Zweibel (2009)) that could tangle the magnetic field. Understanding the thermal conduction and its dependence on magnetic structure is important for determining the thermal properties of the plasma on either side of the interface.

For the ISM and ICM, it is usually valid to assume that the electrons are totally inhibited from moving across field lines (McCourt et al (2011)), as the electron mean

free path is much greater than the electron gyroradius. The underlying assumption is that the field configuration is ideal and there is no stochastic fluctuations existing. The magnetic field structure then plays a key role in controlling the rate of thermal conduction since electrons can move freely only along the field lines. It is worth pointing out that in reality, however, the stochastic field can change the cross field diffusion even if its amplitude is small. Using the conditions given by Rechester & Rosenbluth (1978), it can be shown that the ratio of ion gyroradius and the field length scale presented in our simulation is small. This means even a small added stochastic field is likely to make a difference in the anisotropy of the thermal diffusion. The result is a strong thermal conductivity parallel to the field lines and a weak conductivity across the field lines.

The quantitative subtleties of how a complicated magnetic field structure affects thermal conduction for raises the open question of whether there is a simple measure of field tangling that allows a practical but reasonably accurate correction to the isotropic conduction coefficient for arbitrarily tangled fields. In this context, two classes of problems can be distinguished. The first is the conduction in a medium for which forced velocity flows drive turbulence, which in turn tangles the field into a statistically steady state turbulent spectrum (Tribble (1989), Tao (1995); Maron et al. (2004)). The second is the case in which the flow is laminar and the level of conduction inhibition is compared when the field starts from initial states of different levels of tangling subject to an imposed temperature difference across an interface. This second problem is the focus of our preset paper. It should be stated that the conductivity in our simulations remains that associated with the micro-physical scale throughout the evolution of our simulation. That is, our flow remains laminar so we do not have a broad turbulent spectrum of magnetic fluctuations or a corresponding increase in the effective conductivity as in Narayan & Medvedev (2001).

Using the ASTROBEAR magnetohydrodynamics code with anisotropic thermal conduction, we investigate the influence of initial magnetic structure on thermal conduction in an otherwise laminar flow. The key questions we address are: (1) does the interface become unstable? (2) how fast is the thermal conduction across the interface compared to the unmagnetized case?

We study these questions using different initial magnetic configurations imposed on a planar thermal interface to determine how the conduction depends on the amount of field tangling across the interface. In section 2, we review the basic equations of MHD with anisotropic thermal conduction. In sections 3 and 4 we provide detailed description of the simulation setup. In section 5 and 6 we present the simulation results and analyses. In section 7, we discuss the simulation results in the context of the WBB cooling problem and the cooling flow problem in cores of galaxy clusters. The appendix provides more detailed information on the testing of the ASTROBEAR code.

4.2 Problem Description and Analytical Model

Our initial set up involves hot and cold regions separated by a thin planar interface. We study how the magnetic field configuration alters the heat transfer rate between the hot and cold regions in presence of anisotropic heat conduction. We study the problem in 2-D.

To guide subsequent interpretation of the results, we first compare two simple but illustrative limits of magnetic field orientation: (1) a uniform magnetic field aligned with the direction normal to the interface; (2) a uniform magnetic field perpendicular to the normal direction of the interface. In case (1), because the angle between the magnetic field and temperature gradient is everywhere zero, heat conduction across the interface is expected to take on the Spitzer value associated with isotropic heat conduction. In case (2) however, the angle between the magnetic field and the temperature gradient is always 90° , so with our approximations, heat cannot flow across the interface.

We define a heat transfer efficiency ζ equal to the magnetic field-regulated heat transfer rate divided by the isotropic Spitzer rate, namely,

$$\zeta = \frac{q}{q_i} \quad (4.1)$$

where q is defined as the amount of thermal energy transported through the interface per unit time. The average angle θ between the temperature gradient and the uniform

magnetic field then plays an important role in determining ζ . At $\theta = 0$, $\zeta = 1$. At $\theta = \pi/2$, $\zeta = 0$.

We now address the influence of both a mean field and a tangled field on ζ . Consider there to be a strongly tangled local field that has no mean value in the direction normal to the interface, i.e. $\mathbf{B}_{0,x}$ whose total magnitude is B_0 , and a global magnetic field \mathbf{B}_d aligned with the normal of the interface of magnitude B_d . If $B_d \gg B_0$, the magnetic field around the interface only slightly deviates from the normal direction and ζ should be close to 1. If $B_d \ll B_0$, ζ should be close to zero. The asymptotic limit of the heat transfer efficiency is given by Chandran & Cowley (1998) that $\zeta \simeq 1/(\ln(d/\rho_e))$, where d is the scale length of the magnetic field fluctuation, ρ_e is the electron gyroradius. In our problem, we estimate this limit at about 4.7%. In the subsequent context, we will use ζ_0 to denote this asymptotic limit.

If B_d and B_0 are comparable, we expect $\zeta_0 < \zeta < 1$. We also expect ζ can change throughout the evolution if the structure of the magnetic field is modified by the dynamics of heat transfer. It is instructive to ask whether the feedback from the magnetic field structure evolution will amplify the heat transfer by creating more channels, or shut it down. The answer depends on the influence of magnetic reconnection, as we will see from the simulations. Only if magnetic reconnection acts to smooth out local small scale structures and link the initially isolated structures to the global mean field across the interface then we would expect the heat conductivity to increase.

In what follows, we refer to the initial tangled field region as "the interaction region". Figure 4.1(a) shows a schematic of initial and hypothetical evolved steady state field configurations for such a tangled field set up. From the figure we can see that the initial field configuration forms a "wall" which restricts energy transfer across the two interaction region. However, if the subsequent evolution evolves to the steady state shown in (b), then expansion of the interaction region and magnetic reconnection has allowed the field to penetrate through the entire region. Thus the initial "wall" of tangled field is destroyed and thermal conduction will be less inhibited than initially. We will check how accurately this proposed picture of destruction of

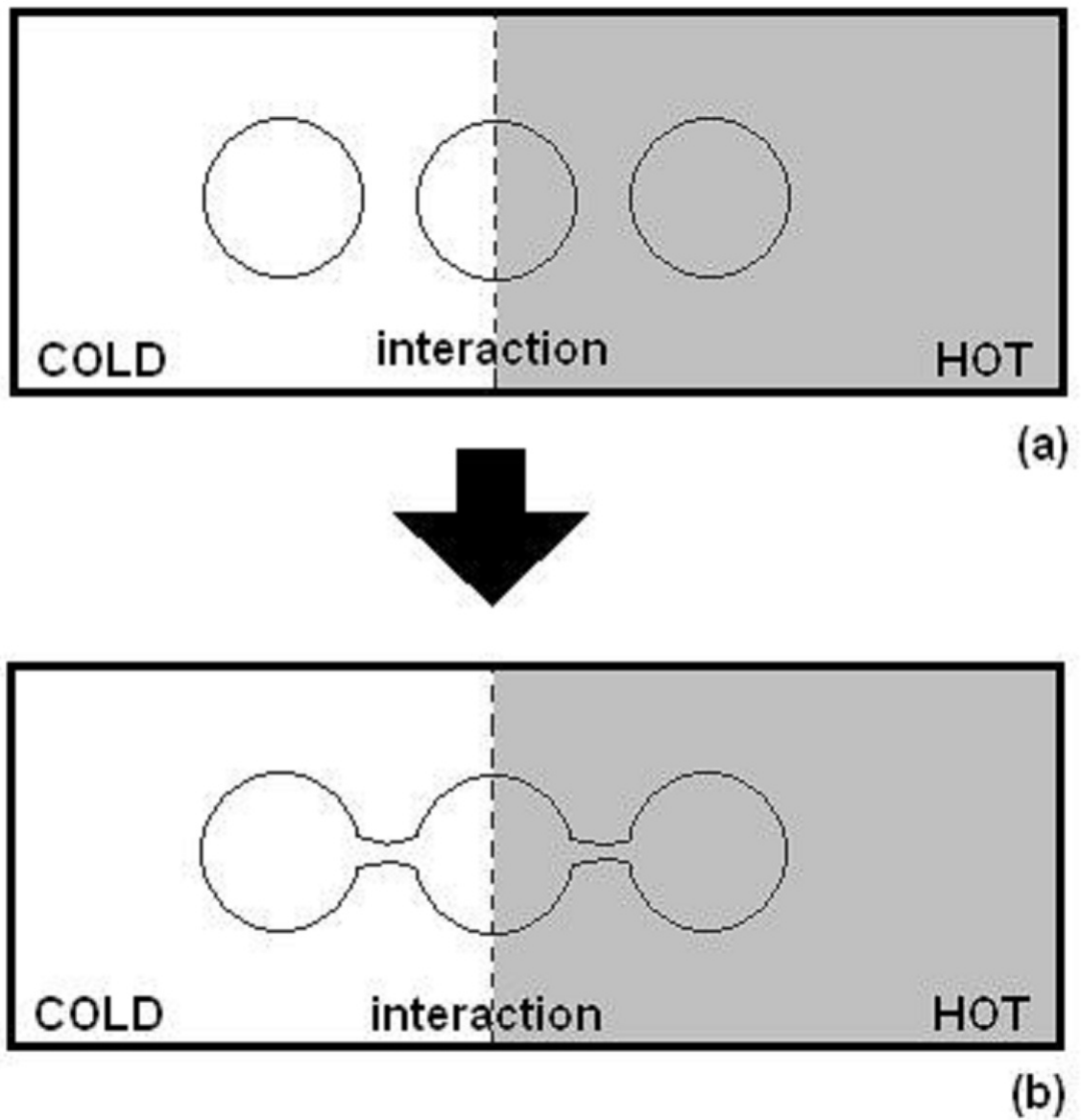


Figure 4.1 The initial and steady state field configuration. (a): the initial field forms complete loops that only allows heat transfer within the interaction region. (b): the steady state field reconnects itself so that it allows heat transfer between regions deeply into the hot and cold areas.

field wall is valid from analyzing our numerical simulations, and quantitatively discuss the effects on the energy transfer.

4.3 Simulation Setup

For our initial conditions, we set up an interface between hot and cold regions in mutual pressure equilibrium. The temperature distribution on the horizontal x axis is given by $T(x) = T_0[1 - 4(x - x_0)^2/w^2]^{0.4}$ in the region $[x_0, x_0 + w]$ with $T_0 = 100$ in computational units. This region is the interaction region as described in the previous section, with x_0 as the left end, w as the width. In the regions $(0, x_0)$ and $(x_0 + w, L_x)$ where L_x is the domain length, we simply assume $T(0 < x < x_0) = T(x = x_0)$ and $T(x_0 + w < x < L_x) = T(x = x_0 + w)$: in other words, the temperature profile has a sharp gradient inside $[x_0, x_0 + w]$. while outside this region, it remains flat. The obtained temperature distribution is plotted in Figure 4.2(a). We set $x_0 = 0.4$ and $w = 0.1$. The region $0.4 < x < 0.5$ is therefore the interaction region. The temperature is constant and uniform across the regions of each respective side of the box connecting to that side of the interaction region. We are primarily interested in the region of the box where the heat transfer occurs and noticeably evolves during the simulation run time. This means we will mainly focus on the interaction region. The horizontal length of the interaction region in the simulation domain is $L_x = 0.8$ in computational units.

The thermal pressure is set to be in equilibrium over the entire box, that is $P(x) = P_0$ with $P_0 = 100$. The density distribution is set up by the ideal gas law, namely $\rho(x) = P(x)/T(x)$ in computational units.

For the Spitzer diffusion coefficient, we assume the diffusion is linear, and use the approximation $\kappa_{\parallel} = \kappa_c T_{mid}^{2.5}$, where κ_c is the classical conductivity, and T_{mid} is taken to be the middle value of temperature across the interface, about $0.5 T_0$.

We choose the initial field configuration:

$$B_x = B_d + B_0 \sin(n \pi y / \lambda), \quad (4.2)$$

$$B_y = B_0 \sin(n \pi x / \lambda) \quad (4.3)$$

where n and λ are the mode number and wavelength of the tangled field respectively, $B_0 = 10^{-3}$ in computational units, and B_d can assume various initial values that reflect the evolving global field as the result of reconnection. The magnetic field configuration is laminar, and there is no broad spectrum of magnetic fluctuations. The magnetic spectrum is concentrated at length scale λ . This initial field configuration is therefore one of a locally tangled field surrounding the interface with one measure of the tangle given by:

$$R = B_d/B_0 \quad (4.4)$$

When $R = 0$, there are only locally confined field lines, whereas $R = \infty$ indicates a straight horizontal field without any "tangling". As R increases, the relative fraction of field energy corresponding to lines which penetrate through the interaction region increases. In our simulations, we consider cases with $R = 0.0, 0.2, 0.4, 0.6, 1, 2, 4, \infty$. Figure 4.2(a), Figure 4.4(a) and Figure 4.5(a) show the magnetic field configuration for initial R values of 0.0, 0.4, 1.0.

We note that our MHD approximation a priori implies that the electron gyroradius is much smaller than the length scale of one grid cell. Thus the dissipation scale and all field gradient scales are larger than the electron gyro-radius by construction in our simulations.

We run simulations with typical resolution of 2048 cells on the horizontal axis in fixed grid mode. Runs with doubled resolution showed no significant differences compared to the standard resolution runs. We use fixed boundary conditions at the x boundaries: the pressure, density and temperature at the two ends are fixed to their initial values, as is the magnetic field. We use periodic boundary conditions for the y axis boundaries.

There are five parameters whose influence determine the simulation behavior and guide interpretation of results:

1. **Plasma β .** $\beta \equiv \frac{8\pi P}{B^2}$ has little effect on diffusion because even with very high values of the plasma β used in the simulation, we are still in the MHD regime and the gyro-radii of electrons are assumed small. Thus the direction of thermal conduction is not locally affected by β . It is possible that instabilities could arise in the low β

limit that affect pressure balance during the evolution of the simulations but that turns out not to be the case for the β range of $10^5 \sim 10^8$ that we use. The value of β in this range does not exhibit any influence on the simulation result as indicated by our numerical experiment.

2. Initial Tangle measure $R = B_d/B_0$. If $R \gg 1$, the local small scale field can mostly be ignored and Spitzer thermal conductivity is expected, whereas if $R \ll 1$ a value much less than Spitzer is expected.

3. Ratio of the diffusion time scale to the sound crossing time scale for one grid cell:

$$r = t_{diff}/t_{hy} = \frac{\rho C_s l}{\kappa_{\parallel}} \quad (4.5)$$

where ρ is the density, l is the characteristic gradient length scale of temperature: $l = \min(\frac{T}{|\nabla T|})$ and C_s is the sound speed. If $r \ll 1$, thermal diffusion would initially dominate and the pressure equilibrium would be broken by this fast energy transfer. If $r \gg 1$, then the pressure equilibrium would be well maintained throughout the entire evolution and the energy transfer may be viewed as a slow relaxation process. In our simulation, $r \approx 0.3$ initially, so that diffusion induces a pressure imbalance. Eventually, as the heat transport slows, the pressure equilibrium catches up and is maintained.

4. Ratio between the temperature gradient scale length and the wavelength of the tangled field: $h = 2\pi l/\lambda = kl$. If $h = 0$ there is no tangled field, and no inhibition to heat transfer. As h increases, the field becomes more tangled, and the energy is harder to transfer. However, a large h value may also result in increased magnetic reconnection, because the Lundquist number of field confined in a smaller region is larger, for the same field strength. Thus would then lower h .

5. Mean global energy transfer rate: $q = \delta E/t_{bal}$, where t_{bal} is defined as the time needed for the hot region and cold region to reach a certain degree of temperature equilibrium by a transfer of heat energy δE across the interface.

A mathematical expression for the heat transfer rate can be derived by considering a slab with a planar interface aligned with the y direction at the middle of the

interaction region with a tangled magnetic field, and an average temperature gradient aligned in the x direction. As in Section 4, we denote the region $[x_0, x_0 + w]$ as the interaction region which contains the interface and the tangled field. Define the average temperature gradient inside the interaction region as $|\nabla T|_g = (T_{hot} - T_{cold})/w$, where the subscripts “hot” and “cold” denote the characteristic temperatures of the hot and cold sides at the two ends of the interaction region. We assume that the resulted effective heat flux depends on how much straight mean field can penetrate through the interaction region. We also assume the heat flux depends on the average temperature gradient of the interaction region in the form: $q \propto |\nabla T|_g$. By integrating the proportion of the amount of straight mean field over the volume of the interaction region (and since there is no z -dependence, the essential content is an area integral) to obtain the effective heat flux through this region:

$$\bar{q} = D |\nabla T|_g \int \frac{B_d}{|B|} dx dy, \quad (4.6)$$

where D is a constant that depends on neither the magnetic field nor the average temperature gradient, $|B|$ is the local field strength. The 2-D integration is carried out over the interaction region: with $x_0 < x < x_0 + w$, $0 < y < L_y$. Notice that this expression is valid only when the magnetic field is varying at a length scale smaller than the interaction region length.

Using equations 4.2, 4.3, 4.4 in 4.6 and the approximation that the areal average in the interaction region $\langle \mathbf{B}_0 \cdot \mathbf{B}_d \rangle \sim 0$ so that $\langle (\mathbf{B}_0 + \mathbf{B}_d)^2 \rangle \sim \langle B_0^2 + B_d^2 \rangle$, we obtain

$$\bar{q} \approx D \frac{|\nabla T|_g R}{\sqrt{1 + R^2}}. \quad (4.7)$$

For the unmagnetized isotropic case, or for transfer with a field entirely aligned with the temperature gradient, we have instead

$$\bar{q}_i = D |\nabla T|_g. \quad (4.8)$$

Dividing equation 4.7 by 4.8, we obtain an approximation for the heat transfer efficiency over the interaction region:

$$\zeta = \frac{R}{\sqrt{1 + R^2}}. \quad (4.9)$$

It should be pointed out that our approximation does not take into account the ζ_0 "leakage" from the magnetic field fluctuation as stated in Section 3 and Chandran & Cowley (1998). If the initial temperature profiles are identical for different field configurations, this formula can then be used to estimate the expected energy transfer rate from situations with various field configuration. By normalizing the heat transfer rate to that of the isotropic heat conduction case, we obtain the heat transfer efficiency ζ . The accuracy of equation 4.9 can be tested by plotting the heat transfer efficiency obtained from the simulations against measured values of R .

If magnetic reconnection occurs during the time evolution of the heat transfer process, then conduction channels can open up and the energy exchange can be accelerated. We would then expect the actual curve of ζ vs R to evolve to be higher than the value equation 4.9 predicts in situations with low R values. Meanwhile, for high R , the analytical prediction and the real physical outcome should both approach the horizontal line $\zeta = 1$, which denotes conductive efficiency consistent with the unmagnetized case. We emphasize that R as used in this paper is always calculated with the the initial values of the magnetic field, not time evolved values, and that equation 4.9 is valid when estimating a cold to hot interface with initial tangle measure as the ratio of initial global straight field to initially local tangled field. To follow a measure of the tangle that evolves with time, a generalized tangle measure should be calculated in a more sophisticated manner and the integral form equation 4.8 should be applied.

4.4 Simulation Results

We choose initial conditions with values $R = 0.0, 0.2, 0.4, 0.6, 1.0, 2.0, 4.0$ to run the simulations. The simulation run time is taken to be 1.2 (which corresponds to 12,000 years in real units for WBB). The initial cuts of temperature and magnetic field lines for $R = 0.0, 0.4, 1.0$ are shown in Figure 4.2(a), Figure 4.4(a) and Figure 4.5(a) respectively. Figure 4.3(a) shows the initial cut of the density distribution in the $R = 0.0$ run. We also run simulations with purely horizontal magnetic field lines, equivalent to the $R = \infty$ case, and runs with purely vertical field lines. Frames (b) to

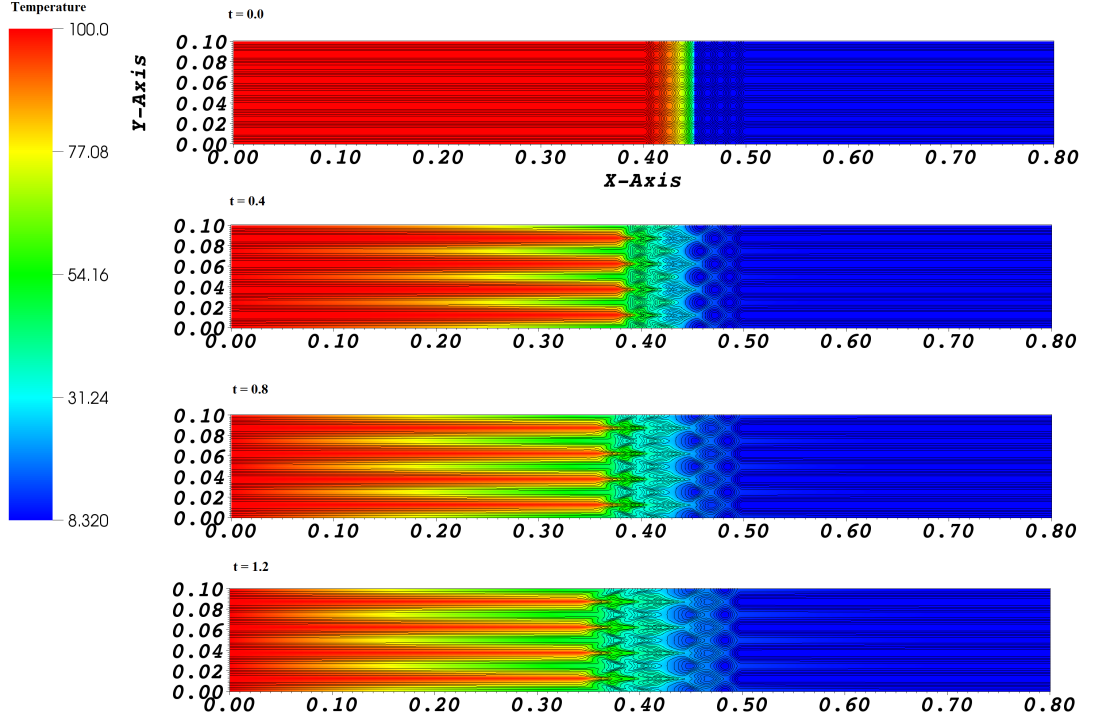


Figure 4.2 Evolution of temperature distribution with $R = 0.0$. The cuts are at (a): $t = 0.0$, the initial state, (b): $t = 0.4$, (c): $t = 0.8$, (d): $t = 1.2$, the steady state.

(d) in Figure 4.2 to Figure 4.5 are from the late stages of the evolution, and the final frames always display the steady state of the runs. A steady state is facilitated by the fact that the boundaries are kept at a fixed temperature throughout the simulations.

In Figure 4.6, we plot the mean cuts of the temperature T_c , obtained by averaging the temperature along y axis, against the x position for selected evolution times. Since the anisotropic heat conduction is initially faster than the pressure equilibration rate, the energy distribution around the temperature interface change rapidly until about $t = 0.4$. This energy transfer is mostly confined to the interaction region for the low R_0 runs, since in these cases only a few field lines can penetrate into the entire interaction region.

During the initial heat exchange phase, the thermal energy and density quickly redistribute in the interaction region. As seen in Figure 4.2(b), islands at $x = 0.48$ are formed by material bounded by the magnetic field lines, since the field orientation

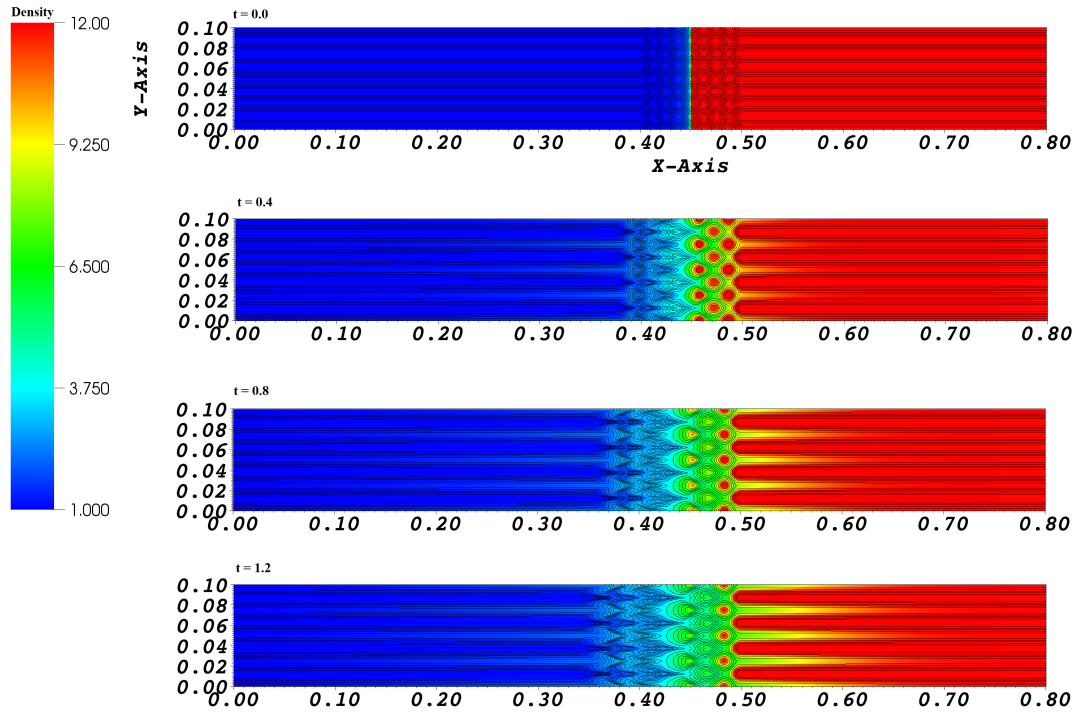


Figure 4.3 Evolution of density distribution with $R = 0.0$. The cuts are at (a): $t = 0.0$, the initial state, (b): $t = 0.4$, (c): $t = 0.8$, (d): $t = 1.2$, the steady state.

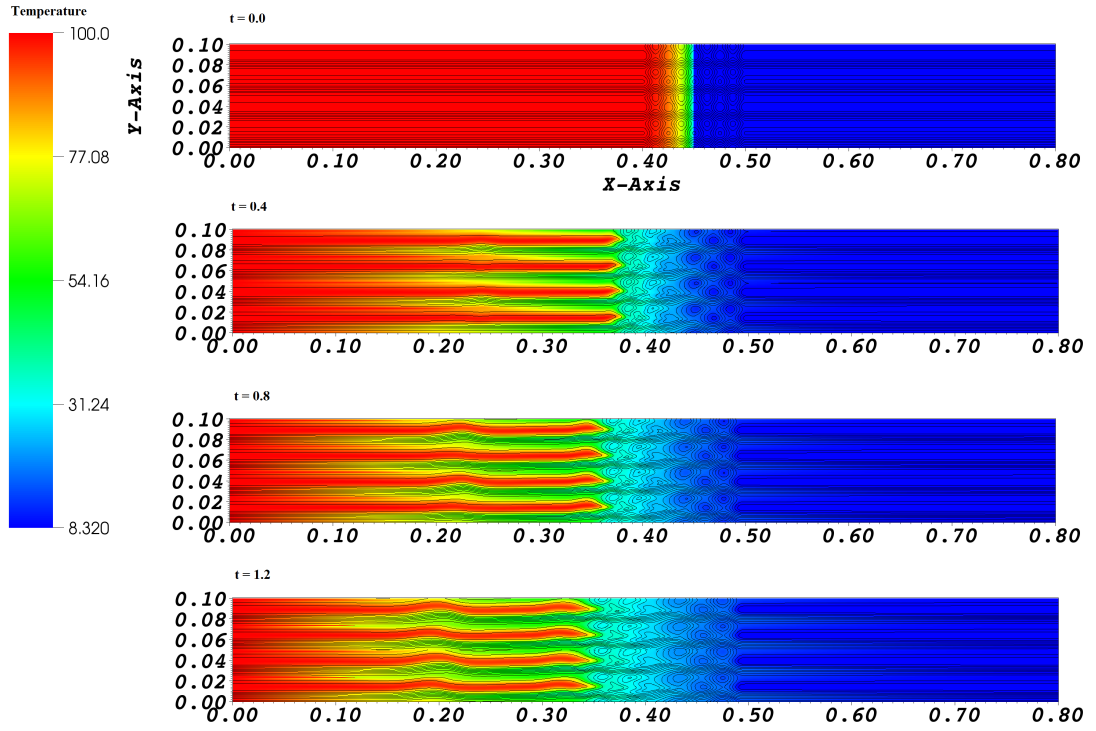


Figure 4.4 Evolution of temperature distribution with $R = 0.4$. The cuts are at (a): $t = 0.0$, the initial state, (b): $t = 0.4$, (c): $t = 0.8$, (d): $t = 1.2$, the steady state.

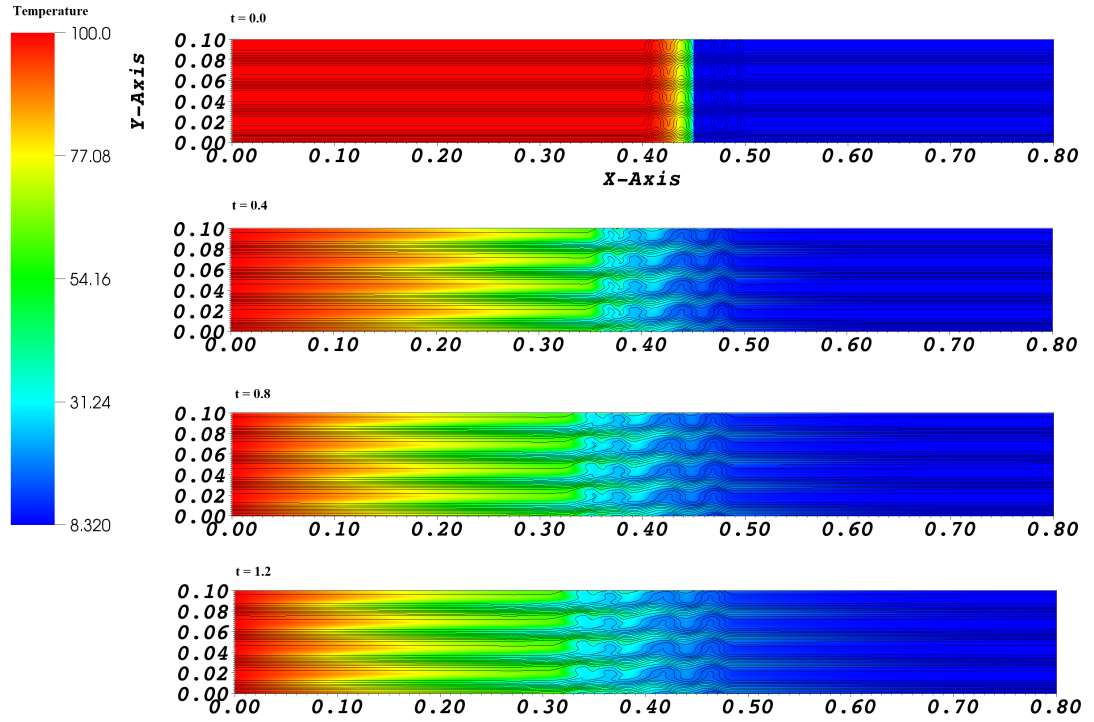


Figure 4.5 Evolution of temperature distribution with $R = 1.0$. The cuts are at (a): $t = 0.0$, the initial state, (b): $t = 0.4$, (c): $t = 0.8$, (d): $t = 1.2$, the steady state.

blocks heat exchange with the surroundings. Around $x = 0.4$, there are also cavities formed where the thermal energy is inhibited from flowing. The magnetic field lines, which form complete sets of loops in the $R = 0.0$ case, begin to distort. It can be observed that the field lines are more strongly distorted in the low density part of the interaction region than in the high density part. This occurs because velocity gradients are driven by the early rapid redistribution of heat (pressure) by conduction.

At time $t = 0.4$ (see Figure 4.2(b)), the field lines surrounding the cavities at $x = 0.4$ reconnect, making thermal exchange possible. During the evolution, field lines begin to link the interaction region to the hot material on the left. This phenomenon is most apparent in Figure 4.2(d), which marks the final state of the thermal energy exchange. We also see that there is little difference between Figure 4.2(c) and Figure 4.2(d), because at late stage of the process, the thermal diffusion gradually slows so that the magnetic field configuration approaches a steady state.

By comparing Figure 4.6(c) with Figure 4.6(d), we see that the mean cuts of temperature show little difference for all values of R . The mean cuts of temperature T_c exhibit a jump in the region of $x = 0.35 \sim 0.5$, but are relatively smooth on either side of this region. This shows that even though the tangled field "wall" has been broken and allows channels of thermal conduction through it, the temperature profiles is not as smooth as in the purely straight field case.

For the cases of $R = 0.4$, there are field lines which penetrate the entire interaction region from the start. By observing the evolution of the magnetic field lines at about $x = 0.38$, we see that magnetic reconnection is still happening, and causes the field loops to merge. The observed behavior resembles the process displayed by Figure 4.1. When $R = 1$, there are hardly any temperature islands that bounded by magnetic field loops. The evolution of the field lines shows less dramatic reconnection and evolve in what appears as more gentle straightening.

4.5 Discussion

We begin our analysis with the evolution of the heat flux. The average heat flux per computation cell for different values of R is plotted as a function of time in

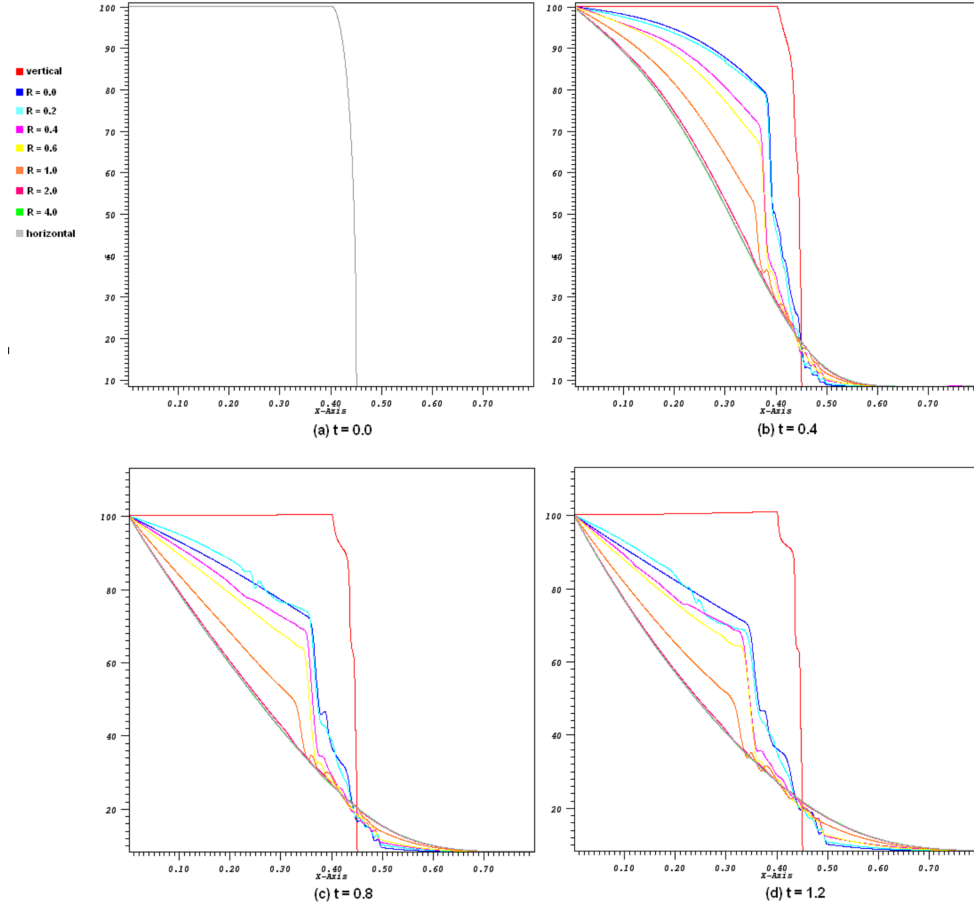


Figure 4.6 Evolution of mean cut temperature averaged on y direction with different R values labeled by different colors. The cuts are at (a): $t = 0.0$, the initial state, (b): $t = 0.4$, (c): $t = 0.8$, (d): $t = 1.2$, the steady state.

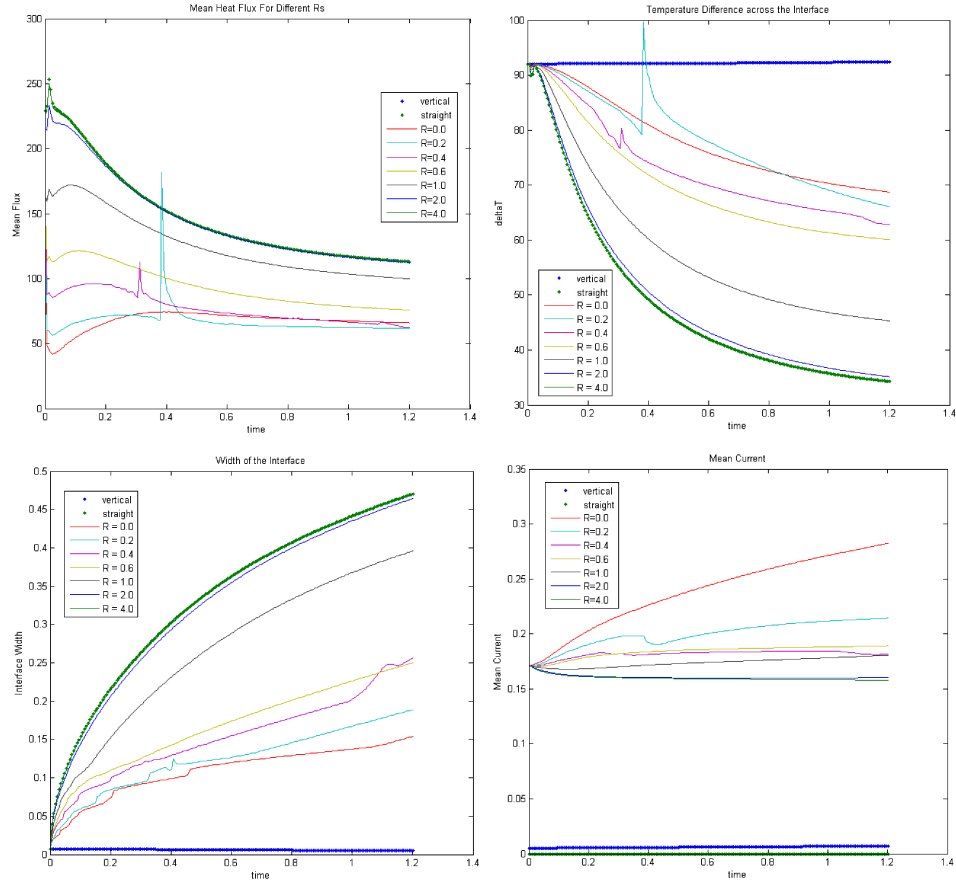


Figure 4.7 (a) top left: time evolution of mean heat flux at the interface, (b) top right: time evolution of average temperature difference between the hot and cold regions, (c) bottom left: time evolution of interface width, (d) bottom right: time evolution of the mean value of $|\nabla \times \mathbf{B}|$.

Figure 4.7(a). Note that in the vertical field case ($\mathbf{B} = B_y \hat{y}$) the heat flux remains zero as field entirely inhibits electron motion across the interface. For cases with $R > 1$, the heat flux decreases throughout the evolution. Recall that $R > 1$ implies cases where the "tangled" portion of the field is relatively weak and heat is quickly transported from one side of the interface to the other. Thus the trend we see for $R > 1$ occurs as the temperature distribution approaches its equilibrium value. For lower R values, especially those of $R < 0.5$, an initial phase of heat flux amplification is observed as magnetic reconnection in the early evolution opens up channels for heat to transfer from hot to cold regions. At the late stage of the evolution when reconnection has established pathways from deeper within the hot region to deeper within the cold region temperature equilibration dominates leading to a decreasing heat flux phase as observed in the $R > 1$ cases. Note that the similarity between the $R > 2$ cases and the $R = \infty$ case is predicted by equation 4.9: as the global field comes to dominate, the heat flux inhibition imposed by anisotropic heat conduction in the local tangled field can be ignored.

In order to understand the influence of magnetic reconnection on heat transfer rates we compare simulations with different filling fractions of the tangled field. Two cases are shown in Figure 4.8(a): (1) a temperature interface with a "volume filling" tangled field and (2) temperature interface with the tangled field filling only the region surrounding the interface. In case (2) the rest of the domain is filled with straight field lines connecting the hot and cold regions. From Figure 4.8(a) we see that case (1) shows much slower heat transfer rates compared to what is seen in case (2). This results because reconnected field lines in case (2) are linked to the globally imposed background field that in turn linking the hot and cold reservoirs. In case (1) reconnection only leads to larger field loops but cannot provide pathways between the reservoirs. The effect of different scale lengths on the evolving field loops is shown in Figure 4.8(b) in which we plot the result from three simulations wavelengths for the tangled field component (tangled field "loops"). Note that λ is defined in equations 4.2 and 4.3. We use a sequence of values for wavelength: 2λ , λ and $\lambda/2$. Figure 4.8(b) clearly shows that smaller field loop λ leads to the largest average heat flux, since smaller scale loops will reconnect before large loops for a given magnetic resistivity.

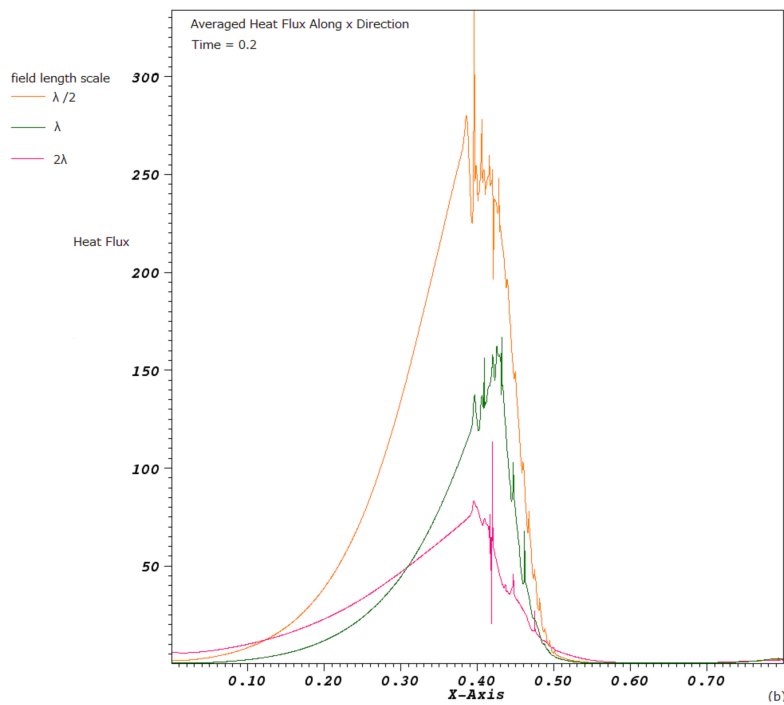
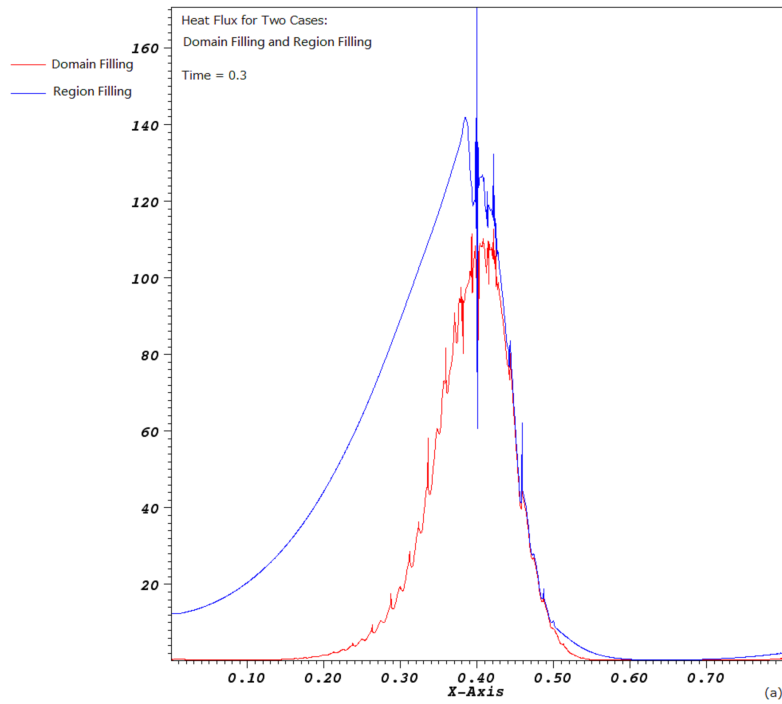


Figure 4.8 (a) Comparison of averaged heat flux for situation with field loops filling up the entire domain and situation with field loops only fill the interaction region. (b) Comparison of averaged heat flux for situations with different tangeld field length scale.

This result demonstrates the link between the number of reconnection sites of the field and heat flux.

We next analyze the temperature equilibration in detail. The averaged temperature difference across the interface is plotted in Figure 4.7(b). It shows the difference between the averaged temperature at the hot side and the cold side. One significant feature in Figure 4.7(b) is that the temperature difference decreases to a steady value T_{end} in all cases. This resembles percolation across a membrane which allows a density jump to happen when filtering two fluids. Figure 4.7(c) shows the distance required for the temperature to drop 80 percent at the interface. This distance characterizes the length of the interaction region. Except for the vertical field case where no heat transfer is allowed, the interface is expanding at different rates for different R values. The expansion for all the cases of nonzero R approaches a steady value which is also a characteristic feature of the temperature equilibration evolution.

We now analyze the modification of magnetic field configuration during the evolution. Throughout our simulations, the local magnetic field is initially a set of complete loops surrounding the interaction region. Once the energy transfer begins, the interaction region tends to expand as discussed previously. This expansion stretches the field lines on the x direction and distorts these circular loops, eventually inducing magnetic reconnection which opens up channels connecting the hot and cold regions. From the current $J_B = |\nabla \times \mathbf{B}|$, we can get information on how tangled the field is. Figure 4.7(d) shows the evolution of the mean value of the strength of $\nabla \times \mathbf{B}$ in the interaction region. We observe that in the vertical and straight field case, $|\nabla \times \mathbf{B}|$ remains constant, but decreases to a fixed value for $R \geq 2$ cases. This means the field in high R cases is straightened by the stretching of the interaction region as seen in Figure 4.7(c). For the $R \leq 1$ cases, we see that $|\nabla \times \mathbf{B}|$ increases. This rise is due to magnetic energy brought in via the cold mass flow and the creation of fine field structures that amplify J_B faster than dissipation caused by interface expansion.

The local field distortion can be clearly demonstrated by studying the energy evolution of magnetic energy stored in different field components. In Figure 4.9(a), we plot the evolution of mean magnetic energy stored in the vertical field $\bar{B}_y^2/2$, compared with $\bar{B}_x^2/2$. We note that the latter includes only the fluctuating contribution to the

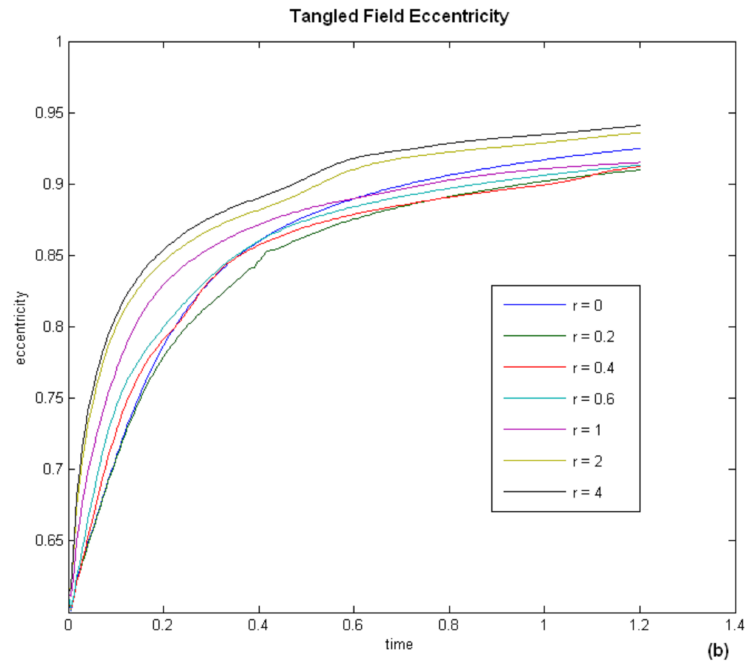
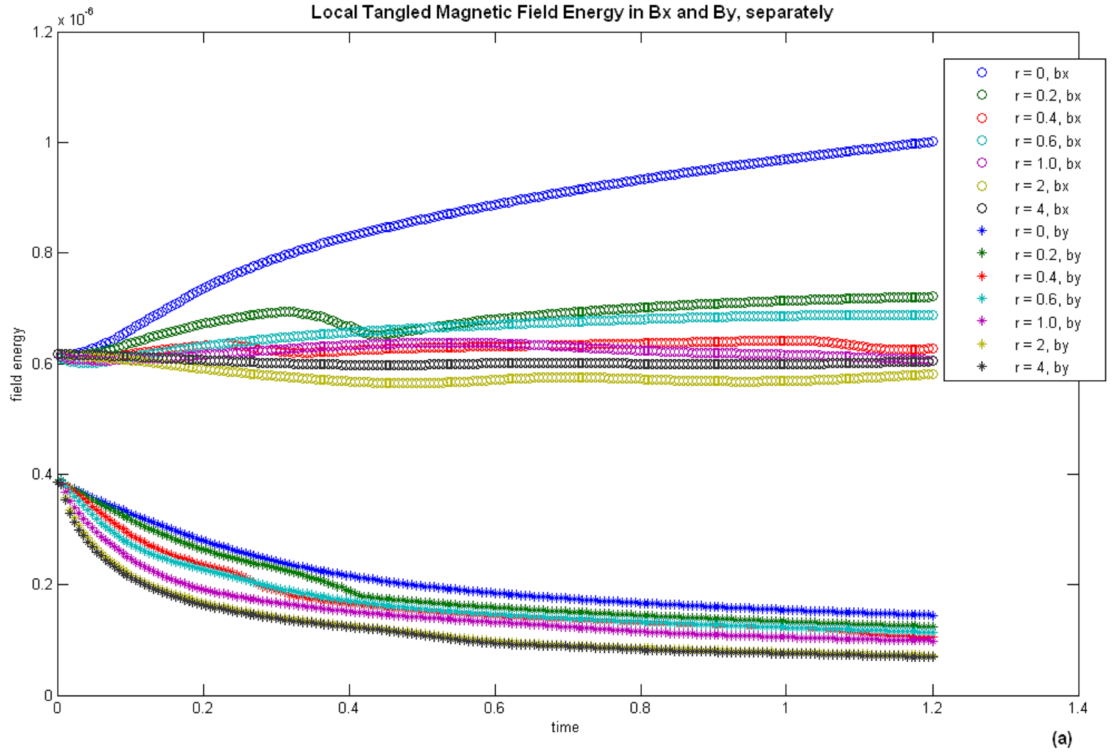


Figure 4.9 (a) Comparison on evolution of local field energy in terms of B_x and B_y . Circles corresponds to the $B_x^2/2$ curve, stars corresponds to the $B_y^2/2$ curve. The different colors denote various R values. (b) Eccentricity of the ellipses constructed by assigning the mean values of local $|B_x|$ and $|B_y|$ to the major and minor axes, respectively. The set of curves show different evolution patterns for different R values.

energy in the x field— that is, the contribution to the horizontal field that does not come from the global mean x component.

From Figure 4.9(a), we observe that the B_y^2 energy decreases while the B_x^2 energy either increases or remains the same for all cases. The magnetic energy evolution can thus be viewed as a conversion of vertical field to horizontal field. This conversion need not conserve the total magnetic energy of the local tangled field because of magnetic reconnection and because material advecting magnetic field can flow in and out of the interaction region. By comparison, in the $R > 1$ cases, the thermal energy and local magnetic energy can both decrease and add to the kinetic energy of the material surrounding the interface, because of the fast thermal diffusion enabled by the strong global field.

The distortion of the local field loops can also be demonstrated by plotting the mean eccentricity of the field loops. In Figure 4.9(b), we plot the mean eccentricity evolution. For all cases, the mean eccentricity is zero initially because of the circular shape of the field loops. Later in the evolution, large R cases tend to evolve into a state of large eccentricity in the steady state. This is caused by a rapid expansion of the interface induced by the strong global field. In short, large R induces more distorted local field loops and less tangled total field due to fast interface expansion, while small R values results in less eccentric local field loops but with more tangled total field and strong magnetic reconnection.

To compute the estimated heat transfer rate in the simulation, we calculate the averaged slope of the curve plotted in Figure 4.7(b), and compare it to the analytic model in Section 4. Although the equilibration rate represented by the slope of the curves in Figure 4.7(b) is changing throughout the evolution, an early phase of the evolution can be chosen when the field configuration has not been modified significantly for which we can then compute the averaged heat transfer rate. By normalizing the resulting heat transfer rate to the isotropic value, we can determine the heat transfer efficiency for different magnetic structures. From figure 4.10, we can see that the analytic prediction and the simulation results agree quite well except for the situation when R is below 0.2. The simulation result does not converge to point (0,0) but ends at an intercept on the y axis. This intercept, which is much larger

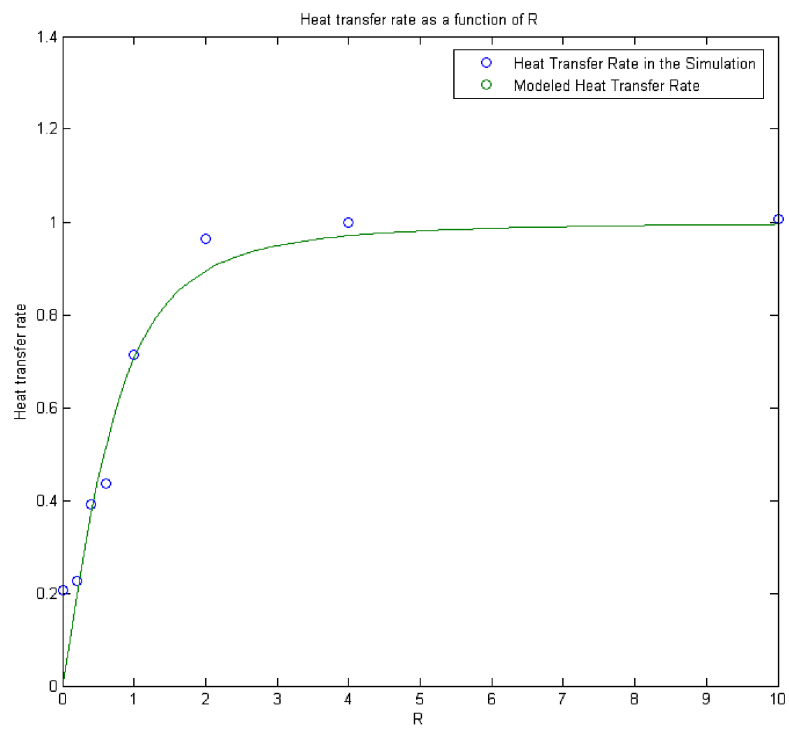


Figure 4.10 heat transfer rate observed in the simulation compared with the analytic model.

compared to both the approximated model and the asymptotic limit ζ_0 , indicates that even if there are initially negligibly few channels for energy transfer, the magnetic reconnection can open up channels and allow heat transfer. Equation 4.9 is valid for predicting the cooling rate of the hot material throughout the early phase of the heat equilibration process. It also provides insight on the strength of the local field in the vicinity of the interface once we know the cooling rate and global magnetic field strength.

It should be pointed out that in our case the electron gyroradius is assumed small compared to the numerical resolution. If we had used an explicit resistivity, then the equivalent assumption would be that the gyro-period is longer than the resistive time on a field gradient scale of order of the gyroradius. The numerical resistivity, which results in numerical reconnection is always present in our simulations and its effect does not seem to depend on resolution: simulations with double resolution shows no significant difference in overall heat transfer efficiency. The existence of numerical resistivity allows the topology of the field to change when scales are approaching the grid scale. As long as this scale is very small compared to global scales, the overall heat transfer rates are not strongly sensitive to this value.

To summarize our results we find first that the average heat flux at the end of our simulations is lower than at the beginning for all R values. Thus we see an approach to thermal equilibrium. In some cases we also see that the heat shows an initially increasing phase denoting a period of active magnetic reconnection.

In the simulations we see the average temperature difference decreases to a constant value T_{end} which is related to R . We also see the width of the initial interface expand to a fixed value during the simulation.

Analysis of the simulation behavior shows that J_B is an accurate measure of structural change in the magnetic field. Current decreases to a constant value for large R cases and increases to a constant value for small R values.

Finally we have shown that equation 4.9 can be used to estimate the energy transfer rate for an initially complicated field structure by considering the relative strength of the local field and the global field. For those cases for which R approaches 0, equation 4.9 becomes invalid since the energy transfer is mainly induced by a

feedback from the magnetic field reconnection. By comparing cases with different field loop length scales, we demonstrate that the smaller the field loop length scale, the faster the reconnection rate.

4.6 Concluding Remarks

In this chapter, we investigated the problem of heat transfer in regions of initially arbitrarily tangled magnetic fields in laminar high β MHD flows through AstroBEAR simulations. The key condition for the magnetic heat flux regulation to occur is that the electron gyroradius needs to be much smaller compared to the electron mean free path. Under such condition, the heat flux is only allowed along the direction of field lines, and thus result in a lower than expected heat transfer efficiency. One of the important results from the simulations is that even if the field loops are locally confined, i.e. its length scale is smaller than the temperature gradient length scale, the hot and cold regions can still exchange heat. This exchange causes pressure imbalance and thus material flow to bend the field lines. In the case of WBB interface with laminar flows, the net effect of this energy exchange is the straightening of the initially tangled field lines, and the reconnection on the field loop length scale. Once the field loops begin to connect regions deep into the hot and cold reservoirs, more energy exchange can happen and eventually making the magnetic field length scale comparable to the temperature length scale, thus reaching a state similar to the non-magnetized case.

We have derived equation 4.9 as an estimate to the heat transfer efficiency through measuring the initial tangled field length scale R .

The issue of magnetized conduction fronts and their mediation of temperature distributions occurs in many astrophysical contexts. One long-standing problem that may involve anisotropic heat conduction are hot bubble temperatures in Wind Blown Bubbles (WBB). WBB's occur in a number of setting including the Planetary Nebula (PN), Luminous Blue Variables (LBVs) and environments of Wolf-Rayet stars. When a central source drives a fast wind ($V_{wind} \sim 500 km/s$) temperatures in the shocked wind material are expected to be of order 10^7 K, which is greater than $2 keV$.

Table 4.1 Scaling of Simulation Parameters

Variables	Computational Units	WBB
Number Density	1	1 cm^{-3}
Temperature	100	1 kev
Domain Length	0.1	0.025 pc
Local Field Strength	10^{-3}	2^{-8} Gauss
Global Field Strength	10^{-4}	2^{-9} Gauss
Evolution Time	1.2	$12,000 \text{ yrs}$
Heat Conductivity	10^{-2}	$2 \times 10^{-18} \text{ cm s g}^{-1} \text{ K}^{-2.5}$

The temperatures observed in many WBB hot bubbles via from X ray emission are, however in the range of 0.5 kev to 1 kev range. NGC 6888 is a particularly well known and well studied example for a WR star (Zhekov & Park (2010)). For planetary nebulae, Chandra X-ray observations have found a number of WBB hot bubbles with temperatures lower than expected based on fast wind speeds (Montez et al. (2005), Kastner et al. (2008)). The role of wind properties and heat conduction in reducing hot bubble temperatures has been discussed by a number of authors (Steffen et al. (2008), Akashi et al. (2007), Stute & Sahai (2007)). The role of magnetic fields and heat conduction was discussed in Soker (1994).

While our simulations herein were meant to be idealized experiments aimed at identifying basic principles of anisotropic heat conduction fronts, we can apply physical scales to the simulations in order to make contact with WBB evolution. Table 4.1 shows the results of such scaling. Upon doing so, we infer that: (1) given field strengths expected for WBB's, heat conduction is likely to be strong enough to influence on the temperature of the expanding hot bubble and the cold shell bounding it. We also note that magnetic fields in WBB (for PN field strengths see Wouter et al. (2006)) are usually in the milli-Gauss range, and are relatively much stronger than the field strength that can be scaled to our simulations. Thus the magnetic field in realistic WBBs is highly likely to result in anisotropy and regulate the behavior of heat conduction. Since the heat transfer does not directly depend on the magnetic β , we can thus apply our analysis to the WBB interface if we approximate the interface to be planar and stationary, which is reasonable as the radius of curvature of WBBs

are much greater than the interface scale of relevance. We must also assume that the global magnetic field is primarily radial.

The computational parameters used in our simulations and the real physics parameters typical in a WBB are listed in the first two columns of table 4.1. We choose the domain length to be $0.025 pc$, which is about 1 percent of the radius of the actual WBB. Table 4.1 shows that by choosing the proper scaling, our simulation fits well with the data observed in a typical WBB. Therefore, the conclusions we draw by analysing the simulation results and the analytical expressions, especially equation 4.9, can be helpful in analyzing WBB evolution.

Chapter 5

MHD Shock-Clump Evolution with Self-Contained Magnetic Fields

5.1 Introduction

The distribution of matter on virtually all astrophysically relevant scales is nonuniform. Within our own galaxy, matter overabundances are found in molecular clouds, and within these clouds matter further is distributed unevenly in the star-forming regions known as molecular cloud cores. Clumps of material exist on smaller scales as well. This heterogeneous distribution of matter is required, of course, for star and planet formation. On the other hand, energetic sources such as young stellar objects (YSOs), planetary nebulae (PNe), and supernovae inject kinetic energy back into their environments in the form of winds, jets, and shocks. On larger cosmological scales galaxies are clustered implying the early evolution of the Universe involved heterogeneous or "clumpy" flows as well. The central regions of active galaxies with their supermassive blackholes are also expected to be home to extensive regions of heterogeneous density distributions with strong incident winds and shocks. Thus understanding how the former (clumps) and latter (winds, jets, and shocks) interact remains a central problem for astrophysics. Since dynamically significant magnetic fields are expected to thread much of the plasma in the interstellar and intergalactic medium the role of magnetic forces on shock clump interactions is also of considerable

interest.

Early analytic studies of single clump/shock interaction focused on the early stages of the hydrodynamic interaction, where the solution remained amenable to linear approximations. The evolution late in time, when the behavior becomes highly nonlinear, remains intractable from a purely analytic standpoint and therefore has benefited greatly from numerical investigation – a review of the pioneering literature may be found in Klein et al (1994) (hereafter KMC94), or Poludnenko et al (2002). Illustrating the maturity of the field, a variety of physics has now been included in the studies. KMC94 discussed systematically the evolution of a single, adiabatic, non-magnetized, non-thermally conducting shocked clump overrun by a planar shock in axisymmetry (“2.5D”). Similar simulations were carried out in three dimensions (3D) by Stone & Norman (1992). The role of radiative cooling [e.g. Mellema et al (2002), Fragile et al (2004)], smooth cloud boundaries [e.g. Nakamura et al (2006)], and systems of clumps [e.g. Poludnenko et al (2002)] have all been studied. A similar problem involving clump-clump collisions, has also received attention [e.g. Miniati et al (1999), Klein & Woods (1998)]. Most studies predominantly use an Eulerian mesh with a single- or two-fluid method to solve the inviscid Euler equations. One notable exception is Pittard et al (2008), who use a “ $\kappa - \epsilon$ ” model to explicitly handle the turbulent viscosity.

As the list of papers described above shows there have been many studies of hydrodynamic shock clump interactions, numerical studies focused on MHD shock-clump interactions have been fewer. Of particular note are the early studies by Mac Low [Mac Low et al (1994)], Jones [Jones et al (1996)] and Gregori [Gregori et al (2000)] which articulated the basic evolutionary paths of a shocked clump with an embedded magnetic field. Further studies at higher resolution Shin et al (2008) or including other physical processes such as radiative cooling Fragile et al (2005) or heat conduction Orlando et al (2008) have also been carried out. In all these studies however the magnetic field was restricted to uniform geometries in which the field extended throughout the entire volume including both the clump, ambient and incident shocked gas. Thus $\mathbf{B}_0 = B_x \hat{\mathbf{i}} + B_y \hat{\mathbf{j}} + B_z \hat{\mathbf{k}}$ where (B_x, B_y, B_z) were constants.

Throughout these studies the role of fields could be traced to the relative impor-

tance of components perpendicular or parallel to the shock normal. The results can be summarized as follows: (1) When the field is parallel to the shock direction, magnetic field is amplified at the head of and behind the clump. The top of the shocked clump is streamlined but there is no significant suppression on the fragmentation of the clump even for low initial magnetic β . (2) When the magnetic field is perpendicular to the shock normal, the field wraps around the clump and becomes significantly amplified due to stretching driven by the shocked flow. In these cases the shocked clump becomes streamlined by field tension and its fragmentation via instabilities can be suppressed even for high initial β cases. Adding radiative cooling into the simulation can further change the shocked behavior as more thin fragments and confined boundary flows, are formed [Fragile et al (2005)]. There are also studies in recent years focusing on the multi-physics aspect of the problem by incorporating the MHD simulations with processes like thermal diffusion, etc [Orlando et al (2008)].

Thus these studies with uniform fields have shown the importance of initial field geometry on the evolution of MHD shocked clumps. The assumption of uniform fields is however an over-simplification to real environments in which clumps most likely have some internal distribution of fields which may, or may not, be isolated from the surrounding environment. The creation of an interior field would likely be linked to ways clumps can be formed. For example shells of magnetized gas can be swept-up via winds or blast waves. If these shells break up via dynamic modes such as the Rayleigh-Taylor (hereafter RT) or Kelvin-Helmholtz (hereafter KH) instabilities then the clumps which form are likely to develop complex internal field topologies. While these fields may stretch into the surrounding medium reconnection can lead to topological isolation. Numerical studies of MHD RT unstable layers relevant to supernova blast waves confirm the development of internal fields [e.g. Jun et al (1995)]. Numerical and high energy density laboratory plasma experiments have also shown how collimated MHD jets can break up into clumps via kink mode instabilities [e.g. Lebedev et al (2005)]. The clumps which form via the instability have been shown to carry complex internal fields.

Another example comes when a cold shell embedded in a hot environment attempts to evolve towards thermal equilibrium via thermal conduction. If the shell

contains an initially tangled field then some of the shell material will be captured in the tangled field region and become disconnected from the background field via anisotropic thermal conduction [Li et al (2012)].

Thus the next level of realism in studies of MHD shock-clump interactions is the exploration of more realistic magnetic fields. Since all studies to date have initialized their simulations with uniform fields, in this work we begin with only interior fields. Our simulation campaign is designed to explore the question: how do more complex field topologies within the clump alter the evolution of shocked clumps. In an effort to isolate important physical processes we choose to use relatively simple interior fields i.e. purely toroidal and purely poloidal both with different alignments to the direction of shock propagation. While we have carried out simulations with random fields we will report the results of those studies in a subsequent paper.

In Section 2 and 3 we describe the numerical method and model. In Section 4 we report our results. Section 5 we provide a analytic model for the evolution field energy that allows us to correctly order the different initial cases and in Section 6 we summarize and provide conclusions.

5.2 Problem Description and Simulation Setup

The initial conditions for the simulations presented in this paper are all based on the same clump/shock/ambient medium, conditions i.e. the clump, ambient and shock conditions are the same. The only variable we explored was the internal magnetic field topology and strength. Our set-up for a torodial magnetic field initial condition is illustrated in figure 5.1.

We choose conditions that are astrophysical relevant with a focus on clumps occurring in interstellar environments. We note however that behavior seen in our model will scale with the appropriate dimensionless numbers. We denote the shock speed by v_s , ambient sound speed by c , clump density by ρ_c , ambient density by ρ_a , clump thermal pressure by P_{th} , the self-contained magnetic field pressure by P_B , clump radius by r_c and radiative cooling length by r_r . Then as long as the Mach number $M = v_s/c$, clump density ratio $\xi = \rho_c/\rho_a$, plasma beta $\beta = P_{th}/P_B$ and cooling

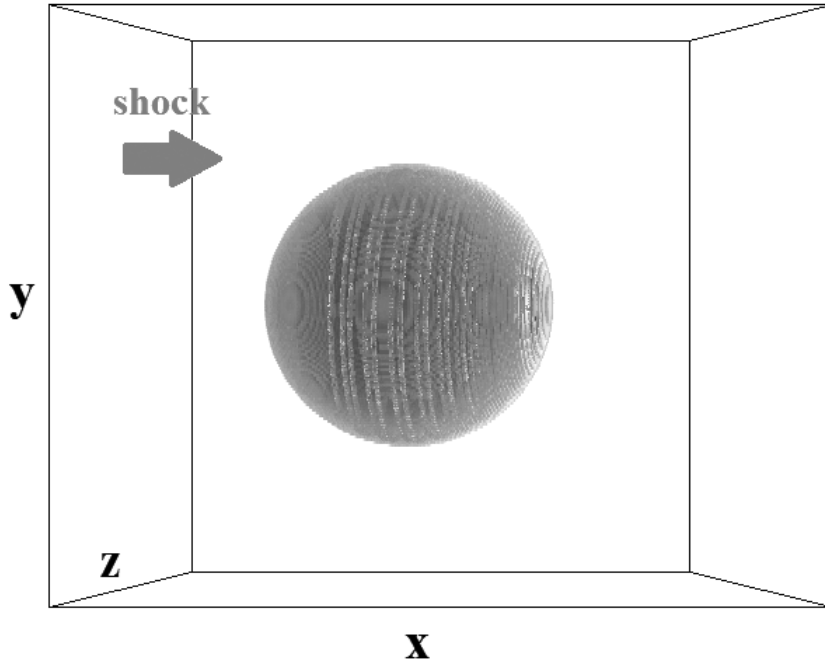


Figure 5.1 The initial setup of the clump simulations. The actual domain is four times as long on x as on y and z . The upcoming planar shock is at the left edge of the domain, propagating rightward along the x axis. The stripes on the clump surface denote a self-contained toroidal magnetic field with its axis aligned with x axis inside the clump.

parameter $\chi = r_c/r_r$ are the same between two runs then the solutions should be independent of absolute scales for input parameters.

Thus we choose an ambient gas that is non-magnetized and isothermal, with a particle number density of 1cc^{-1} and a temperature of 10^4K . Our clump begins with a radius of $r_c = 150\text{a.u.}$ and is in thermal pressure equilibrium with the ambient medium. The clump has a density contrast of $\xi = 100$, i.e., particle number density of 100cc^{-1} and a temperature of 100 K . The domain is a box with dimensions $2400\text{a.u.} \times 60\text{a.u.} \times 60\text{a.u.}$, with an resolution of $1296 \times 324 \times 324$, which gives 54 cells per clump radii. We use outflow boundary conditions on the six sides of the box. We are thus able to follow the evolution for approximately 16 clump radii.

The magnetic fields in our clumps were chosen to allow for self-contained geometries. We use β_{avg} to denote the ratio of thermal pressure to averaged magnetic pressure across the entire clump, that is

$$\beta_{avg} = \frac{P_{th}}{P_{B,avg}} \quad (5.1)$$

where $P_{B,avg}$ denotes the average magnetic field pressure inside the clump. The detailed setup of the self-contained magnetic field is described in Appendix A.

To better characterize the initial magnetic field configuration, we use a dimensionless number η to define the ratio of magnetic energy of the field component that is perpendicular to the shock propagation direction. If the average magnetic field energy density for the initial setup is $B_0^2/8\pi$, then the perpendicular component has an average magnetic field energy density of $\eta B_0^2/8\pi$, while the parallel component has an average magnetic field energy density of $(1 - \eta)B_0^2/8\pi$. η for different initial magnetic field setup is summarized in table 5.1.

Throughout the paper, we use β_{avg} as a measure of dynamical importance of the self-contained magnetic field, and investigate the shocked behavior of situations where the self-contained field is either strong or weak. We will refer to the simulations with $\beta_{avg} = 0.25$ as "strong" field cases and those with $\beta_{avg} = 1.0$ as "weak" field cases throughout the paper. The orientation of the magnetic field relative to the incident shock is another critical parameter. This was already seen in the uniform field simulations described in the introduction. In our simulations, we focus on the cases

Table 5.1 Simulation Setups

Code	β_{avg}	Field Configuration	Field Orientation (related to shock normal)	η
TAS	0.25	<i>toroidal</i>	aligned	1
TPS	0.25	<i>toroidal</i>	perpendicular	0.5
PAS	0.25	<i>poloidal</i>	aligned	0.25
PPS	0.25	<i>poloidal</i>	perpendicular	0.75
TAW	1	<i>toroidal</i>	aligned	1
TPW	1	<i>toroidal</i>	perpendicular	0.5
PAW	1	<i>poloidal</i>	aligned	0.25
PPW	1	<i>poloidal</i>	perpendicular	0.75

when the self-contained magnetic field is either purely poloidal or purely toroidal. For these field configurations which possess an axial symmetry, it will be the orientation of the field axis \mathbf{b} to the shock normal \mathbf{n} which matters. For each configuration we run both parallel $\mathbf{b} \cdot \mathbf{n} = 1$ and perpendicular cases $\mathbf{b} \cdot \mathbf{n} = 0$. The complete set of runs presented in this study are described and coded in table 5.1 and these orientations are presented visually in figure 5.2.

We do not begin our simulations in a force free state as it is not clear that this is the most generic astrophysical situation. Clumps created in dynamic environments subject to repeated incident flows may not have time to relax to force free conditions. Thus we expect the clump will be deformed by the self-contained field on the time scale of

$$\tau_B = \frac{r_c}{u_A} \approx 276 \text{yrs}, \quad (5.2)$$

where u_A is the Alfven speed of the self-contained field calculated from the average magnetic energy density inside the clump. In our simulations the clump evolution driven by the shock is always faster than or comparable to this timescale as we discuss below.

The incoming shock has a Mach number $M = 10$ which puts our simulations in the strong shock regime (KMC94). To understand the role of the magnetic fields we identify the clump crushing time scale as

$$\tau_{cc} = \frac{\sqrt{\chi} r_c}{v_s} \approx 95 \text{yrs}. \quad (5.3)$$

Thus $\tau_{cc} < \tau_B$ and we expect that the strong shock dynamics driven by the trans-

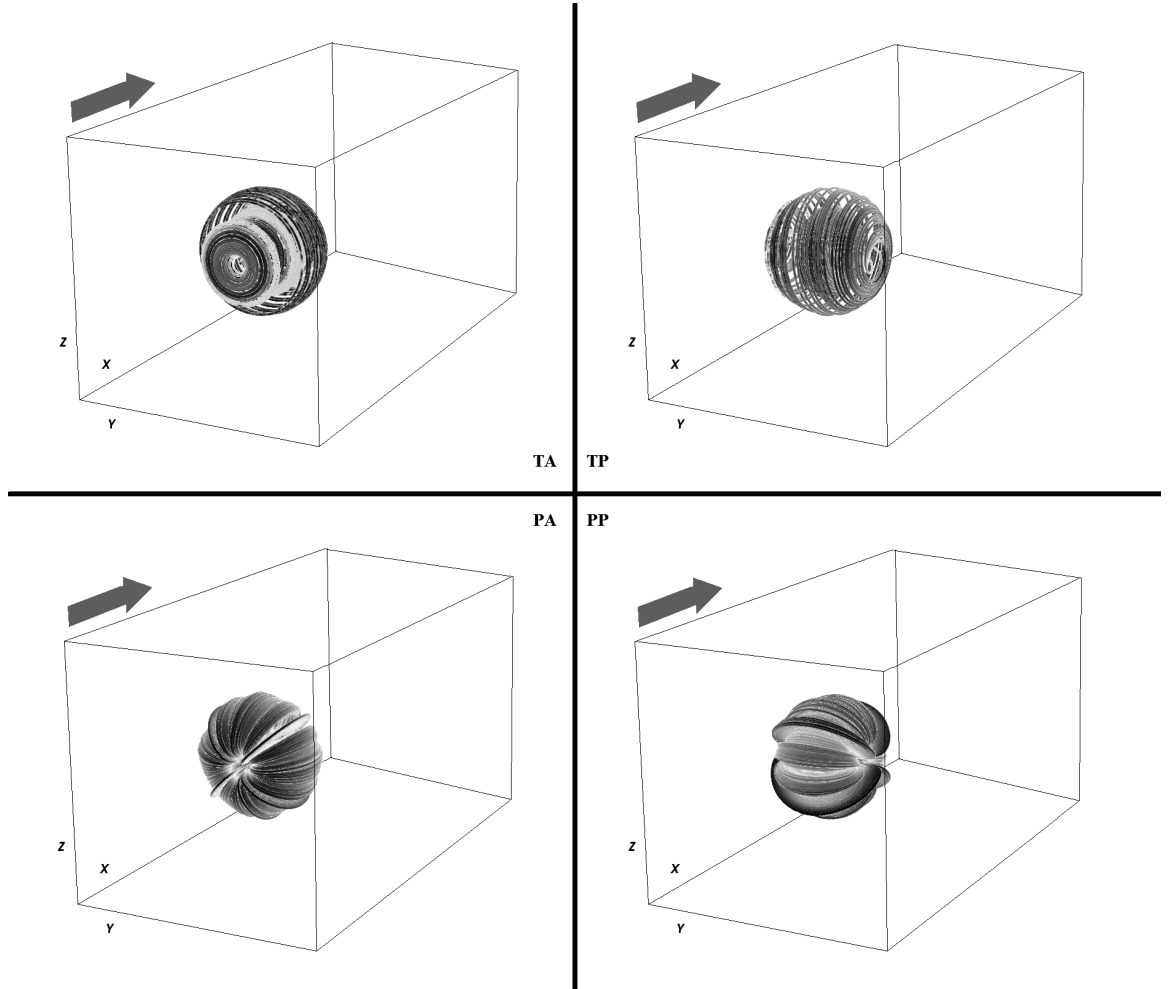


Figure 5.2 The initial setup of the clump magnetic field. The actual domain is four times as long on x as on y and z . The first letter denotes the field configuration: T for toroidal only; P for poloidal only. The second letter denotes the field orientation with respect to the shock propagation direction: A for aligned; P for perpendicular. The blue arrow denotes the shock direction.

mitted wave propagating into the clump will dominate over any relaxation driven effects from the internal magnetic field. To confirm this we also define energy parameters of the shock clump interaction where $\sigma_{th} = K_s/E_{th}$ and $\sigma_B = K_s/E_B$. These are ratios between shock kinetic energy density $\propto \rho_s v_s^2$ and the thermal or average magnetic energy density contained in the clump, respectively. From parameters for our simulation we then have $\sigma_{th} \approx 222$ and $\sigma_B \approx 33$. Thus, although the clump is initially magnetically dominated, the shock has higher energy densities than either the thermal or magnetic energy contained inside the clump. Given these conditions and our choice of $\tau_{cc} < \tau_B$ we expect that most of the simulation evolution will be driven by the shock and not internal relaxation.

We note that the cooling time scale for the transmitted shock $\tau_r = E_t/\dot{E}_t = kT_p/n\Lambda$ is below the clump crushing time to ensure noticeable cooling and is given by

$$\tau_r \approx 48 \text{yrs} \ll \tau_{cc}. \quad (5.4)$$

Therefore we are in the regime of “weakly cooling” inside the clump where the magnetic energy is concentrated, i.e., for the transmitted shock, the ratio of cooling time against crushing time $\chi = \tau_r/\tau_{cc} < 1$. The cooling length scale can be calculated as:

$$l_r = v_{ps}\tau_r \quad (5.5)$$

where v_{ps} is the post-shock sound speed:

$$v_{ps} = \sqrt{\frac{\gamma k_B T_{ps}}{m_A}} \quad (5.6)$$

From the above equations, we can calculate the ratio of the clump radius to the cooling length behind the transmitted shock:

$$\chi_* = r_c/l_r \approx 5.64 \quad (5.7)$$

Therefore one clump radius contains 5 cooling length scales. The bow shock in our simulations has a cooling time that is longer than the evolutionary timescale of the flow and remains adiabatic in its dynamics. Notice that although the situation we consider here is freely scalable, the condition “weakly cooling” should always be

satisfied. Since the cooling length scale does not depend on the size of the clump, it can become extremely small comparing to the clump radius when the scale length is increased and thus become a dominating process after applying such a scaling.

In order to ensure $\nabla \cdot \mathbf{B} = 0$, the self-contained magnetic field is set up by first choosing a vector potential distribution, and then taking its curl. The geometry of the toroidal field is best demonstrated using the cylindrical coordinates. The vector potential \mathbf{A} has the following distribution:

$$A_r = 0 \quad (5.8)$$

$$A_\theta = 0 \quad (5.9)$$

$$A_z = \begin{cases} B_{0,tor} \frac{f\sqrt{r_c^2 - z^2} - r^2}{2fr_c}, & \text{if } r \leq f\sqrt{r_c^2 - z^2} \\ B_{0,tor} \frac{(\sqrt{r_c^2 - z^2} - r)^2}{2(1-f)r_c}, & \text{if } r > f\sqrt{r_c^2 - z^2} \end{cases} \quad (5.10)$$

where $B_{0,tor}$ is the desired peak magnetic field intensity, and r, θ, z take their usual meanings in a cylindrical coordinate system: r is the distance to the z -axis; θ is the azimuthal angle; z is the distance to the $x - y$ plane. $f < 1$ is an attenuation factor to cut off the magnetic field when $\sqrt{r^2 + z^2} > r_c$, i.e. outside the clump. This vector potential distribution gives the following \mathbf{B} distribution upon taking the curl:

$$B_r = 0 \quad (5.11)$$

$$B_\theta = \begin{cases} B_{0,tor} \frac{r}{fr_c}, & \text{if } r \leq f\sqrt{r_c^2 - z^2} \\ B_{0,tor} \frac{\sqrt{r_c^2 - z^2} - r}{(1-f)r_c}, & \text{if } r > f\sqrt{r_c^2 - z^2} \end{cases} \quad (5.12)$$

$$B_z = 0 \quad (5.13)$$

For any given z , the magnetic field intensity peaks at $f\sqrt{r_c^2 - z^2}$. If f is close to 1, the field will be concentrated near the outer edge of the clump. In the presented simulations, we take $f = 0.9$.

The poloidal field is best demonstrated using the spherical coordinates. It has a vector potential distribution of:

$$A_r = 0 \quad (5.14)$$

$$A_\theta = -\frac{B_{0,pol}(r_c - r)^2 r \sin\theta}{2r_c^2} \quad (5.15)$$

$$A_\phi = 0 \quad (5.16)$$

where $B_{0,pol}$ is the desired peak magnetic field intensity, r, θ, ϕ are the distance to the origin, the polar angle and the azimuthal angle respectively. Notice here r and θ are defined differently compared to cylindrical coordinates. The curl of this vector field is:

$$\mathbf{B}_r = 0 \quad (5.17)$$

$$\mathbf{B}_\theta = 0 \quad (5.18)$$

$$\mathbf{B}_\phi = -\frac{B_{0,pol}(r_c - r)(r_c - 3r)\sin\theta}{r_c} \quad (5.19)$$

We observe that the magnetic field energy density \mathbf{B}^2 peaks at the center $r = 0$ and has a weaker secondary maximum at $r = 2r_c/3$. The field attenuates to zero at the outer edge of the clump $r = r_c$. There is another zero point in between $r = 0$ and $r = r_c$: $r = r_c/3$. The toroidal and poloidal field setup are orthogonal to each other, and can be combined into a more general self-contained magnetic field distribution. The cases presented in our paper form the basis to understand more complex self-contained magnetic field configurations.

We run the simulation from time $t = 0$ to time $t \approx 333\text{yrs}$ or $t \approx 3.5\tau_{cc}$. We will use the clump crushing time τ_{cc} as our unit of time throughout the rest of the paper.

5.3 Simulation Results

5.3.1 Shocked clumps with a self-contained strong ordered field

We begin with the simulations in which the internal self-contained magnetic field is relatively strong ($\beta_{avg} = 0.25$). Recall in what follows that the incident shock kinetic energy is dominant in the initial interaction even though the clump is magnetically dominated in terms of its own initial configuration. Figure 5.3 shows case TAS: i.e. the internal magnetic field is toroidal and aligned with the shock normal. Panels run from top to bottom and correspond to different evolutionary times: $t = (\tau_{cc}, 2\tau_{cc}, 3.5\tau_{cc})$.

At early times, $t \leq \tau_{cc}$, the shocked clump evolution appears similar to that of the unmagnetized case (not shown). The usual pair of shocks form: a bow shock facing into the incoming flow and a transmitted shock which propagates into the clump. Note that the transmitted shock in our simulations is radiative meaning that thermal energy gained at the shock transition is quickly radiated away. With the loss of thermal pressure support the shock collapses back towards the contact discontinuity. In this regime shock regions becomes thin and post-shock densities are high [Yirak et al (2010)]. In our simulations, only the bow shock cools effectively which is evident at the thin boundary flows.

The effect of the toriodal field becomes particularly apparent in the morphology after a crushing time. At the middle frame in figure 5.3 ($2\tau_{cc}$) we see the clump collapsing towards the symmetry axis due to the pinch by the toriodal magnetic field. This behavior is in contrast to the hydrodynamic or MHD adiabatic case with parallel fields in which the shocked clump material expands laterally and is then torn apart by RT instabilities. Even in radiative hydrodynamic cases the shocks tend to flatten the clump which then break up into clumps [Yirak et al (2010)]. Only in uniform perpendicular field cases do we see situations where the flow becomes shielded from RT instabilities. The internal toriodal field simulations show something different entirely however. Here the tension force from the compressed internal toriodal field is strong enough to suppresses the lateral expansion. This inward directed tension controls the subsequent evolution.

The ongoing compression within the clump driven by the tension of the toriodal field restricts the downstream flow. Thus only a limited turbulence wake forms. The compression of the clump and downstream flow into a narrow cone continues at later times as can be seen in the frame corresponding to $t = 3.5\tau_{cc}$. By this time shocked clump has become compressed into a very narrow conical feature resembling the "nose cone" observed in the MHD jet simulations [e.g. Frank et al (1998), Lind et al (1989)]. The development of an dense streamlined clump by the end of the simulations indicates that for these configurations the long term evolution will be simply slow erosion of the clump without significant fragmentation.

When the toriodal axis is perpendicular to the shock normal however the evolution

is quite different. In figure 5.4 we show 3 snapshots of density for run TPS. In this case the field is attempting to pinch the clump onto z axis (a compression "inward" towards the clump axis along the x and y directions). The shock however only produces a compression along the x axis. The differential forces on the clump do yield on transient period of flattening as is seen in both hydrodynamic and uniform field MHD simulations. However the presence of the internal toroidal fields alters the internal distribution of stresses. The result is a differential aerodynamical resistance to the flow over the clump as it becomes immersed in the post-shock region. Note that the magnetized clump is easier to distort along z axis compared to y axis where tension forces are at work. Thus at $t = \tau_{cc}$ we see the clump becoming ellipsoidal or football shaped. The structural coherence that the tension force provides in y direction during the compression phase continues to shape the subsequent flow evolution. By $t = 2\tau_{cc}$ oblate clump which continues to be eroded by the incoming wind begins developing a concave morphology along the z axis. The subsequent formation of a "banana" shaped configuration tilts the field along the body of the clump shifting the position of the local toroidal axis relative to the incident flow. Thus the clump begins to fragment mostly along the z axis because of a lack of field tension in this direction. In addition a ring-like feature develops along the outer extent of the clump where the field is initially concentrated. By the end of the simulation, the clump has fragmented along the z axis from erosion and cooling, and evolves to an array of cold, magnetized "clumplets".

Note that the perpendicular toroidal case produces a turbulent wake that occupies a much larger volume than the parallelly oriented case. As we will see the development of such an extended wake is well-correlated with the degree of mixing between clump and ambient medium.

We now turn to the poloidal strong field cases. Figure 5.5 shows the simulation of a shocked clump when the internal field is poloidal and aligned with the the shock normal (case PAS). In this run, there is a strong field concentration of field at the clump axis, as well as a relatively weak field near the clump surface. When the axis is aligned with the shock normal, we can see that during the compression phase $t = \tau_{cc}$, the clump is compressed radially as in the unmagnetized case. Note however that

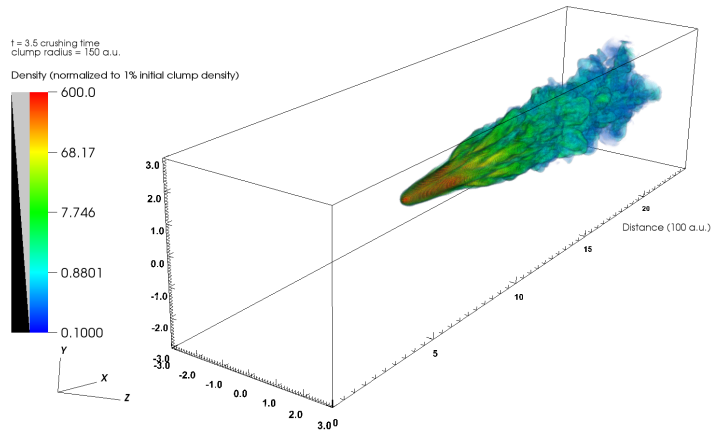
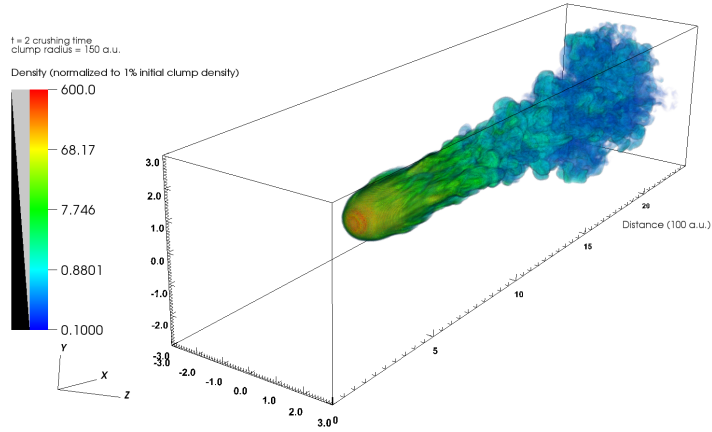
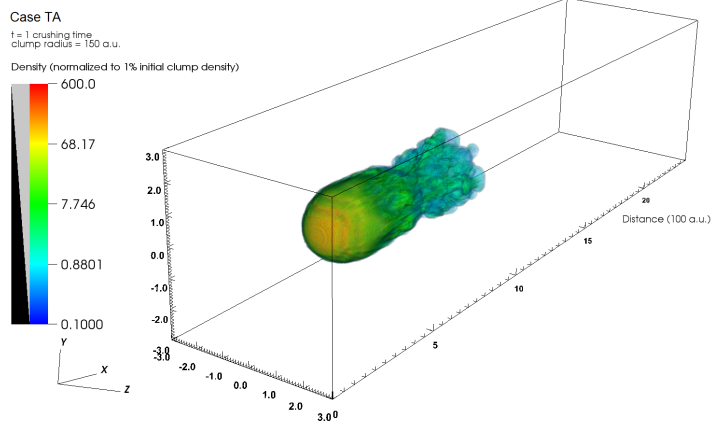


Figure 5.3 Case of strong toroidal only, aligned with shock normal. Evolution of clump material at 1, 2 and 3.5 clump crushing time. The color indicates clump material concentration, normalized by initial value.

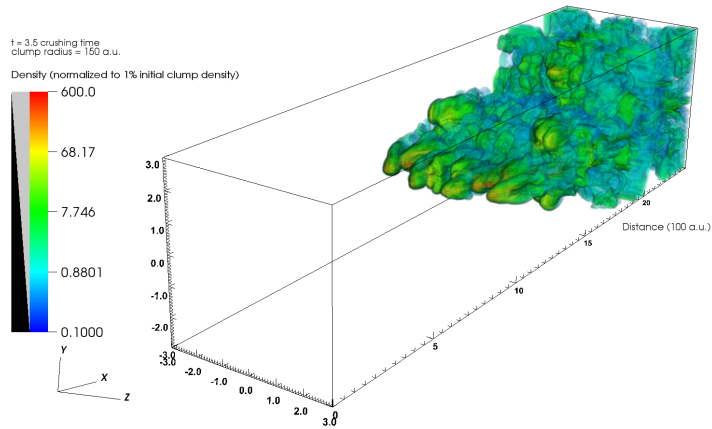
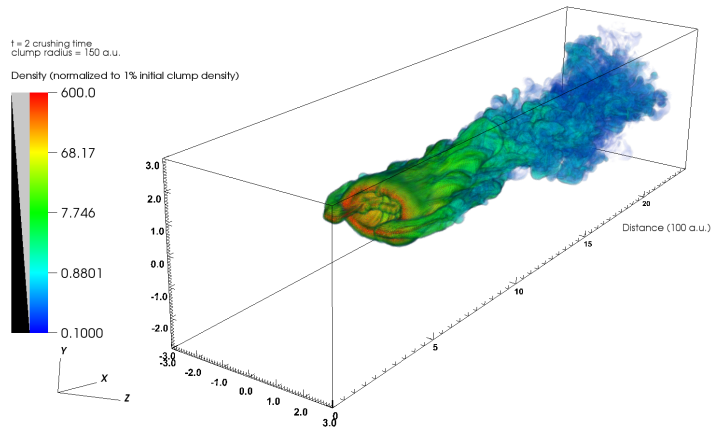
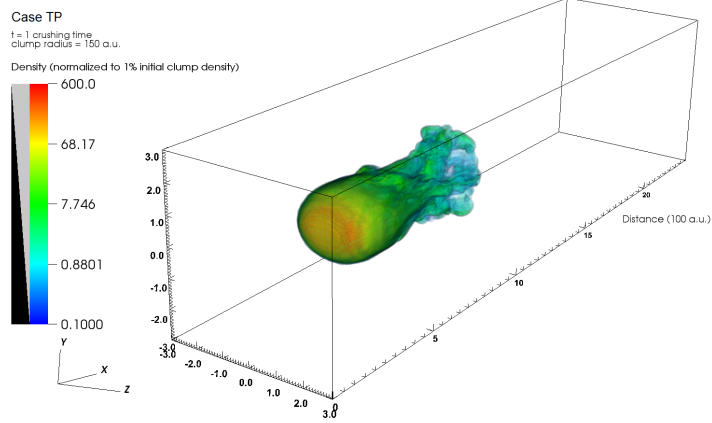


Figure 5.4 Case of strong toroidal only, perpendicular to shock propagation direction. Evolution of clump material at 1, 2 and 3.5 clump crushing time. The color indicates clump material concentration, normalized by initial value.

a depression develops along the clump axis as the incident flow's ram pressure is relatively unimpeded there by the magnetic field. Because the field along the axis is aligned with the flow direction, the evolution resembles the global field parallel case [Mac Low et al (1994)]. However, by $t = 2\tau_{cc}$ the differential stresses of internal self-contained poloidal field yield a different evolution compared to both our previous toroidal cases and the uniform field cases.

While the clump expands laterally as in the unmagnetized case, it then develops a hollow core. The initial phase of the axial core were already apparent at the earlier times however now we see that the outer regions corresponding to the domains closer to the clump surface with relatively strong magnetic field retain (weaker than the field on the axis, but stronger than the region surrounding the $r_c/3$ point. See Appendix A) their coherence while the incident flow has evacuated the area surrounding the axial core. Thus the poloidal field yields a coherence length associated with the curvature (and tension) of the field around its circumference. Regions closer to the axis with weak initial field get distorted, compressed and driven downstream while the regions with a strong field or fully flow-aligned field better resist the compression.

The "shaft" shaped feature surrounded by the hollow core has a relatively low β compared to the rest of the clump. It gradually deforms as a result of field line tension (squeezing outwards towards the clump periphery away from the axis) on the timescale of $t = \tau_B$, which for these runs is $2.8\tau_{cc}$. Consequently we see at the last frame $t = 3.5\tau_{cc}$, that the "shaft" disappears and the clump is fragmented into an array of cold, magnetized "clumplets", similar to the TP case.

Figure 5.6 shows the simulation with a strong internal poloidal field oriented perpendicular to the shock normal (coded PPS). The influence of the different field orientation is already evident at the first frame $t = \tau_{cc}$. The initial compression phase has produced an ellipsoidal clump distribution in a similar manner as the toroidal perpendicular simulation (Figure 5.4). In this case the internal stresses of the poloidal field change the oriental of the ellipse while also producing substructure due to the smaller scale of field loops ($R \sim 0.5r_c$ for the poloidal field rather than $R \sim r_c$ for the toroidal case). By $t = 2\tau_{cc}$ we see a "shaft" and a "ring" structure develop as in the PAS case, but now the smaller scale of the loops (radius of curvature) allow

these structures to be partially eroded by the incoming shock. The "shaft" is then fragmented by the shock rather than the field pinch, and the "ring" leaves an extended U-shape structure. As a result, two large clumplets located on the $y - z$ plane form at $3.5\tau_{cc}$. For configurations TA and PP, the initial setup is entirely axisymmetric.

5.3.2 Shocked clumps with a weak self-contained ordered field

We now look at the results where the contained magnetic field is relatively weak compared with the previous cases ($\beta_{avg} = 1$). In this regime we still expect to see the field exerting influence over the shock clump evolution but the final outcome on the flow, in terms of global properties, may not sort cleanly between different initial field configurations.

Figure 5.7 shows the simulation of a shocked clump when the internal field is torodial and aligned with the the shock normal (coded TAW). Here, the most significance difference comparing to the TAS case is that the post-shock clump material does not collapse into a core, instead the ram pressure of the incident flow pushed through the clump axis after the initial compression phase $\tau_{cc} < t < 2\tau_{cc}$. This indicates that the pinch force provided by the toroidal field no longer overwhelms the stresses produced by the flow as it does in the case with stronger initial field and lower initial σ_B . By $3.5\tau_{cc}$, the clump evolves into a series of cold dense clumps as in the hydrodynamic case although the position of the clumps appears to reflect the original toroidal orientation of the field.

Figure 5.8 shows the case of weak internal toroidal field with its axis perpendicular to the shock normal (coded TPW). Compared to the TPS case in the previous subsection, we can see that the clump opens up at $t = 2\tau_{cc}$ similar to the TAW case because of the lack of strong pinch forces. One can still see the the effect of the field in the orientation of the two nascent clumps forming aligned with the z-axis. Indeed by $3.5\tau_{cc}$, the clump material forms an array of "clumplets" with a stronger distribution along z axis than in x or y which is similar to TPS case. Thus like the TAW case even a weaker self-contained magnetic field still yields an influence over the global

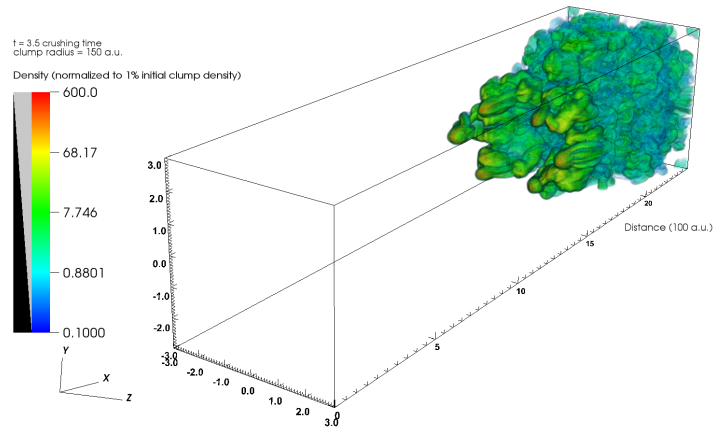
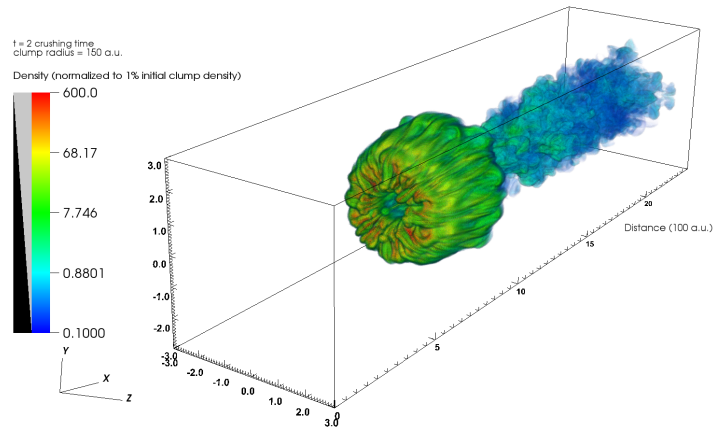
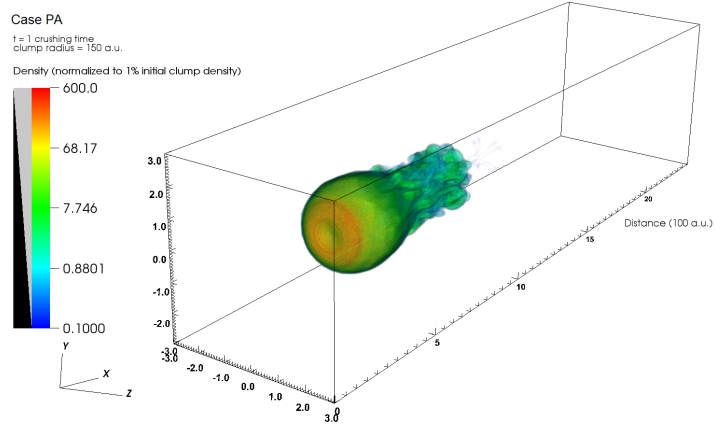


Figure 5.5 Case of strong poloidal only, aligned with shock normal. Evolution of clump material at 1, 2 and 3.5 clump crushing time. The color indicates clump material concentration, normalized by initial value.

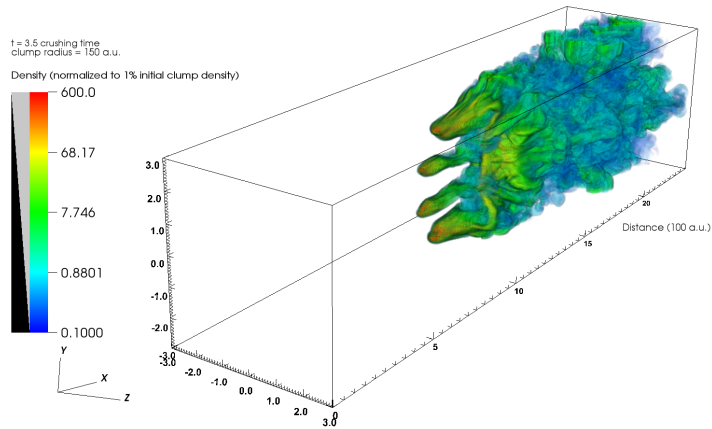
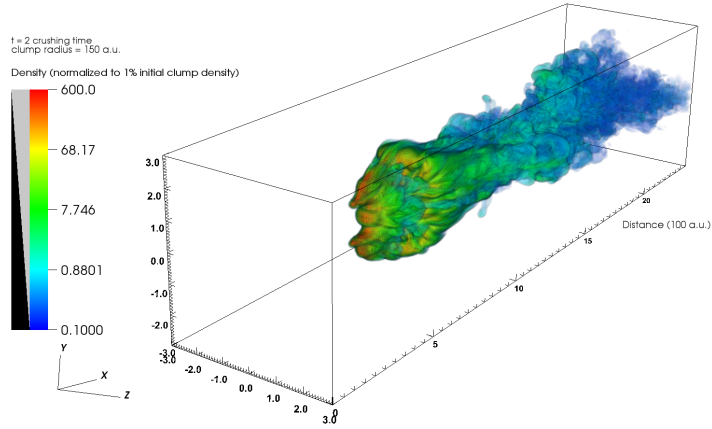
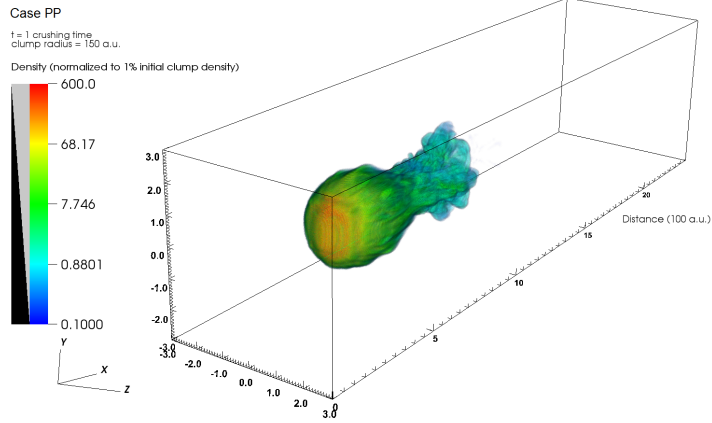


Figure 5.6 Case of strong poloidal only, perpendicular to shock propagation direction. Evolution of clump material at 1, 2 and 3.5 clump crushing time. The color indicates clump material concentration, normalized by initial value.

flow evolution.

Figure 5.9 shows the simulation of a shocked clump when the internal field is poloidal and aligned with the the shock normal (case PAW). Here the initial morphological evolution is similar to that of the PAS case (Figure 5.5): at $2\tau_{cc}$, a "shaft" feature is formed, with a "ring" shaped feature surrounding it. By $3.5\tau_{cc}$, the shaft is destroyed by the internal pinching and the "ring" feature fragments into an array of clumplets due to field pinching and cooling. Notice that the size of the "ring" feature and the spread of the resulting clumplets is smaller compared to the PAS case: an effect that can be attributed to the weaker initial field and its resulting hoop stresses.

In Figure 5.10 we show the simulation with a weak internal poloidal field oriented perpendicular to the shock normal (case PPW). The evolution is comparable with the PPS case. Once again the U-shaped feature which forms after the shock has passed through the entire clump is less pronounced due to reduced pinch forces. Note that we see that the final fragmentation produces two large clumplets at $3.5\tau_{cc}$.

The overall evolution of the weaker field cases shows the effect the field has in terms of the final spectrum of fragments produced by the shock-clump interactions. Unlike purely hydrodynamic cases the fragmentation of the initial clump into smaller "clumplets" does depend on the the initial field geometry and its orientation relative to the incident shock at least for the evolutionary timescales considered in this study. Thus even in cases where the field does not dominate the initial energy budget of the clump, the shock dynamics does depend on the details of the initial field. Note also that in all cases a nearly volume filling turbulent wake develops behind the clump at later evolutionary times. For TA and PP configurations, the initial setup is axisymmetric. But as a result of numerical instabilities and finite domain size, we can observe asymmetry at late frames in Figures 3, 5, 7 and 9.

Magnetic fields can be important in suppressing the instabilities associated with shocked clumps. According to Jones et al (1996), the condition for the magnetic field to suppress the KH instability is that $\beta < 1$ for the boundary flows. The condition for the magnetic field to suppress the RT instability is that $\beta < \xi/M = 10$. For both strong and weak field cases presented in our paper, the β at the boundary flows has a value between 1 and 10. Therefore the KH instability is present in all of our

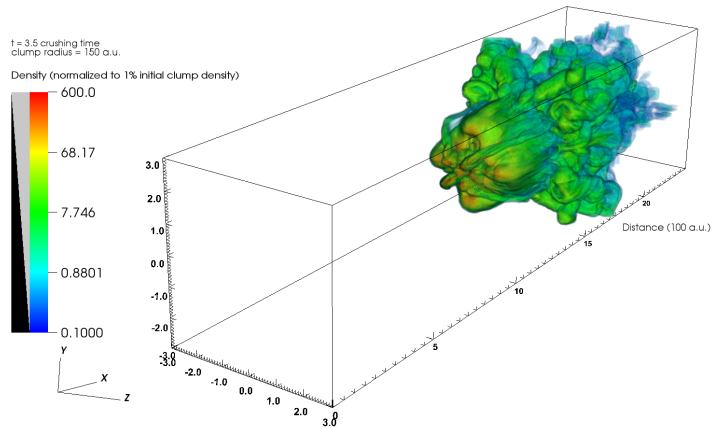
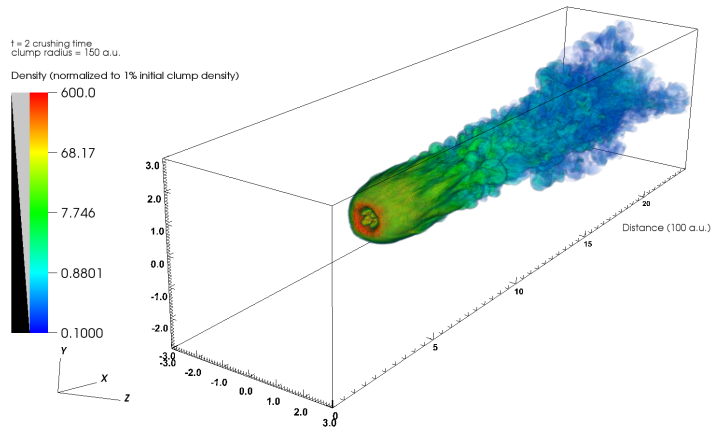
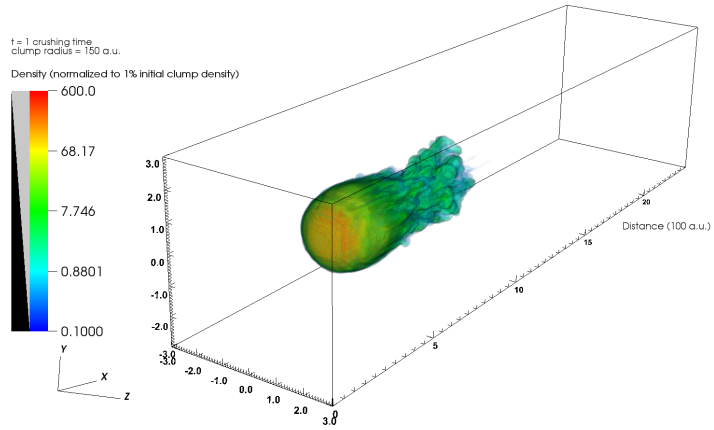


Figure 5.7 Case of weak toroidal only, perpendicular to shock propagation direction. Evolution of clump material at 1, 2 and 3.5 clump crushing time. The color indicates clump material concentration, normalized by initial value.

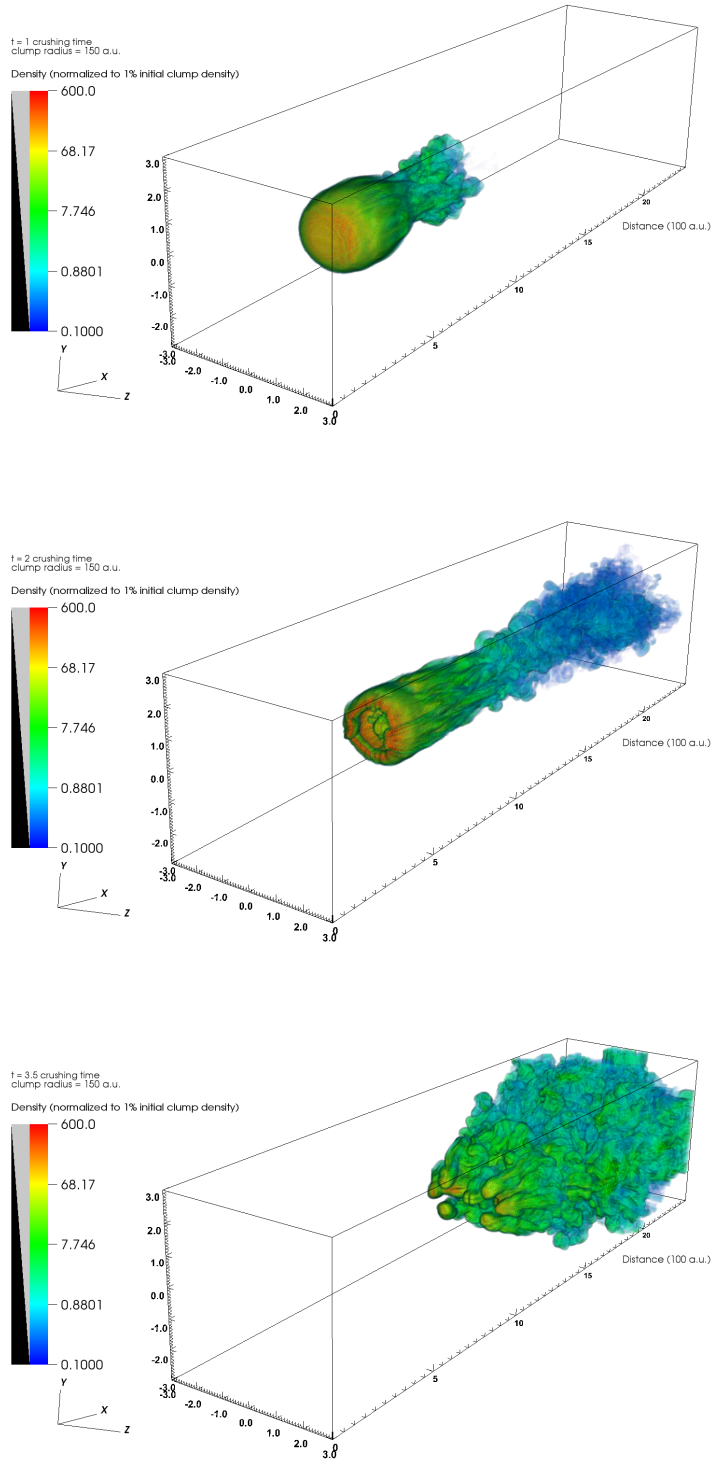


Figure 5.8 Case of weak toroidal only, perpendicular to shock propagation direction. Evolution of clump material at 1, 2 and 3.5 clump crushing time. The color indicates clump material concentration, normalized by initial value.

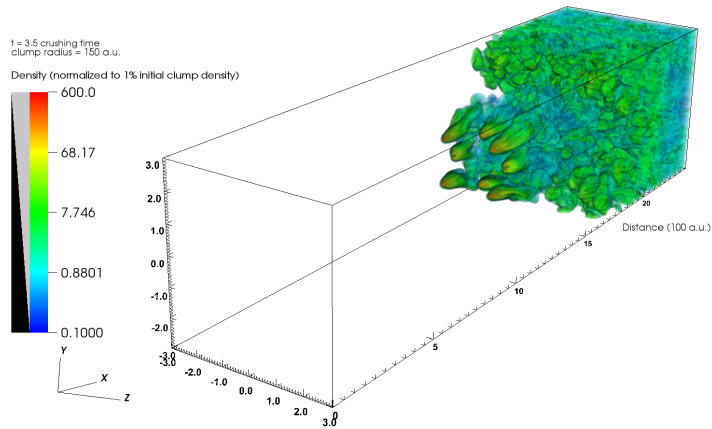
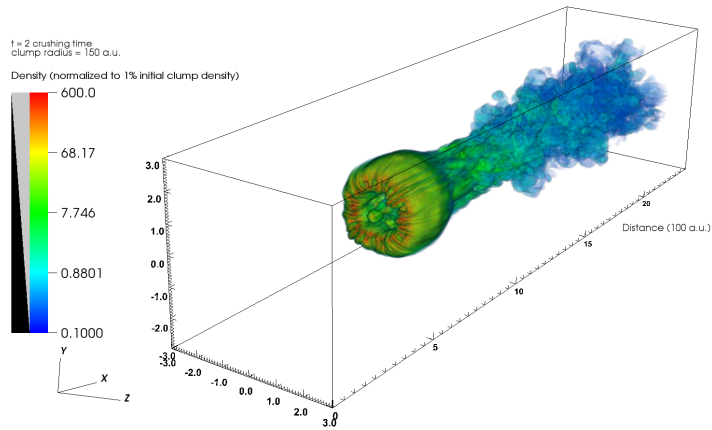
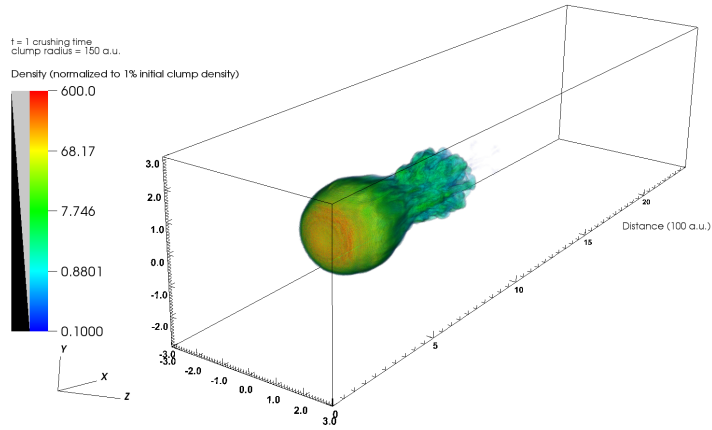


Figure 5.9 Case of weak poloidal only, aligned with shock normal. Evolution of clump material at 1, 2 and 3.5 clump crushing time. The color indicates clump material concentration, normalized by initial value.⁷⁵

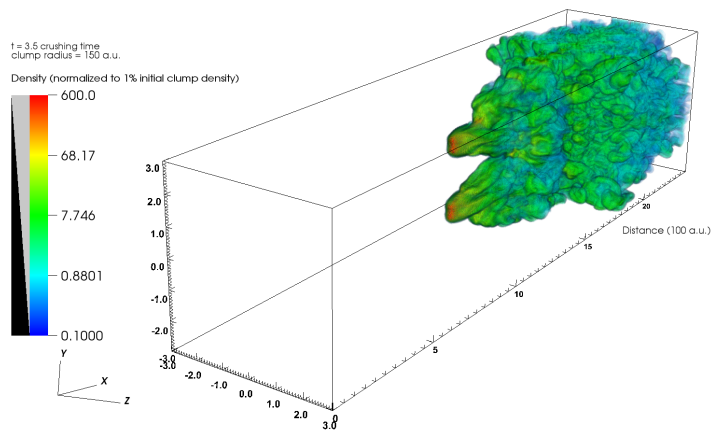
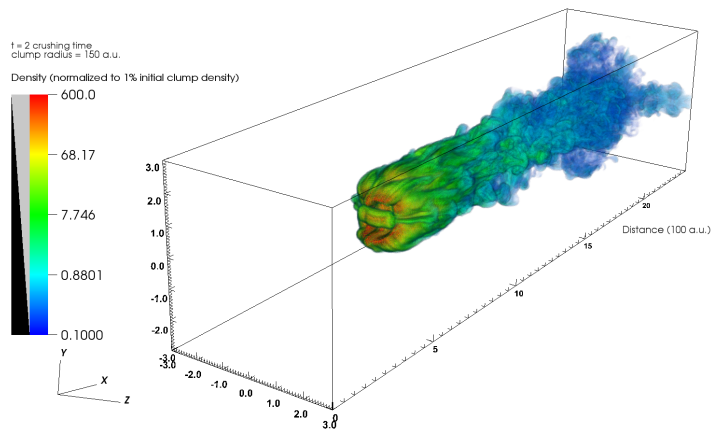
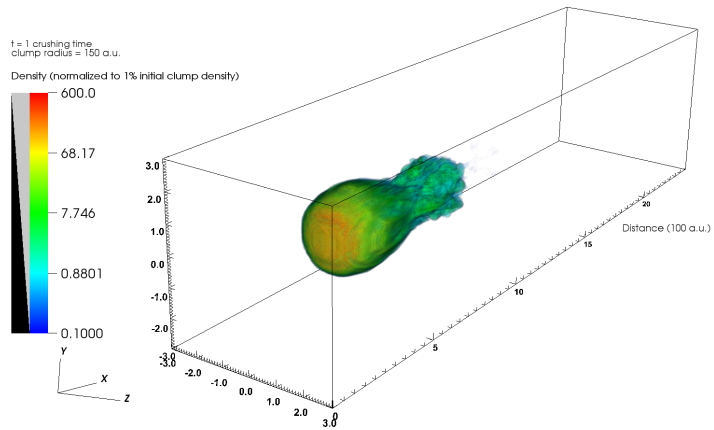


Figure 5.10 Case of weak poloidal only, perpendicular to shock propagation direction. Evolution of clump material at 1, 2 and 3.5 clump crushing time. The color indicates clump material concentration, normalized by initial value.

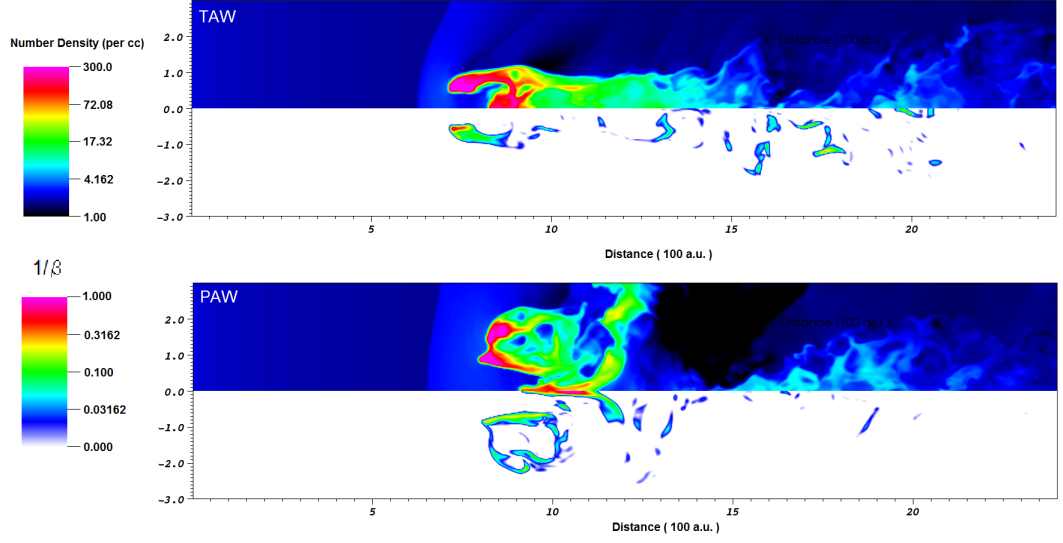


Figure 5.11 Snapshot of shocked clumps cutthrough the center of the domain, at $t = 2.5\tau_{cc}$, for the TAW and PAW cases. The upper panel corresponds to the density, the lower panel corresponds to $1/\beta$.

cases, shredding the clump boundary flows and converting them into downstream turbulence. However, even for the weak self-contained field cases, the RT instability is suppressed. To demonstrate, we map the density and β (presented by $1/\beta$ in figure 5.11) for TAW and PAW cases in figure 5.11. We observe that the shocked clump material develops a streamlined shape in both cases. The region where density is concentrated has $1/\beta > 0.1$.

Finally to illustrate the post-shock distribution of magnetic field, we plot the density and field pressure by cutting through the $x - y$ mid plane of the simulation box in figure 5.12. It shows that the field follows the clump density distribution, as is expected in our simulations where the diffusion is only numerical and weak.

5.4 Mathematical Model and Analysis

Figure 5.13(a), (b) show, for the strongly magnetized clump cases, the evolution of kinetic energy and total magnetic energy respectively. Figure 5.14 shows the the

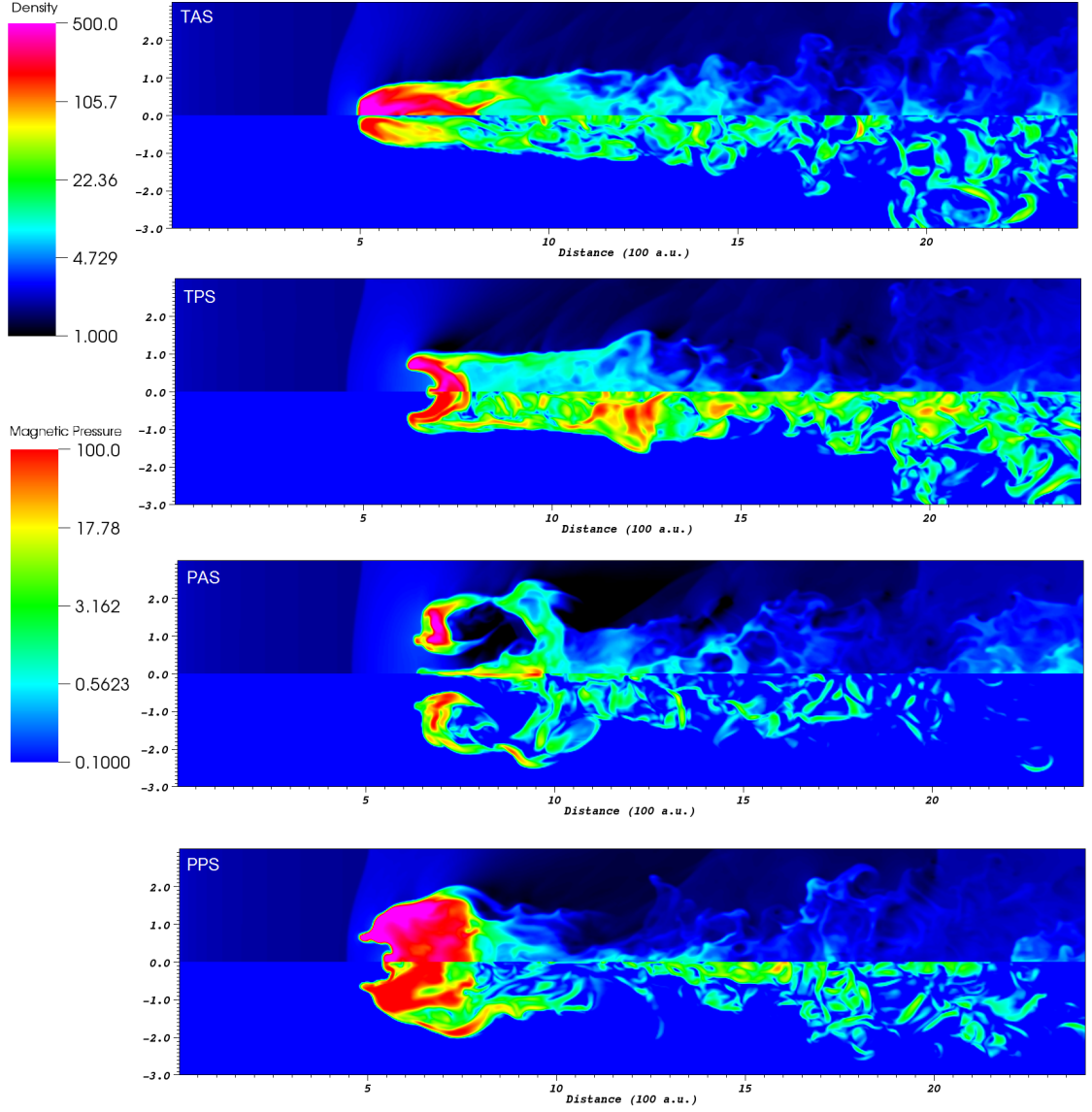


Figure 5.12 Snapshot of shocked clumps cutthrough the center of the domain, at $t = 2\tau_{cc}$. The four panels correspond to the TA, TP, PA, PP cases from top to bottom, respectively. The upper half part of each panel shows the clump density, the lower half part shows the magnetic pressure in pseudocolor.

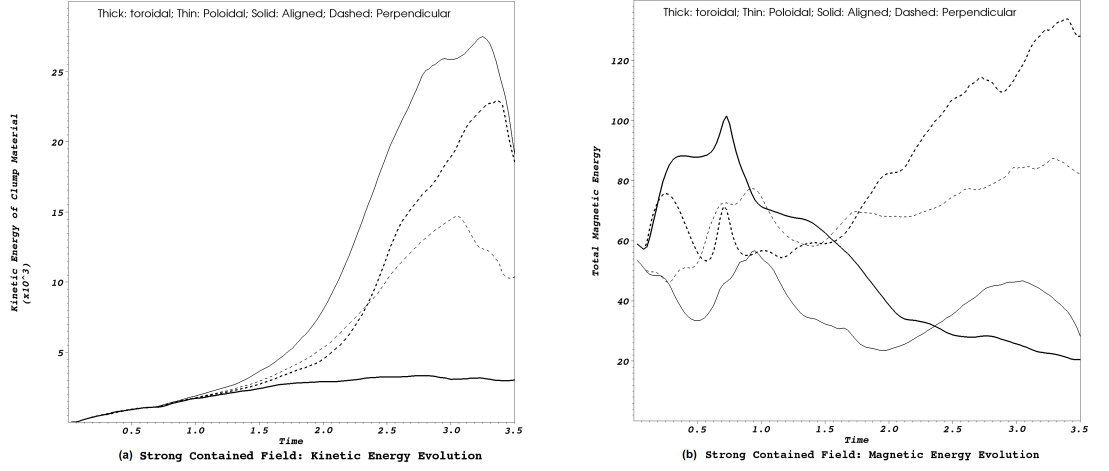


Figure 5.13 Global quantities of the strong self-contained field case: (a) Time evolution of kinetic energy contained in the clump material in computation units, indicating how much energy has transferred from wind into clump. (b) Time evolution of total magnetic energy.

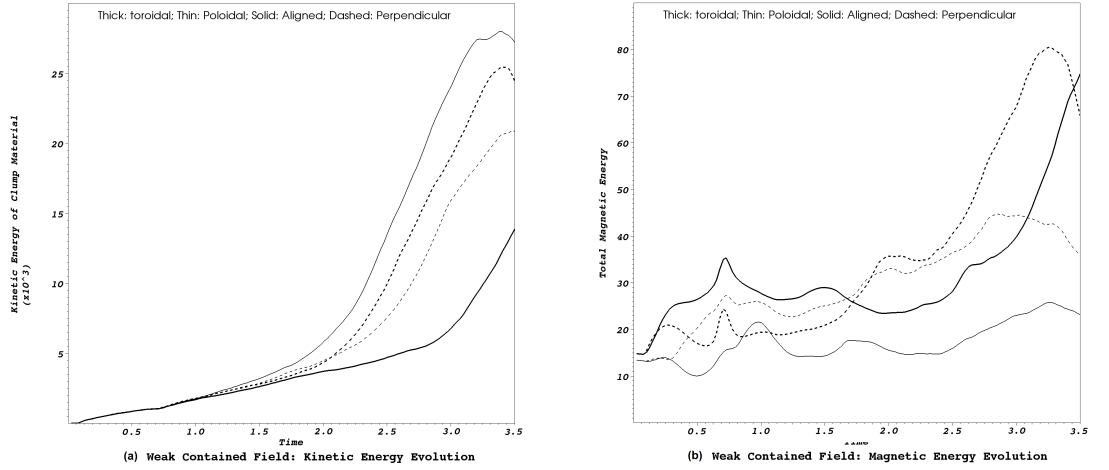


Figure 5.14 Global quantities of the weak self-contained field case: (a) Time evolution of kinetic energy contained in the clump material in computation units, indicating how much energy has transferred from wind into clump. (b) Time evolution of total magnetic energy.

analogous plots for the weak field cases.

In figure 5.13(a), we observe that prior to τ_{cc} , the kinetic energy of the clump gained from the incoming shock is similar in all cases. Later, the curves begin to diverge, reach a peak and then descend. The descending feature after $3\tau_{cc}$ is caused by clump material leaving the simulation box. The identical ascending prior to τ_{cc} and the later diverging behavior for different field configurations will be explained in the subsequent subsection. Similar trend can also be observed for the weak contained field cases of figure 5.14(a).

In figure 5.13(b), we observe that the total magnetic energy evolution for the four field configurations are different: TAS case grows and has the highest magnetic energy at τ_{cc} , PAS case fluctuates and has the lowest magnetic energy τ_{cc} . After τ_{cc} , the TAS curve begins to drop while the other two perpendicular cases continue to rise. At the end of $3\tau_{cc}$, the TPS case has the most magnetic energy, followed by PPS, then PAS. The TAS case dropped to the lowest. In figure 5.14(b), the order of contained magnetic energy prior to τ_{cc} is the same as in figure 5.13(a). However, the TAS curve does not drop afterwards: it continues to rise and at the end of $3\tau_{cc}$, it ranked second in terms of total magnetic energy behind the TPS case. The rest cases have similar feature compared to their strong field counterparts. The magnetic field energy evolution is clearly related to the internal field configuration.

In summary, the kinetic energy transfer and the total magnetic field variation can be determined by the initial structure of the self-contained magnetic field. To account for the results exemplified in the figures, we propose that the shock-clump interaction incurs two phases, a compression phase and an expansion phase.

5.4.1 Modeling the Compression Phase

In the evolutionary phase of the shock-clump interaction the transmitted shock passes through the clump and drives it higher densities. After this compression phase energy is then stored in the form of clump thermal pressure and increased magnetic field pressure. During this phase, the kinetic energy of the clump resides mostly in the form of linear bulk motion and because of the incoming shock, this initial kinetic

energy transfer to the clump is similar for all of the clump cases we have considered. The magnetic energy growth depends on the initial magnetic field geometry because the shock compression only directly amplifies the field components perpendicular to the shock normal.

We now develop a mathematical model that describes the magnetic field energy for the compression phase. We define l_{\parallel} and l_{\perp} as the thicknesses of the clump along and perpendicular to the shock normal respectively. We assume that the clumps are initially spherical so initially $l_{\perp,o} = l_x = l_y = l_z = l_{\parallel,o}$ and the shock propagates in the x direction. Subsequently, l_{\parallel} corresponds to the x direction and l_{\perp} refers to the y and z directions, assuming that the compression is isotropic in the $y - z$ plane.

Assuming that magnetic reconnection is slow on the time scales of the compression phase, magnetic flux conservation can be used to estimate the magnetic energy increase from compression. The energy associated with a uniform field in the $x - z$ plane increases $\propto (l_{\parallel}l_{\perp})^{-2}$ whereas the energy of a uniform field in the x direction will increase $\propto l_{\perp}^{-4}$. Then, assuming that the initial field configuration has $\eta B_0^2/8\pi$ stored in the perpendicular component, $(1 - \eta)B_0^2/8\pi$ stored in the parallel component, we obtain the magnetic energy density after compression:

$$\epsilon_B = \frac{B^2}{8\pi} = \frac{1}{8\pi}[\eta B_0^2(2r_c/l_{\perp})^2(2r_c/l_{\parallel})^2 + (1 - \eta)B_0^2(2r_c/l_{\perp})^4], \quad (5.20)$$

where r_c is the initial clump radius. We use $l_{\parallel,h}$ and $l_{\perp,h}$ to denote the length on the two directions for the case where the clump does not contain any magnetic field, i.e. hydrodynamic case. The magnetic energy density can then be rewritten as:

$$\epsilon_B = (1/8\pi)(\eta B_0^2(2r_c/l_{\parallel,h})^4(l_{\parallel,h}/l_{\parallel})^4(l_{\parallel}/l_{\perp})^2 + (1 - \eta)B_0^2(2r_c/l_{\parallel,h})^4(l_{\parallel,h}/l_{\parallel})^4(l_{\parallel}/l_{\perp})^4). \quad (5.21)$$

Assuming that the post compression clump are self-similar (i.e., different in size, but with the same shape) then the ratio of perpendicular and parallel scale lengths is a constant during compression. This allows us to define a constant shape factor e , given by

$$e = (l_{\parallel}/l_{\perp})^2 = (l_{\parallel,h}/l_{\perp,h})^2. \quad (5.22)$$

To articulate the influence of the magnetic field compared to a purely hydrodynamic clump we assume that the ratio of the magnetized to unmagnetized clump

dimensions in a given direction after compression is inversely proportional to the ratio of forces incurred by hydro and magnetized clumps respectively. That is:

$$l_{||,h}/l_{||} = \frac{F - f_B}{F} = 1 - f_B/F, \quad (5.23)$$

where F is the force exerted by the transmitted shock, and f_B is the "repelling" force exerted by the self-contained magnetic field (see appendix B). The ratio of these two forces is proportional to the magnetic and kinetic energy densities, that is

$$f_B/F = \frac{\alpha B_0^2}{6\pi\rho_s v_s^2}, \quad (5.24)$$

where α is a dimensionless number that depends on the magnetic field configuration, and ρ_s and v_s are the density and velocity behind the transmitted shock. For example, if the repelling force is from the magnetic pressure gradient ∇P_B only, and the magnetic field is distributed in a thin shell of radius $r_c/3$, then

$$f_B = \frac{3}{r_c} \frac{B_0^2}{8\pi} \quad (5.25)$$

per unit volume. On the other hand, the ram pressure acting on the clump has:

$$F = \frac{\rho_s v_s^2 \pi r_c^2}{4\pi r_c^3/3} \quad (5.26)$$

per unit volume. Therefore from the above two expressions we obtain that in the case considered, $\alpha = 3$.

Because the self-contained magnetic field is curved with a positive radius of curvature, a magnetic tension force in $\mathbf{J} \times \mathbf{B}$ is present and can cancel some of the repelling force from the field pressure gradient. For instance, in the toroidal perpendicular case, the tension force along the x direction is $\partial_x B^2/4\pi$. The tension force therefore reduces α to $\alpha = 1$. We define μ as the ratio of the initial averaged clump magnetic energy density and the external energy density driving the shock. We also assume $\mu \ll 1$ during the compression phase. Specifically,

$$\mu \equiv \frac{B_0^2}{6\pi\rho_s v_s^2} = \frac{2}{3\sigma_B} \ll 1. \quad (5.27)$$

We also define the hydrodynamic compression ratio

$$C_h = (2r_c/l_{||,h})^4. \quad (5.28)$$

Combining equations 5.21, 5.23 and 5.28, the magnetic energy density after compression can then be written as

$$\epsilon_B = (B_0^2 C_h e / 8\pi)(\eta + (1 - \eta)e)(1 - \alpha\mu)^4. \quad (5.29)$$

Multiplying this total magnetic energy by the volume of the compressed clump gives the total magnetic energy,

$$E_B = (B_0^2 C_h / 8\pi)(\eta + (1 - \eta)e^2)(1 - \alpha\mu)^4 \pi l_{||}^2 l_{\perp} = (B_0^2 C_h l_{||,h}^3 / 8)(\eta + (1 - \eta)e^2)(1 - \alpha\mu)^4 (l_{||} / l_{||,h})^3. \quad (5.30)$$

Assuming that all of the different clump field configuration cases evolve to similar shapes after compression (i.e. that e is constant) we then have

$$E_B = e E_{h0}(\eta + (1 - \eta)e)(1 - \alpha\mu) = E_h(\eta + (1 - \eta)e)(1 - \alpha\mu), \quad (5.31)$$

where $E_{h0} = B_0^2 C_h l_{||,h}^3 / 8e$ is the total magnetic field energy in the absence of any repelling tension force from the self-contained field, and $E_h = e E_{h0}$. Different initial field configurations lead to different strengths of the repelling force and field amplification during the compression and therefore modifying both α and η . Using the strong field case as example, the η parameter for the TA, TP, PA, PP cases are 1, 0.5, 0.25 and 0.75 respectively. From the field gradient and the magnetic tension, we can use α for these four cases: 3, 1, 1 and 3 (See Appendix B). Using $\mu \approx 0.02$ (from Section 2, $\sigma_B \approx 33$) and $e \approx 0.25$ (from the approximated ratio $l_{||} / l_{\perp} \approx 0.5$), we find the total magnetic energy for the TA, TP, PA, PP to be: $0.94E_h$, $0.61E_h$, $0.43E_h$ and $0.76E_h$, respectively. Therefore at the end of the compression phase, the total magnetic energy from high to low is: TA, PP, TP, PA. These theoretically predicted ordering exactly agrees with the line plots of figure 5.13(b) from the simulations.

The simulations also justify the underlying assumption of equation 5.23, namely that the energy transferred from the shock to the clump material is initially similar in all cases regardless of the initial field configurations because the field is weak with respect to the impinging flow. This is expressed as

$$(F - f_B)l_{||} \simeq F l_{||,h} \quad (5.32)$$

and is evidenced by the kinetic energy transfer plots figure 5.13(a) and figure 5.14(a): During the compression phase, all clumps receive identical kinetic energy flux. Note that our model in the main text ignores differences in e . In the Appendix C we derived the corrections to equation 5.31 when differences in e are allowed.

5.4.2 Expansion Phase

Unlike the compression phase, in the expansion phase a large fraction of the kinetic energy of the clump comes from expansion motion parallel to the shock plane. However the specific evolution of this phase depends on which two distinct circumstances arise at the end of the compression phase: Either (1) the magnetic pressure gradient and tension force are small compared to the pressure force exerted by the shock or (2) the magnetic pressure gradient and tension force dominate over the shock.

If the shock is still dominant at the end of the compression phase (circumstance 1), the clump will expand similarly to the hydrodynamic case. During this phase, the magnetic field inside the clump acts against this expansion: the clump material is doing work to the self-contained magnetic field (mainly via field stretching) in order to expand. Thus, in general, more magnetic energy at the end of the compression phase means a stronger force opposing the expansion. The kinetic energy in the expansion phase shows differences for the different field configurations: the higher the self-contained field energy at the end of the compression phase, the lower the kinetic energy transfer efficiency in the expansion phase. The ordering of kinetic energy transfer efficiency in the expansion phase from high to low is then PA, TP, PP, TA. This again exactly agrees with our plots figure 5.13(a) and figure 5.14(a).

In addition for circumstance (1), the expansion phase also sees a switch in the nature of field amplification: the field is amplified according to how much kinetic energy is transferred into the expansion motion. Thus the ordering of the magnetic field amplification in the expansion phase will be the same as the ordering for the kinetic energy transfer in that phase. In figure 5.14(b), the weak field cases follow this pattern: the TAW, TPW and PPW curves reverse their ordering when entering the expansion phase, giving them the same ordering as the kinetic energy transfer

plot figure 5.14(a). The PAW case does not conform with the prediction of the model because most of the field lines are parallel to the shock propagation direction so that they do not get amplified by the stretching from the expansion motion on the $y - z$ plane.

If the shock is no longer dominant at the end of the compression phase (circumstance 2 above), then the clump evolves under the influence of a significant Lorentz force. The comparison between the TAS (Figure 5.13(b)) and TAW (Figure 5.14(b)) cases exhibits the transition and the distinction between circumstance (1) vs. circumstance (2) evolution: at the end of the compression phase, the TAW case expands while the TAS case shrinks.

The requirement for these distinct evolutions to arise can be predicted using a dimensionless ratio calculated from the parameters of the initial field configuration. Assuming that the pressure from the expansion in the direction perpendicular to the toroidal field lines in a TA case is $1/3$ of the total post shock ram pressure, the ratio between the total magnetic pressure and the pressure of the expansion motion is given by

$$r_e = \frac{(B_0^2 C_h e / 8\pi)(\eta + (1 - \eta)e)(1 - \alpha\mu)^4}{\rho_s v_s^2 / 3}. \quad (5.33)$$

Using the parameters $\alpha = 3$, $\mu_{strong} = 0.02$, $\mu_{weak} = 0.005$, and a compression ratio $C_h = (2R/l_{||,h})^4 \approx 3.5^4 \approx 150$ we find that $r_e \approx 1.3$ for the TAS (circumstance 2) case and $r_e \approx 0.4$ for the TAW case (circumstance 1) respectively. Intuitively the threshold for the toroidal configuration to expand would require $r_e \leq 1$. Thus in the TAS case, the field pinch is dominant at the end of compression phase and the clump collapses down to the axis; whereas in the TAW case the expansion is dominant and the clump behaves similar to a hydrodynamic case.

5.4.3 Geometrical Factor of Magnetic Repelling Force α

Above, we have worked out the magnetic repelling force for the TA case:

$$f_B = \frac{3}{r_c} \frac{B_0^2}{8\pi} \quad (5.34)$$

which gives the parameter $\alpha = 3$. For the TP case, the magnetic tension force is pointing inward with:

$$f_T = \frac{1}{r_c} \frac{B_0^2}{4\pi} \quad (5.35)$$

assuming the radius of curvature for the magnetic field lines is R . This tension force cancels some of the gradient force, which brings α to 1.

For the PA case, the repelling force from the field gradient remains the same (this is because the average self-contained field pressure is an invariant for the four "strong field" cases). But the curved magnetic field on the outer edge of the clump has an average energy of $B_0^2/2$. The tension force is thus:

$$f_T = \frac{1}{r_c/2} \frac{B_0^2/2}{4\pi} \quad (5.36)$$

where the field loop's radius of curvature is $r_c/2$. This tension force also brings α down to $\alpha = 1$.

For the PPS case, the tension force from the outer edge of the clump can be canceled by the tension force from the center of the clump so that their net contribution to the total repelling force is zero. Therefore we get roughly the same α as in the TA case.

5.4.4 Correction in the Shape Factor e

In deriving equation ??, we used an assumption that no matter what the self-contained field configuration is, the clump is always compressed to a self similar shape if the hydrodynamic setup is unchanged. However, we know that when the self-contained field is ordered, the force it exerts on the clump is inhomogeneous depending on the geometry. The difference in the repelling force therefore results in a difference in the shape factor e introduced in Section 5.1. We now look at how large this correction is for the four studied simulations.

Let us go back to equation ??. Assuming the force exerted by the shock on the clump is different on the perpendicular and parallel directions: the force on the perpendicular direction is only a portion of that on the parallel direction, and this

portion is fixed for all the cases with the same hydrodynamic setup:

$$F_y = \gamma F_x \quad (5.37)$$

where γ is fixed. Then following the same procedure as in Section 5.1, we have:

$$\epsilon_B = E_h(\eta(1 - \alpha_x\mu) + (1 - \eta)\frac{(1 - \alpha_y\mu/\gamma)^2}{1 - \alpha_x\mu}) \quad (5.38)$$

where α_x and α_y denote different repelling forces from the self-contained field on the x and y direction.

As in Section 5.1, α_x for the simulated cases TAS, TPS, PAS, PPS are 3, 1, 1 and 3. Since the perpendicular α_x is just the aligned α_y and vice versa, we know that the α_y for these four cases are 1, 3, 3 and 1. We use the same parameters as in Section 5.1: $\mu = 0.02$. We assume the incoming shock engulf a spherical sector of the clump with a cone angle $2\theta_e$. Then the compression force applied on the y direction is a fraction of that of the initial incoming shock. This fraction is $\frac{2}{\pi} \int_0^{\theta_e} \frac{1}{2} \sin^2 2\theta d\theta$. During the compression process, θ_e varies from 0 to $\pi/2$. Therefore we can estimate γ as:

$$\gamma = \frac{2}{\pi/2} \int_0^{\pi/2} \frac{\int_0^{\theta_e} \frac{1}{2} \sin^2 2\theta d\theta}{\pi/2} d\theta_e = 0.125 \quad (5.39)$$

where the inner integration calculates the ratio of average pressure applied on the perpendicular direction when the compressed part of the clump is a spherical cone with cone angle θ_e ; the outer integration calculates the average over the compression process where θ_e varies from 0 to $\pi/2$. The factor 2 results from the fact that the perpendicular compression happens on both $+y$ and $-y$ directions.

We can calculate the corrected compressed magnetic field energy for the TAS, TPS, PAS and PPS cases. The results are $0.94E_h$, $0.63E_h$, $0.44E_h$ and $0.72E_h$, for the TAS, TPS, PAS, PPS cases respectively. Comparing to the results presented in Section 5.1: $0.94E_h$, $0.61E_h$, $0.45E_h$ and $0.89E_h$ for the four cases, we find there is a positive correction to the cases with $\eta < 1$. The ordering of the field amplification factor remains unchanged. Further sophisticated modeling is possible by taking into consideration the dependence of the Lorentz force on the compression ratio: the further the compression, the smaller the magnetic field length scale thus the stronger

the repelling force. This results in a model with an integral equation, on which we did not discuss in this paper.

5.4.5 Mixing of Clump and Ambient Material

Figure 5.15(a), (b) show the mixing ratio of wind and clump material at τ_{cc} and $3\tau_{cc}$ for the strong field cases. Figure 5.16(a), (b) show the mixing ratio of wind and clump material at τ_{cc} and $3\tau_{cc}$ for the weak field cases. We define a wind-clump mixing ratio in a single computational cell as

$$\nu = \frac{2\min(n_c, n_w)}{n_c + n_w}, \quad (5.40)$$

where n_c and n_w denote the clump and wind number densities, respectively. This definition shows that $\nu = 1$ means perfect mixing: there is equal number of clump and wind particles in the cell, while $\nu = 0$ means no mixing at all. In figure 5.15, we see that the mixing ratios for the four strong self-contained field cases are almost identical at early times. This is consistent with the fact that at early times the clump as a whole is in the processes of being accelerated as along the shock propagation direction. The only mixing between clump and wind occurs at the edges of the clump from the interaction with the incoming shock. The strong field prevents strong mixing.

In the weak magnetic field cases, the toroidal configurations do not see a significant increase in the early time mixing ratio compared to the strong field case (Figure 5.16(a)). This is because the toroidal case has most of its magnetic field concentrated at the edges of the clump (See Appendix A). Thus the average plasma β on the outer edge is still small enough to contain the clump material. In the weak poloidal configuration cases however, the magnetic field is concentrated at the center of the clump and accordingly the PAW and PPW cases have the largest magnetic β on the outer edge of clump, making them the most susceptible to early shock erosion. This explains the significant increase we see in the initial mixing ratio in the PAW and PPW cases (Figure 5.16(a)).

The late mixing ratio depends on how much kinetic energy is transferred from wind to clump. At late times the PA configuration has the highest mixing ratio of

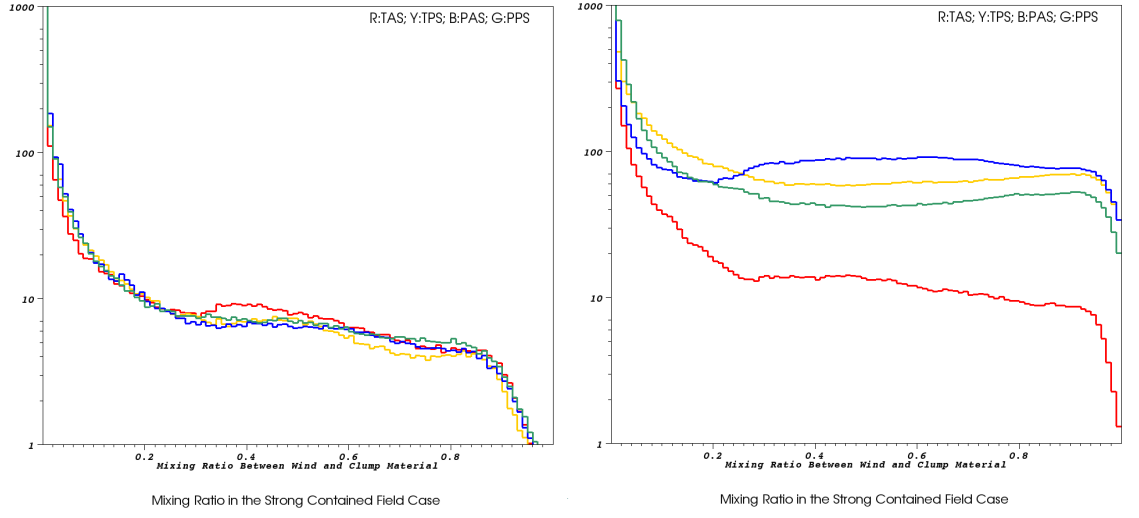


Figure 5.15 Wind-clump mixing ratio for the strong self-contained field case: (a) at τ_{cc} . (b) at $3\tau_{cc}$. The color codings and their corresponding simulations are labeled in the plot

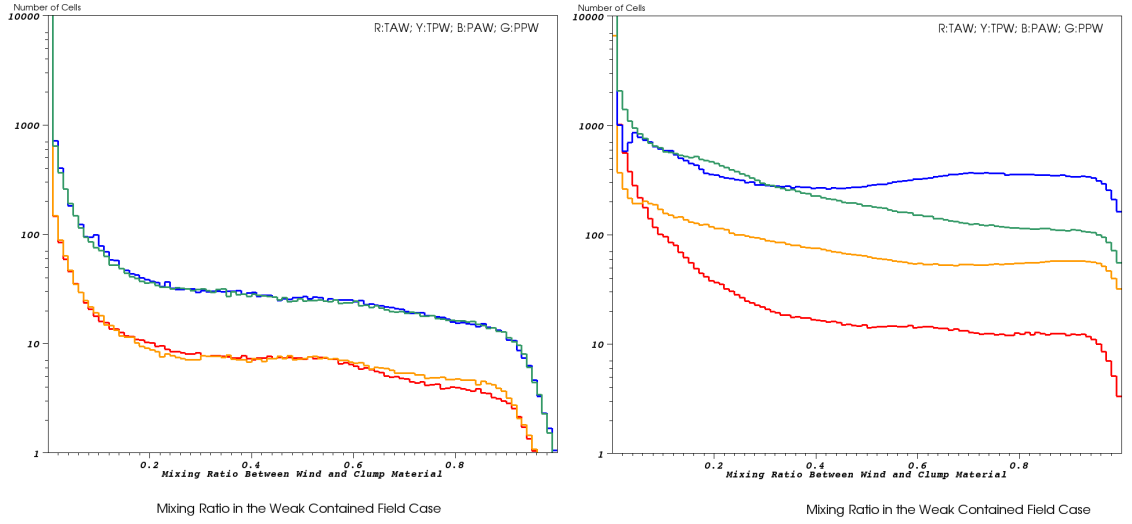


Figure 5.16 Wind-clump mixing ratio for the weak self-contained field case: (a) at τ_{cc} . (b) at $3\tau_{cc}$. The color codings and their corresponding simulations are labeled in the plot

the four studied cases. The PP and TP cases have intermediate mixing ratios, and the TA has the lowest mixing ratio. This ordering agrees with the ordering of kinetic energy transfer: the more force resisting compression from the self-contained magnetic field in the early phase the less the kinetic energy transfer occurs in the expansion phase, and the less the mixing. The late mixing ratio also partially depends on the efficacy of enhanced turbulent mixing downstream. The 3-D images in the previous section Figures 3 to 10, we can identify the downstream turbulence of the TA and PA cases as the least and most volume filling respectively.

5.5 Concluding Remarks

Using 3-D AstroBEAR MHD simulations, we have demonstrated that shocked clumps with self-contained internal magnetic fields show a rich, but qualitatively understandable behavior not seen in previous simulations of shock-clump interactions which employed ordered background fields extending through both the clump and the ambient gas.

We find that the post-shock evolution depends strongly on internal field morphology. The energy transfer from wind to magnetic field and the mixing of wind and clump material also depend on the field geometry. In general, the more perpendicular the clump magnetic field is to the direction of shock propagation, the more aerodynamic resistance the field provides, and the less the mixing and energy transfer occurs. Compared to the uniform field cases studied in Jones et al 1996, both provide protection against shock erosion and mixing when the magnetic field is oriented perpendicular to the shock normal. However, the uniform field case relies on the stretching amplification of the magnetic field along the clump profile thus acting as a “shock absorber”, the contained field case relies on the internal field tension to hold the clump material together against expansion.

We have studied the mathematical model of the evolution by dividing the process into “compression” and “expansion” phases. Since the compressed magnetic field can greatly influence the morphology during the expansion, we estimate the amplification by deriving equation 5.31. The qualitative behavior of different cases studied in the

simulation provides good agreement with our model.

The extent to which clump material mixes with the wind material also depends primarily on the field orientation: in general, the more the initial field is aligned perpendicular to the shock normal, the better the clump can deflect the flow around the clump and the less effective the mixing. Equivalently, the better aligned the field is with the shock normal, the more effective the clump material gets penetrated by the incoming supersonic flow, gains kinetic energy in expansion, and enhances mixing.

Chapter 6

Triggered Star Formation

6.1 Introduction

Triggered star formation (TSF) occurs when supersonic flows generated by distant supernova blast waves or stellar winds (wind blown bubbles) sweep over a stable cloud. In realistic environments, this is likely to occur when such a flow impinges the heterogeneous regions within molecular clouds (Roberts (1969), Hillenbrand (1997), Kothes et al (2001), Bonnell et al (2006), Leao et al (2009)). While it is unclear if TSF accounts for a large fraction of the star formation rate within the galaxy, the concept has played an important role in discussions of the formation of our own solar system because it offers a natural way of injecting short lived radioactive isotopes (SLRI's) like ^{26}Al and ^{60}Fe into material which will then form planetary bodies.

In light of SLRI observations, a series of studies dating back to the 1970s (Cameron et al (1977), Reynolds et al (1979), Clayton et al (1993)) have attempted to quantify the ability of a blast wave or stellar wind to both trigger collapse in a stable cloud and inject processed material. Because of the complex nature of the resultant flows, these studies have relied strongly on numerical simulations (Boss (1995), Foster et al (1996), Vanhala et al (1998), Vanhala et al (2002)). In a more recent series of papers by Boss and collaborators (Boss et al (2008), Boss et al (2010), Boss et al (2013)) the shock conditions needed for successful triggering and mixing were mapped out. In general, the higher the Mach number of the shock, the more difficult it is to

trigger collapse. Faster shocks can shred and disperse the clump material before it has time to collapse. However faster shocks also allow better mixing by enhancing Rayleigh-Taylor instability growth rates. Boss et al (2010) have shown that for a stable cloud of $1M_{\odot}$ and radius of 0.058 pc, the incoming shock needs to be slower than 80 km/s to trigger collapse. The shocks also need to be at least 30 km/s to yield 10% of blast material (by mass) mixing into the cloud. Thus there is a relatively narrow window, in terms of shock Mach number, where both triggering and mixing can be achieved.

Boss et al (2010) and Boss et al (2013) further pointed out that in order to explain the abundance of ^{26}Al in the Solar System using triggering, the supernova shock needs to satisfy additional width requirements besides the shock speed condition. Finally, Gritschneider et al (2012) pointed out the importance of cooling in such a triggering scenario, detailing the condition for collapse of the cloud fragments by thermal instability. We note also Dhanoa et al (2014) who studied the possibility of forming low-metallicity stars by supernova shock triggering with simulations and Vaidya et al (2013) who studied the collapse of magnetically sub-critical cloud cores.

These studies have done much to reveal the details of TSF but they have been restricted to the early stages of the resulting flow pattern. The full evolution leading to a collapsed object (a star) and its subsequent gravitational interaction with the surrounding gas has yet to be studied. Part of the difficulty has been the numerical challenge of generating a sub-grid model for the collapsing region that adequately represent stars. This has left many questions unanswered. For instance, what is the mass accretion rate of such a star formed by triggering? What is the accretion history of such a star? Does a trigger-formed star also have a disk when rotation is present in the cloud? If so, is the disk stable? Some of these questions, such as disk stability, have been studied in other contexts: Ouellette et al (2007) explored disk ablation when the disk was swept over by a supernova blast wave and ejecta. They found the disks to be long-lived and relatively stable in spite of the supernova blast impact. Their disks were not, however, formed by triggering but were considered to be pre-existing. Determining the surviving disk mass and the mixing between cloud and wind material is important for understanding the role of TSF in Solar System

formation and/or in supplying SLRI abundances.

We note that the issue of triggering is of more general interest than discussions of SLRIs. For example the in the HII regions associated with the Carina nebulae a number of elongated pillars are seen with jets emerging from the head of the pillar (HH901 and HH 902 Smith et al. (2010)). The presence of the jet is an clear indication of the presence of a newly formed star at the head of pillar. If the pillars are formed via a combination of photo-ablation and winds from the massive star then one would expect shock triggering to occur within any marginally stable clumps in the pillar material once the shock reached the clump position. Thus the dynamics of star formation within HII region pillars represents another of many reasons why TSF needs to be explored in its full evolutionary detail.

In this paper, we use the parallel AMR code AstroBEAR2.0 (Cunningham et al (2009), Carroll-Nellenback et al (2013)) to study the shock-induced triggering of a stable Bonnor-Ebert cloud following, for the first time, the long-term evolution of the system after a star, numerically represented by a sink particle, has been formed.

To explore the post-triggering physics of TSF, we present simulations in three different regimes: I. triggering a non-rotating cloud; II. triggering a cloud with an initial angular momentum parallel to the shock normal; III triggering a cloud with an initial angular momentum perpendicular to the shock normal. These simulations allow us to answer four questions: 1. What is the nature of the flow pattern after a star has formed in TSF? 2. How do disks form in TSF environments? 3. what is the subsequent disk evolution in the presence of the post-shock flow? 4. How do accretion and mixing properties change with initial conditions in TSF? In particular we explore the evolution and the disruption of the protostellar envelope by the post-shock flow. For the rotating cases, we are interested in how the initial angular momentum can lead to formation accretion disk surrounding the newly formed star. Finally, we study the interaction of the disk and the post-shock flow and its affect on circumstellar disk survival.

The structure of this first report of our ongoing campaign of simulations is as follows. In Section 2 and 3 we describe the numerical method and model. In Section 4 we report our results. Section 5 provides analysis of the results and we conclude in

Section 6.

6.2 Initial Simulation Setup

We begin with an initial marginally stable Bonnor-Ebert sphere as the triggering target for our shock. The initial cloud setup is similar to Boss et al (2010), i.e a cloud with $M_c = 1M_\odot$, a radius of $R_c = 0.058pc$, a central density of $\rho_c = 6.3 \times 10^{-19}g/cc$ and edge density of $3.6 \times 10^{-20}g/cc$. The cloud has a uniform interior temperature of $10K$. The ambient medium is initialized to satisfy pressure balance at the cloud boundary when the cloud is stationary, with density $\rho_a = 3.6 \times 10^{-22}g/cc$ and temperature of $1000K$.

We express time scales in terms of the “cloud crushing time” t_{cc} which is defined as the time for the transmitted shock to pass across the cloud, i.e. $t_{cc} = \sqrt{\chi}R_c/V_s$ where V_s is the incident shock velocity and $\chi \approx 1700$ is the ratio of peak cloud density to ambient density. For our conditions $t_{cc} \approx 276$ kyrs. We have performed simulations to check the stability of the cloud and find that the cloud oscillates with a time scale of about $10t_{cc}$. This is longer than the time span of our simulation. The free-fall time t_{ff} can be used to gauge the time scale of gravitational collapse. Our initial cloud has $t_{ff} \approx 84$ kyrs. Note that although we find that triggering can form a star as early as $t_{cc} < t < 2t_{cc}$, our interest in the post-triggering interaction leads us to simulate the fluid evolution through $4t_{cc}$, which is approximately equivalent to 1 million years. To make a comparison between slow and fast shock cases, we initialize the incoming shock at two different Mach numbers: either $M = 1.5$ or $M = 3.16$, where M is the ratio between the shock speed and ambient sound speed: $M = v_s/c_s$. Given the shock speed $v_s = 3km/s$, we can estimate the incoming mass flux as $F_s = 4\pi\rho_av_s \approx 1.4 \times 10^{-13}g/cm^2s$.

We use $K = \Omega t_{ff}$ to characterize the importance of rotational energy in our simulations where Ω is the angular velocity. We assume $K = 0.1$ for all the rotational cases presented in this paper (Banerjee et al (2004)). Characterizing the influence of different $K > 0$ values is an important separate topic that we leave for future work. Here we simply focus on studying the difference between the rotating ($K = 0.1$)

Table 6.1 Simulation Setups

Code	Shock Mach	Cloud Rotation (relative to shock normal)	K
N	1.5	None	0.0
N'	3.16	None	0.0
R1	1.5	Parallel	0.1
R2	1.5	Perpendicular	0.1

and non-rotating cases ($K = 0$) and different orientations of the initial rotation axis. Adding an initial solid-body rotation can change the initial equilibrium of the cloud as the added centrifugal force breaks the equilibrium of a Bonnor-Ebert sphere. However, we have performed simulations to verify that only for $K > 0.4$ can significant expansion be seen during the time duration of our simulations, i.e. 4 cloud crushing times. Furthermore, the added slow expansion from $K = 0.1$ does not alter the mechanism of shock triggering as such effect does not lead to cloud collapse on its own. Intuitively, rotation does not only lead to possible disk formation, but also adds resistance to triggering from centrifugal force. The effect of rotation on triggering is discussed in more detail in Section 5. The parameters of the initial setup are summarized in table 6.1.

We continue to inject a "post-shock wind" of the same form as that used in Boss et al (2010) (and of the same density and temperature as the initial ambient gas) until the end of the simulations (i.e. long after the initial shock has passed by the cloud). We assess how strongly this wind ablates the bound cloud material, including that material which forms a disk in the rotational cases. The density of this post-shock wind is approximately 100 times lighter compared to the shock front, giving a mass flux of $F_w \approx 1.4 \times 10^{-15} g/cm^2 s$.

Although continuation of this post-shock wind for the full duration of the simulation is unphysical because it implies a total mass loss of $198M_\odot$ ejected from a source 1pc away, it will tell us that any disk which survives this extended wind will also survive any shorter lived wind with the same mass flux .

We implement mesh refinement to focus on the region centered on the sink particle. The simulation box has a base resolution of $320 \times 192 \times 192$, which is equivalent

to 64 cells per cloud radius. We add 3 levels of refinement around the region of the cloud (or sink particle) yielding an effective resolution of $64 \times 2^3 = 512$ cells per cloud radius. We employ outflow boundary condition at all the boundaries of the simulation box.

6.3 Simulation Results

In general, we can divide the triggering event into three phases: I. the incoming shock impinges on the cloud compressing it into a dense core until the local Jeans' stability criterion is violated. The subsequent infall generates a star (represented by a sink particle in our simulations) marking the end of this phase. II. Ablated cloud material that is not gravitationally bound is accelerated and ejected downstream. The still gravitationally bound gas is also exposed to the post-shock wind. III. The star and its bound material continue to evolve while interacting with the post-shock wind until the end of the simulation.

Fig.1 demonstrates these stages. In the figure we show the column density (density integrated along the axis pointing out of the plane) evolution of case R1 (see table 6.1) immediately after the star is formed, at about $1.1t_{cc}$ (0.3 million years) in the top panel; immediately after the star has entered the post-shock region (0.5 million years) in the middle panel; and after the star and its surrounding disk become embedded completely in the post-shock wind in the bottom panel. In Fig.1(a), a star (represented by a red sphere) embedded in the cloud is visible as the collapse proceeds. In Fig.1(b), the star, as well as the bound cloud material has been left behind as the unbound remnant cloud material is driven downstream (to the right). The star and the gas bound by its gravitational potential remain exposed in the post-shock wind. At this point, the initial angular momentum of the cloud (oriented along the shock normal) leads to the creation of a disk. In Fig.1(c), we capture the flow pattern at time ~ 0.85 million years. Here, although the disk has experienced a ram-pressure driven ablation from the post-shock flow for more than 0.3 million years, its shape and size remain relatively unchanged. As noted in Section 3, in reality the post-shock

flow will last less than 1 million years, so our results conservatively indicate that disks should survive the post-shock environment of a typical triggering event. This survival is discussed in more detail in Section 5.4.

To compare the different cases listed in table 6.1, in figure 6.2 we plot the column density of each case at a fixed time - 0.6 million years. This corresponds to just after the star has entered the post-shock wind, and the disk, if it forms, is present. For case N, the bound cloud material surrounding the newly formed star is quickly shredded away by the post-shock flow, leaving the star isolated in the wind. Given the low density of the resulting circumstellar material, its accretion rate is low and the bulk of mixing be determined before the end of phase II.

For case N', the incoming shock is approximately twice as fast as that in case N. We observe that star formation can still be triggered, confirming that $Mach = 3.16$ falls in the “triggering window” (less than Mach 20) described in Boss et al (2010). The time scale for the triggering t_t , defined as the time scale between the beginning of the shock compression until the formation of the star, is half of that of case N.

For cases R1 and R2, the bound material forms a disk of radius $\sim 1000\text{AU}$ at the end of phase II. This disk radius is consistent with the estimation of disk formation radius $r_d \approx \Omega^2 R_c^4 / 2GM_s$, where M_s is the mass of the central star (about $1M_\odot$). This expression for r_d is determined by the radius at which material in-falling while conserving angular momentum reaches a Keplerian rotation speed. Note also that the disk temperature deviates from the initial cloud temperature (10K) because γ is set to 1.0001 instead of exactly 1. For Federrath type accretion algorithm, this temperature increase can introduce heated numerical accretion zone (a zone of fixed number of cells that are kept at just below the threshold density) around the star. Once the star drifts into the post-shock wind, this heated zone can expand and disrupt the circumstellar profile. This is the reason why we preferred to choose Krumholz accretion algorithm which does not rely on creating such an accretion zone. We have verified through simulations that when $\gamma - 1$ is approaching zero, the triggered star formation results obtained from Federrath and Krumholz type accretion algorithms

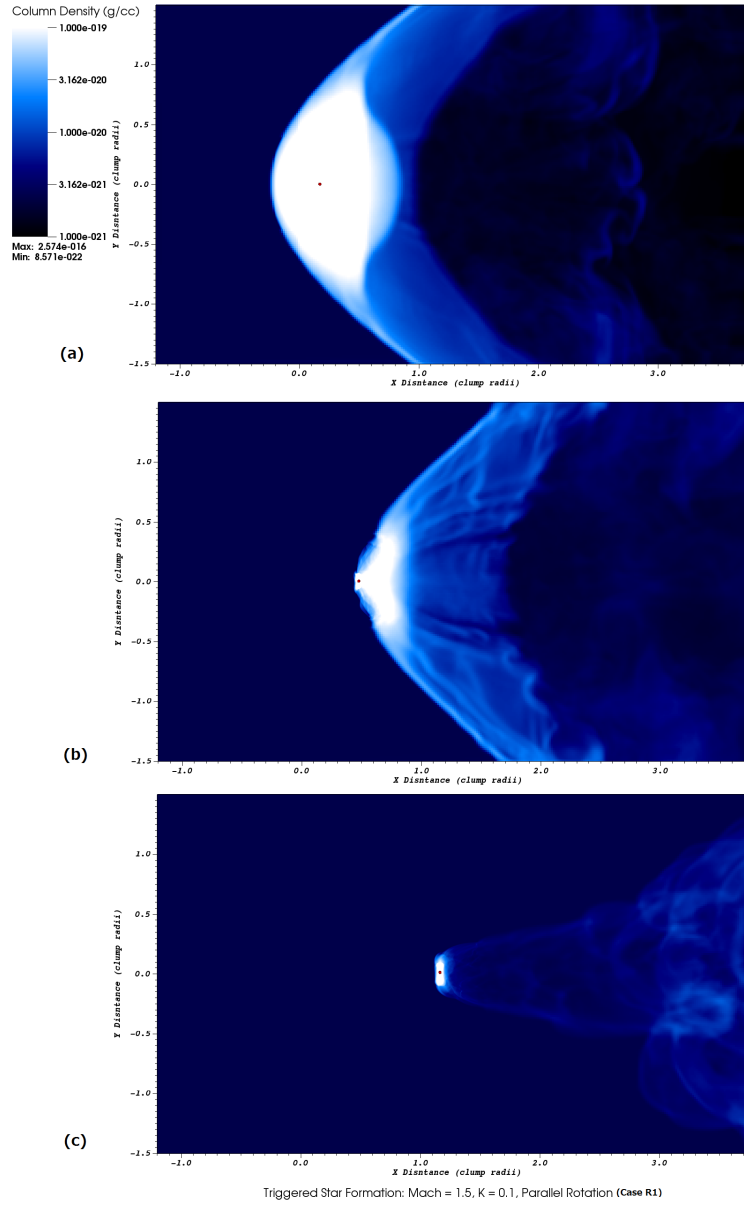


Figure 6.1 Column Density Evolution for Case R1: (a) 0.3 million yrs; (b) 0.5 million yrs; (c) 0.85 million yrs

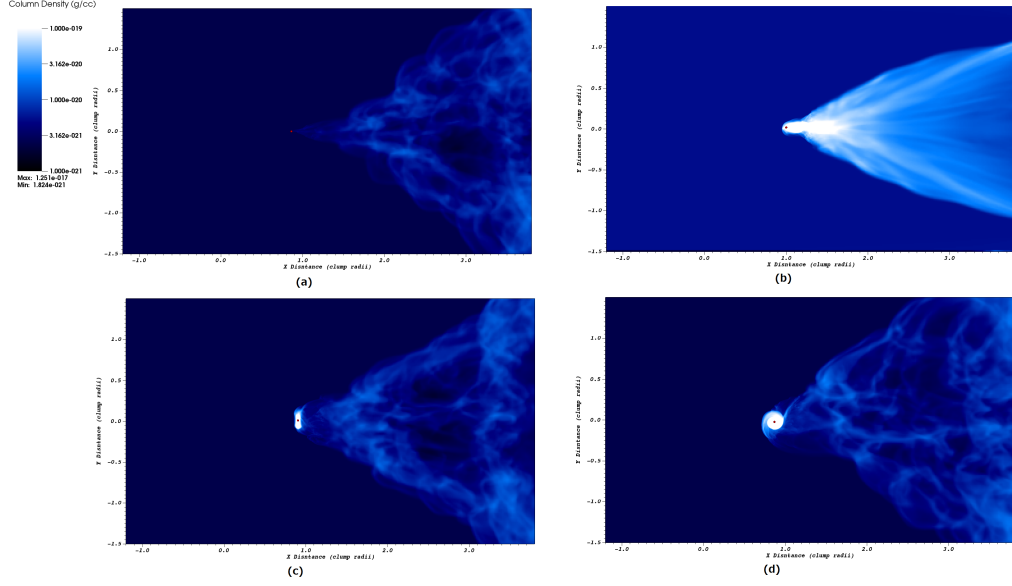


Figure 6.2 Post-triggering evolution at 0.6 million years: (a) Case N; (b) Case N'; (c) Case R1; (d) Case R2.

converge.

The disk formation is a natural consequence of the initial rotation, as in both cases the planar shock does not significantly alter the angular momentum distribution of the cloud as long as the shock remains stable. In the the N cases, little post-shock circumstellar material remains compared to the R cases since the material can more easily collapse to the core for the former cases. However, the total post-shock stellar plus bound circumstellar material is lower for the R cases than the N cases since the presence of angular momentum makes material less tightly bound initially.

We also expect less mixing in the N cases compared to the R cases given the same shock Mach number because an extended disk acts to trap some of the incoming material. But because R1 and R2 have different orientations of the disk relative to the incoming wind, we expect the mixing of material into the disks in these two cases to also be different. In case R1, the disk presents the maximum cross section for ablation (πr_d^2) while in case R2, the wind hits the disk edge on, yielding a much smaller cross section $\propto h$ the vertical scale height. Case R2 exhibits an ellipsoidal

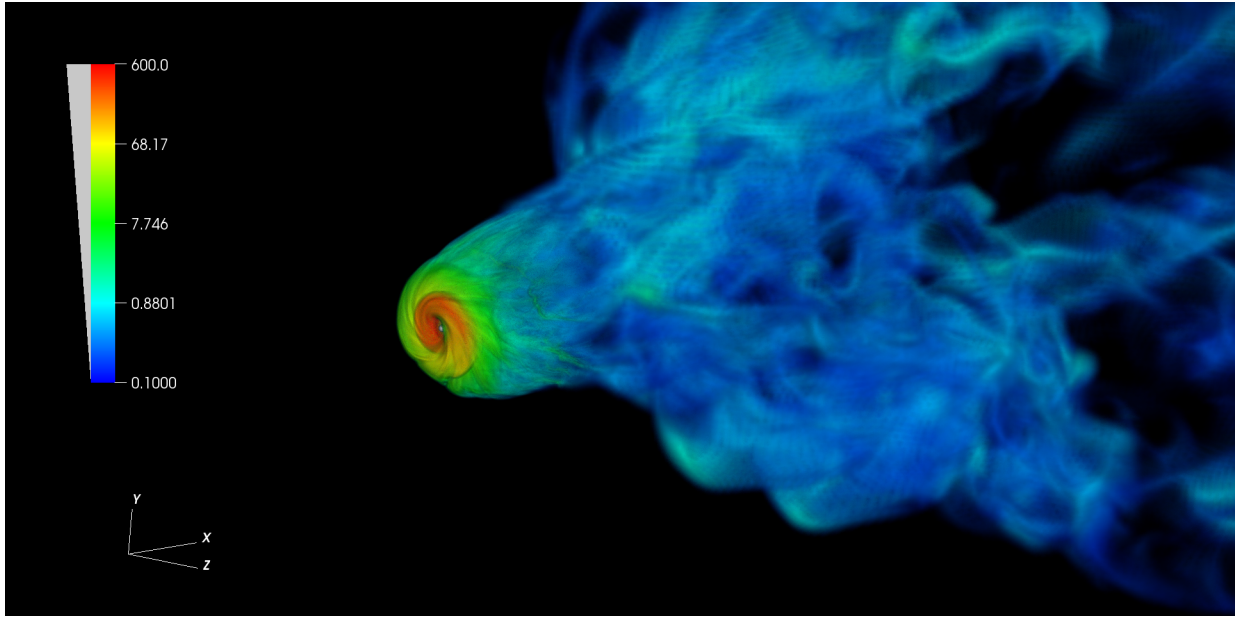


Figure 6.3 Case R1: 3D volume rendering of the disk formed by triggering at 0.6 million years.

disk geometry just after its formation due to the disk-wind interaction. In short, comparing the R and N cases, we can qualitatively understand the differences in both accretion rates and mixing ratios.

In figure 6.3, we plot a 3D volume rendering of case R1, at time 0.6 million years. This corresponds to the time period after the disk has been completely engulfed in the post-shock wind. The pseudo-color shows the density percentage as normalized by the initial average cloud density - initial average cloud density is set as 100. Figure 6.3 shows that the compressed cloud material (red region in figure 6.3) mostly ends up accreted onto the star (marked in figure 6.3 as the white sphere) or in the accretion disk. The figure shows the spiral pattern that forms downstream as disk material is ablated by the post-shock flow.

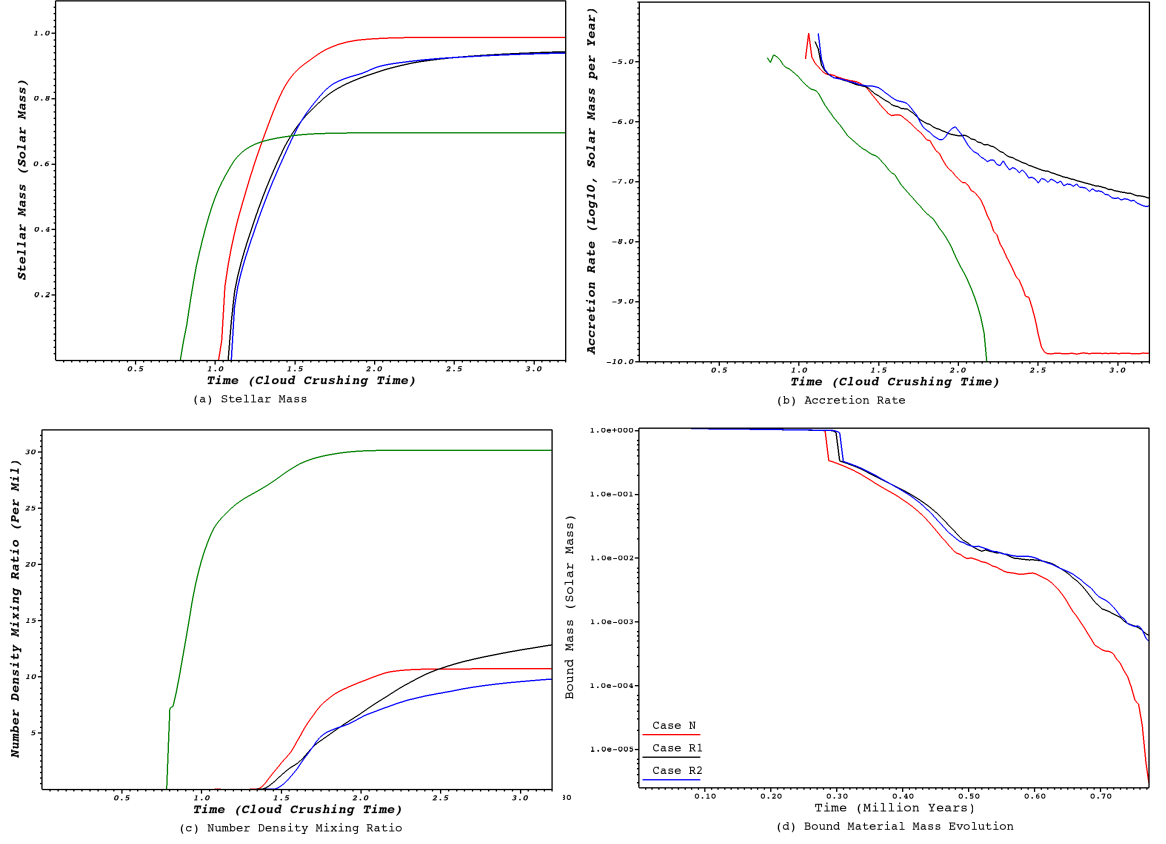


Figure 6.4 Time Evolution of Stellar Mass, Accretion Rate, Wind Material Mixing Ratio and Bound Mass

6.4 Quantitative Discussion

In this section we briefly discuss the implications of our simulations, in terms of the physics of triggering and subsequent star/disk evolution, given the cases we have studied. We saved a more complete exploration of parameter space and its astrophysical implications for future work.

6.4.1 Triggering time

In figure 6.4(a), we plot the evolution of the stellar mass (represented by sink particle mass) formed by the triggering event for the four cases. Note first that in all four simulations the star forms at around 0.8 to $1.2t_{cc}$, which corresponds to about 0.2

to 0.3 million years for the Mach $M = 1.5$ cases, and about 0.12 million years for the $M = 3.16$ case. Case N' has an absolute formation time of about half of that of Case N, due to its fast compression. For the transmitted shock, the density compression ratio η is related to the transmitted shock Mach number M via $\eta \propto M^2$. This is because the force exerted on the cloud is proportional to the ram pressure of the incoming wind $\rho_w v_s^2$, where ρ_w is the wind density defined in Section 3 and v_s is the shock velocity: $v_s = Mc_s$. If we assume that the compressed cloud material behind the transmitted shock undergoes free-fall collapse, we can estimate the collapse time scale as $t_{ff} \propto 1/\sqrt{\eta}$. This yields a scaling for the triggering time described in the last section as $t_t \propto 1/M$. If the triggering time is inversely proportional to force on the cloud, then as we increase the Mach number by a factor of 2 as occurs in the set up of Case N vs. Case N', we expect the triggering time to be approximately halved. This is consistent with figure 6.4(a). The rotating cases R1 and R2 have slightly later triggering times compared to the non-rotating cases, because of the additional support against collapse provided by the added rotation. When K is small, the inward acceleration is reduced by ΩR^2 , where R is the orbital radius of the considered gas parcel. The in-fall time is then calculated from:

$$\frac{1}{2}(GM/R^2 - \Omega^2 R)t_{in} = R \quad (6.1)$$

from relations $GM/R^2 = 2R/t_{ff}^2$ and $\Omega^2 R = RK^2/t_{ff}^2$, we obtain the in-fall time is increased as $t_{in} = \sqrt{1 + K^2}t_{ff}$ when initial rotation is added. The delayed triggering time can then be seen as the effect of the K^2 term.

6.4.2 Asymptotic Stellar Mass

Another significant feature shown in all four cases is the asymptotic stellar mass found in the simulations. We find $M_* \sim 1M_\odot$ for the Mach 1.5 cases, and $0.6M_\odot$ for the Mach 3.16 case. The lower asymptotic mass of case N' can be explained by the fact that once a sink particle is formed, its accretion rate is determined by the Bondi accretion rate implemented through the Krumholz et al (2004) accretion algorithm.

Thus, the stellar mass at the end of phase I, and consequently the asymptotic stellar mass, is predominantly determined by how much time the particle has to accrete cloud material before it enters the post-shock wind region. This time scale is determined by how fast the incoming shock can accelerate the cloud material. Using the analysis of Jones et al (1996) we have the “cloud displacement” time $t_{dis} = \sqrt{R_c/a_c}$, where R_c and a_c are the cloud radius and acceleration, respectively. Since a_c is proportional to the ram pressure from the shock exerted on the cloud, $a_c \propto M^2$. This yields a time scale $t_e \propto \sqrt{R_c}/M$ for the star and its bound material to become exposed to the post-shock. Thus case N’ has about half the time to accrete cloud material as compared to cases N, R1 and R2. Figure 6.4(a) agrees with the above analysis. For the Mach 1.5 cases, the final stellar mass approaches $M_* \sim 0.98M_\odot$ for the non-rotating case, and $M_* \sim 0.94M_\odot$ for the two rotating cases. This indicates that for all the cases studied, most of the initial cloud material ends up in the star before the end of phase II, which is consistent with the discussion in Section 4.

The reduced stellar mass for the rotating cases is reasonable as some of the material ends up in a disk as opposed to directly accreting onto the star. At the end of stage I (0.45 million years for the R cases), the gravitationally bound gas enters the post-shock region, and the disk is visible in the simulations. This disk has an initial mass of approximately $0.1M_\odot$, which is in agreement with the initial K and its radius as discussed in the previous section. The disk mass gradually depletes because of the accretion onto the star as shown in figure 6.4(d), and the stellar mass continues to increase during stage II for the R cases. At the end of the simulation, the disk mass drops to less than $10^{-3}M_\odot$. We will discuss the wind ablation and the asymptotic disk mass in more detail in Section 5.4.

6.4.3 Accretion Rates

In figure 6.4(b), we present the stellar accretion rates in our models. The accretion rate is calculated as the time derivative of the stellar mass. The most conspicuous feature is the difference between the non-rotating and rotating cases. While case N

reaches its final accretion rate at approximately 0.7 million years (set by Bondi-Hoyle accretion in the post-shock flow), cases R1 and R2 continue to accrete mass at a higher rate because the mass was unable to fall in earlier and is in the disks. The higher accretion rate at these times for the R cases can be thought of as “delayed” infall: in the R cases, some of the cloud material ends up in the disk instead of being immediately accreted by the star due to the additional support provided by the rotation. This material can still be accreted through the disk later in stage II (i.e. accretion is delayed). The total mass that becomes the star would be overall less for the R cases.

The disk formation and subsequent accretion aids in mixing more material from the shock (and post-shock) gas into the star compared to previous studies without such disks as the disk provides greater cross section for interaction with the incoming wind. The accretion efficiency of wind material during stage II is set by the cross section of the total bound gas embedded in the wind (star+gas). This cross-section is πr_d^2 for the R cases. For the N cases it is determined by the Bondi radius: πr_B^2 where $r_B = 2GM_*/(c_s^2 + v_w^2)$. Given the parameters $M_* \approx M_\odot$, $T = 10K$ and $v_w = 3km/s$, we find that $r_d^2 \gg r_B^2$.

We define the mixing ratio as the ratio of $\kappa = n_w/(n_c + n_w)$, where n_w and n_c are the number densities of the post-shock gas and cloud gas that end up accreted onto the star, respectively. In figure 6.4(c), we see that the parallel rotation case has the highest mixing ratio amongst the three Mach 1.5 cases. As discussed earlier, this is likely due to its large cross section of interaction with the post-shock flow. Case R2 has a lower mixing ratio compared to N at the end of the simulation but the R2 rate is still growing while the N rate has reached its maximum value. Note that the $M = 3$ case shows much more mixing than the lower Mach number simulations. This is likely the result of increased shock speed on the internal flow within the cloud and is consistent with Boss et al (2008), where the effect of shock Mach number on mixing ratio was more thoroughly explored.

6.4.4 Circumstellar Bound Mass and Disk Survival

Finally in figure 6.4(d), we present the mass evolution of the circumstellar gravitationally bound gas where we label any gas parcel with total energy $E = E_k + E_{th} + E_{gas-gas} + E_{gas-particle} < 0$ as bound (E_k is the kinetic energy, E_{th} is the thermal energy, $E_{gas-gas}$ and $E_{gas-particle}$ are the gravitational binding energy from self gravity and the star's point gravity.) The initial kink in the three curves at around 0.3 million years coincides with the onset of triggering. From 0.3 to 0.5 million years, the shapes of the curves remain similar. This is in phase I where the star has not yet emerged from the cloud, and most of the mass loss results from the accretion onto the star.

Since case N does not form a disk, the circumstellar bound material is quickly shredded away by the incoming wind once exposed to the post-shock flow. At 0.8 million years, its bound mass drops to about 100 times less than that of the two rotating cases. There is no resolvable material left surrounding the formed star. For cases R1 and R2, the bound mass drops at a much slower rate because of the disk. From figure 6.4(d), we observe that if the wind is turned off prior to 0.7 million years, the surviving disk will have a mass greater than $10^{-3}M_\odot$, giving the mass of the whole system $1.001M_\odot$, close to the Solar System. Therefore we conclude that it is possible to obtain at least a $1.0014M_\odot$ star plus protoplanetary disk system from such a triggering mechanism given our physically reasonable choice of initial conditions.

To connect our disk survivability results with previous work, we follow Chevalier (2000) and estimate the erosion radius $r_e(t)$ of the disk from $\rho_d(t)\sqrt{2GM_*/r_e(t)} = \rho_w v_w$, where ρ_w and v_w are the density and velocity of the post-shock wind and $\rho_d(t)$ is the density of the disk. Material at radii $r > r_e(t)$ cannot survive in the disk assuming that the wind momentum is fully transferred to the disk. Any disk surviving at a given time must have $r_d(t) < r_e(t)$. For our simulations we have $\rho_d \approx 10^{-18}g/cc$, $\rho_w = 3.6 \times 10^{-22}g/cc$, $M_* \approx M_\odot$ and $v_w = 3km/s$ at the end of our simulations thus we can verify that $r_d \ll r_e$. Although this is a necessary property that a surviving disc must have at the end of the simulation, the condition evaluated at the *initial time* of disk formation is not sufficient to assess its long term survivability because it does not account for the accumulated influence of the wind. Even a low density

wind impinging over long enough times could in principle ablate the disk. However our disk survival is also in agreement with the study by Ouellette et al (2007), who found that pre-existing disks can survive ablation from the full exposure to supernova driven shock. Such survival can only result if the drag of the disk on the wind is inefficient. Indeed Ouellette et al (2007) find that a high pressure region and reverse shock formers upstream of the disk surface and deflects the flow around the disk leaving it intact. The result is that the wind-disk interaction is ineffective at disk ablation.

6.5 Concluding Remarks

Using AMR numerical simulations, we have followed the interaction between shocks of different Mach numbers and self-gravitating clouds, with and without initial rotation. In each case we followed the evolution of the interaction to study collapse of the cloud, formation of a star, and post-shock evolution as the wind continues to interact with the collapsed cloud. Our studies have carried out the shock-cloud interaction to longer times than have been previously studied. Our focus has been on the extent to which the variation in Mach number and the presence of rotation (at 10% the escape speed) affects star formation, the post-collapse circumstellar bound mass, and the mixing of blast wave material with the cloud. In all three cases that we studied, the interaction proceeds in three phases. First the shock compresses the cloud enough to form a star at the core. Then some cloud material gets ablated and unbound from the star. Finally, some material remains bound to the star and continues to evolve as it is exposed to the post-shock flow. The star formation from the shock induced collapse is robust in all cases whether rotating or not. The mass of the star formed in the initial collapse phase is also comparable in the rotating and non-rotating cases but slightly larger in the non-rotating case since the rotation makes the total mass less bound than for the non-rotating case. However the shock Mach number affects the asymptotic stellar mass even more than the rotation: the higher the Mach number, the less the stellar mass at the end of the simulation.

For the case of rotating clouds, bound circumstellar disks form around the newly

formed stars. Even though the disks are exposed to a continuous stellar wind for throughout the long duration of our simulations, the disk survives this long duration of wind erosion. Because the net momentum from the wind impinging on the disk is substantial, the survival of the disk implies that the drag on the wind by the disk is small, leading to inefficient conversion of the full wind momentum to disk ablation flow. Overall, the asymptotic disk mass of around $10^{-3}M_{\odot}$ given our $1 M_{\odot}$ initial cloud, is achieved when the wind duration at 0.7 million years.

For the question of mixing, we find that the dominant influence on the mixing ratio of blast wave to bound cloud material is the Mach number of the initial shock. The higher the Mach number, the higher the mixing ratio. The mixing ratio is relatively insensitive to the rotation. We note however that rotation can lead to disk formation which subsequently increases the cross section of the bound mass around the star and that can favor extra trapping of incoming wind material (when comparisons are made at a given Mach number with and without rotation).

Based on previous studies of Boss and collaborators that explored the relation between SLRI mixing and incident shock mach numbers, the simulations we present here (with $M = 1.5$ or 3) are not high enough to yield sufficient injection of material to account for observed SLRI abundences. Given the earlier work we would need Mach numbers in the range of 10 to 20 and we leave a fuller exploration of parameter space to a future work. The simulation results presented here however do provide a general understanding to the long term evolutionary mechanisms of TSF including the effects rotation.

Chapter 7

Resistive Shock-clump interaction and its Lab Astrophysics Implication

7.1 Introduction

In the National Laser User Facility (NLUF) project, we conduct experiments to run shocks over target (SiO_2) embedded in room temperature ambient (Argon), and study the X-ray projection image of the resulting flow pattern. The goal of the project is to resolve on the experimental basis the shocked-behavior of clumps that can be commonly found in supernova remnants, stellar jets and YSOs. As discussed in chapter 5, it is often the case that the clumps in such objects contain non-negligible magnetic field. Following Jones et al 1996, we have studied the more realistic situation in chapter 5 where the magnetic field is contained inside the clumps and possess complicated geometry. As a first cut for the lab effort, we design experiments with uniform magnetic field. These experiments provide direct verification for numerical results of shock-clump interaction dated back to the 1980s, and can be used to contrast observed behaviors of such regions such as HH1.

The general model for the shock-clump interaction as predicted in many previous papers such as the time scale for Rayleigh-Taylor instability and Kelvin-Helmholz

instability (Jones et al 1996), the compression ratio for magnetized clumps (Li et al 2013), are expected to be measurable and compared with. One of the major differences between realistic and laboratory astrophysical is the fact that in the realistic astrophysical environment, the magnetic Reynolds number $R_m = VL/\eta$ is usually large due to the enormous length scale of the astrophysical objects. In the lab environment, however, the flow speed V can be produced to mimic the realistic heterogeneous flow by adjusting the radiation pressure from the Omega laser. The magnetic diffusivity is usually smaller in the lab environment depending on the ambient and target density, as $\eta \propto n_e T^{-3/2}$, the temperature is usually comparable, but the electron number density is 40 times greater in an experiment using Argon ambient compared to realistic ionized hydrogen. The most important difference comes from the flow length scale L which takes on the order of parsecs for the realistic astrophysical objects, but only on the scale of mm for the lab experiments. Therefore, R_m for the experiment is likely 10^{18} times smaller than that of the realistic value. While the latter may be very large so that it can be entirely ignored, R_m may not be big enough to be ignored in the lab astrophysics. One of the question for the experiment design, is then to ask at what R_m value does the shock-clump interaction resembles the case of ideal MHD ($R_m = \infty$)? The instrumentation needs to be designed so that such R_m value can be achieved. In this chapter, we introduce the numerical simulations that for the first time captures the behavior of magnetized shock-clump interaction with a non-negligible magnetic Reynolds number. In section 7.2, we present the numerical setup. In section ??, we discuss the results from simulations where R_m is held constant. In section ??, we present the simulation results where R_m is taking Spitzer value from the relation $\eta \propto n_e T^{-3/2}$.

7.2 Initial Setup

In the experiment, we choose Argon ambient and SiO₂ target both at room temperature. In the numerical simulations, we change the temperature of SiO₂ so that the pressure equilibrium holds between the ambient and the target. We present two sets of simulations. The simulation box is three-dimensional, with an effective resolution

of 64 zones across one clump radius.

(1) Constant magnetic Reynolds number with no radiation heating. This setting allows us to test the effect of magnetic diffusion on the shocked behavior under different magnetic Reynolds number. Recall that magnetic Reynolds number $R_m = VL/\eta$ where V and L are the velocity and length scales of the flow, η is the magnetic diffusivity. Taking V and L to be the shock velocity and the diameter of the target, we apply constant η in our simulation so that we can manually vary the R_m by changing the numerical η . We investigate the cases ranging from $R_m = \infty$ to $R_m = 100$. It is worth mentioning that although the parameter regime of $R_m \sim 1$ is of great interest as the magnetic diffusion time scale becomes comparable to the hydrodynamic time scale, the AstroBEAR code implements explicit resistivity solver which relies on operator splitting - we repeatedly solve the induction equation at each hydrodynamic time step, only taking time step $t \propto R_m$. Therefore dropping R_m to 1 would result in an unpractically small time step. Such difficulty can be overcome by implementing implicit resistive solver, which causes a side effect - we now need to enforce the divergence free condition for the magnetic field after each resistivity time step. The resistive MHD solver in AstroBEAR is discussed in detail in section 2.4. We present the results from these simulations in section ??.

(2) Realistic resistivity that depends on the Spitzer value. The Spitzer resistivity is discussed in section ?. In the experiment, the laser beam irradiates the horn to produce a blast wave travelling through the cavity and shocks the target. Such laser also creates ablation of the horn thus produces intense ablation and heating that can change the temperature of the cavity. This radiative heating is non-negligible as it can significantly increase the conductivity of the ambient plasma, thus lowering the plasma resistivity. In order to accurately simulate the temperature profile at the time when shock hits the target, our group has run radiative hydrodynamic simulation to predict the radiation heating (Peter Graham et al). We then import the data from the radiative hydrodynamic simulation to AstroBEAR and create a temperature profile shown in figure 7.1(b). The temperature is about 0.026 eV in the ambient (room temperature), 0.0012 eV in the target initially, 0.026 - 0.8 eV in the ambient, 0.0012 - 0.3 eV in the target after preheated by radiation). The Spitzer resistivity has a

floor temperature: any temperature below 0.26 eV (3000 K), is treated as 0.26 eV when calculating resistivity. This choice is purely out of numerical concern: if the temperature drops too low, the resistive time step can become too small to track: from section 2.4, we know that $\Delta t \propto T^{-3/2}$. This implies that the magnetic diffusion inside the target is always treated as if the target is heated by the radiation. Such approximation may not be valid in the real experiment as it is important to measure the magnetic diffusion before the preheating.

The magnetic field is on the direction vertical to the shock normal. In the experiment, the magnetic β can be suppressed to around 10 by careful instrumentation. In the numerical simulations below, we assume $\beta = 4$ universally. We present the simulation results in section ??.

7.3 Results for Constant Magnetic Reynolds Number

For the case of constant magnetic Reynolds number, the magnetic diffusivity is computed from R_m . We study the three cases where $R_m = 100$, $R_m = 1000$ and $R_m = \infty$ for both horizontal (magnetic field parallel to the shock normal) and vertical (magnetic field perpendicular to the shock normal) field orientations. Figure 7.2 shows the horizontal field case with two-dimensional cut through the center of the simulation box, at 3 clump crushing time (defined in the same fashion as equation 5.3).

For horizontal magnetic field case, Jones et al 1996 predicts a streamlining effect along the clump surface due to the magnetic field tension suppressing the Kelvin-Helmholtz instability. Another significant difference for the magnetized case is the “magnetic rope” at the back of the clump facing downstream where field strength is amplified because of the converging flow downstream. This magnetic rope creates a thread-shaped density cavity, which is visible in the $R_m = \infty$ ideal MHD case in figure 7.2 as the dark blue thread-shaped feature in the density map. The horizontal magnetic field cannot suppress the Rayleigh-Taylor instability thus the head of the clump facing upstream is still susceptible to shock erosion even when the field is

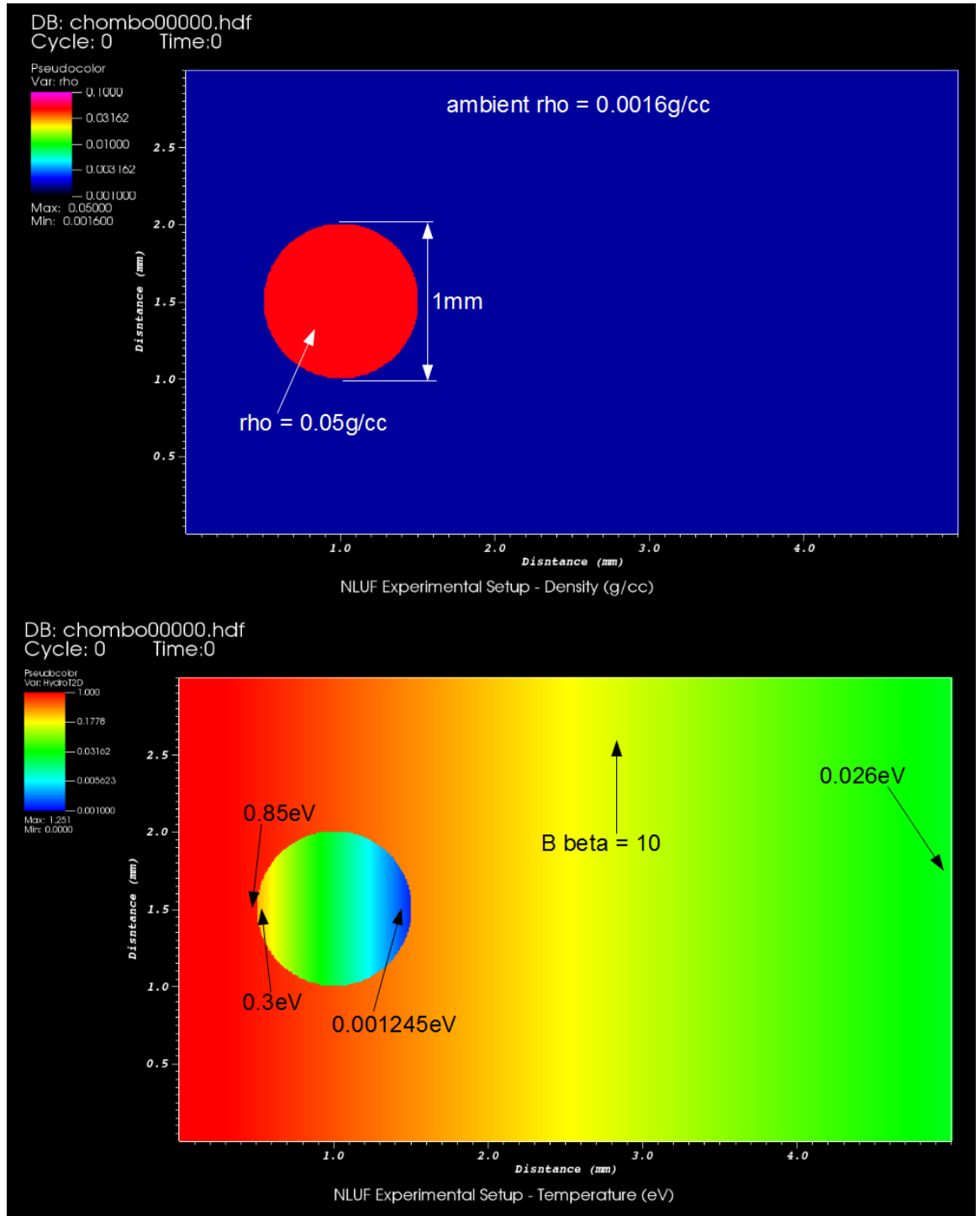


Figure 7.1 Initial setup for shock-clump interaction with Spitzer resistivity. (a) density distribution, (b) temperature distribution with radiation preheating.

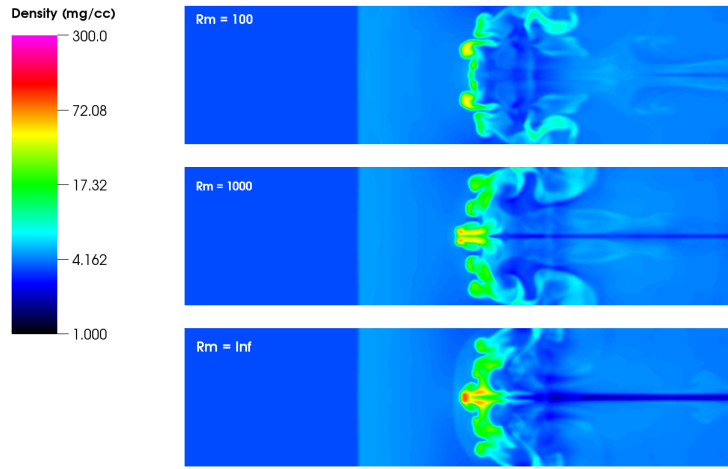


Figure 7.2 Shocked behavior of the target with horizontal magnetic field at different magnetic Reynolds number R_m as marked.

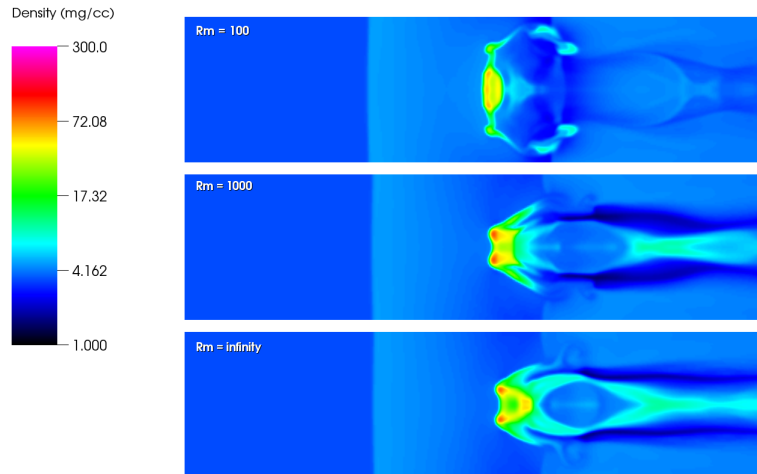


Figure 7.3 Shocked behavior of the target with vertical magnetic field at different magnetic Reynolds number R_m as marked.

strong. In figure 7.2, we observe that erosion happens at the head of the clump facing upstream in all cases.

One of the important features in figure 7.2 is that the profile of the clump remnant of the $R_m = 100$ simulation at $3t_{cc}$ is similar to that of Jones et al 1994, the hydrodynamic cases. This indicates that for parameter regime $R_m \leq 50$, it is impossible to distinguish the magnetized case with the non-magnetized case: the magnetic diffusion is strong enough so that the streamlining effect is diminished to be almost not noticeable. It is therefore important to suppress the magnetic diffusion to achieve $R_m > 100$ during instrumentation.

We next observe that the profile of the clump remnant of the $R_m = 1000$ simulation is similar to that of the $R_m = \infty$ case, i.e. the ideal MHD case. This indicates that for the parameter regime $R_m \geq 1000$, we can treat the experiment as ideal MHD. This observation implies that for maximum magnetic field effects, we need to suppress the magnetic diffusion to achieve $R_m \geq 1000$ for the horizontal field experiment.

Figure 7.3 shows the density cut-through of the vertical magnetic field simulation at $3t_{cc}$ under different magnetic Reynolds number. For the vertical magnetic field case, Jones et al 1996 predicts strong amplification of magnetic energy due to stretching along the clump profile. This amplification creates a “shock absorber” encompassing the clump, preventing it from shock erosion. The clump remnant in this case is much more confined vertically compared to the non-magnetized and the horizontal field cases. With vertical magnetic field, both the Kelvin-Helmholtz instability and the Rayleigh-Taylor instability are suppressed, as the field compression and stretching at the head of the clump facing upstream creates significant magnetic energy amplification, while at the edges of the clump, the field amplification is mainly due to stretching.

Comparing the top panel with that of Jones et al 1994, we find that similar to the horizontal field case, for $R_m \leq 100$, it is difficult to distinguish non-magnetized with magnetized environment by comparing the downstream flow: the clump remnant expands vertically, and creates tails at the edge of the clump, producing KH instability patterns. Note that however, the core of the clump remnant remains relatively intact compared to the non-magnetized case for $R_m = 100$. This indicates that the head of

the clump facing upstream is protected against RT instability for $R_m = 100$. Indeed, although the stretching effect is decreased under resistivity, the field compression at the head of the clump is still significant enough to create a “buffer” to reduce shock erosion. The condition for this to happen is that the shock needs to be fast enough so that the field it brings to the buffer zone outweighs the field leaving the buffer zone due to diffusion. We conclude that for $R_m = 100$ with vertical magnetic field, it is possible to observe the difference between non-magnetized and magnetized cases, by observing the spread of the core of the clump remnant.

In the middle and bottom panel of figure 7.3, we observe that when $R_m \geq 1000$, the resistive MHD result resembles the ideal MHD result. The stretching at the edge of the clump is strong enough such that the KH tail produced in the top panel of figure 7.3 is suppressed. This result is consistent with the horizontal field case: to observe differences in the downstream flow pattern, it is required to achieve $R_m \geq 1000$.

7.4 Results for Realistic Resistivity

In the previous section, we have investigated the effect of constant R_m , and established two key results: (1) In both cases of magnetic field orientation, the parameter regime for the resistive MHD shock-clump interaction to resemble that of non-magnetized case at downstream is $R_m \leq 100$; to obtain downstream flow pattern comparable to ideal MHD, we require $R_m \geq 1000$. (2) In the vertical magnetic field case, it is possible to distinguish the resistive MHD case from the pure hydrodynamical case even when $R_m = 100$, by looking at the core of the clump remnant: the MHD case exhibits significantly less spread.

In the experiment, however, R_m is not a constant, but depends on flow density and temperature via expression of conductivity: $\sigma = F \ln \Lambda n_e T^{3/2}$, where F is the shielding factor that is usually around unity, $\ln \Lambda$ is the Coulomb Logarithm, that can be fitted as a function of density and temperature. The magnetic diffusivity that we feed into the Ampere’s law is therefore $\eta = 4\pi c/\sigma$. As the magnetic diffusivity varies according to $T^{-3/2}$, it is crucial to resolve the correct temperature profile throughout the simulation. Using the radiation preheating temperature profile introduced in sec-

tion 7.2, we conduct resistive MHD simulations with Spitzer resistivity with varying magnetic β . The results are shown in figure 7.4.

We first observe that the top panel resembles the middle panel: with Spitzer resistivity, $\beta = 10$ magnetic field does not significantly change the flow pattern. This result is important as it gives us direct guidance as for how strong the uniform field needs to be so that the MHD effect can be observable: magnetic field weaker than $\beta = 10$ cannot be observed by examining the density map.

Next, we find that the $\beta = 1$ case shows differences at the head of the clump facing upstream. Most noticeably, there are significantly less RT rolls, resulting in a much smoother profile compared to the top and middle panel. Each of the RT rolls has a length scale of around $0.1mm$. We therefore conclude that under Spitzer resistivity, in order to distinguish the $\beta = 1$ with the non-magnetized case, we need to be able to resolve flow features $\leq 0.1mm$ at the head of the clump. This conclusion provides clear direction for the instrumentation.

7.5 Concluding Remarks

Through the resistive MHD simulations, we demonstrated that AstroBEAR can be used to assist the instrumentation design of laboratory astrophysics. The pioneering NLUF project that is set to probe the shock-clump interaction problem in the lab setting has challenges that have never been considered before. In this chapter, we discovered that although it is usually reasonable to assume ideal MHD for realistic astrophysics objects, in the lab environment, resistivity cannot be ignored in general due to small length scales.

From the two sets of simulations - one with fixed magnetic β and varying magnetic Reynolds number R_m , the other with Spitzer resistivity and varying magnetic β . We derived three useful conclusions that can be used to guide the experiment design.

(1) For constant R_m , the parameter regime that the magnetized from the non-magnetized downstream flow pattern become identical is $R_m \leq 100$. The parameter regime where resistive MHD resembles ideal MHD is $R_m \geq 1000$.

(2) It is possible to distinguish the magnetized case from the non-magnetized if

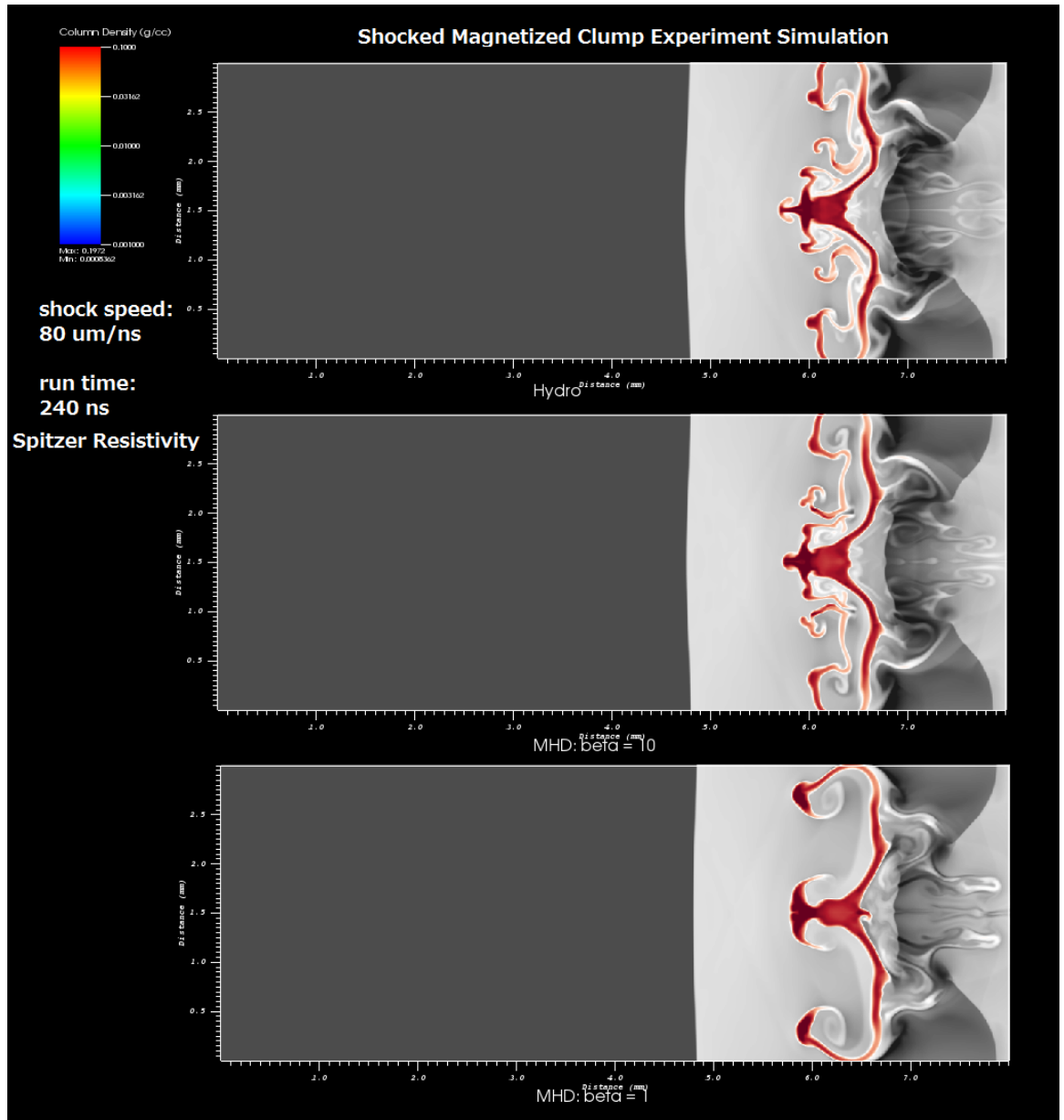


Figure 7.4 Shocked behavior of the target with vertical magnetic field and Spitzer resistivity at different magnetic β .

the magnetic field is vertical even for low R_m ($R_m \leq 100$). We need to observe the core of the clump remnant and measure the vertical spread: the magnetized case has considerably less spread even under strong magnetic diffusion.

(3) With Spitzer resistivity, the radiation preheating from the horrum is crucial in raising the temperature inside the container and therefore lowering the resistivity. For strong magnetic field case ($\beta = 1$), it is possible to observe the effect of the magnetic field on the shocked dynamics by probing the instability pattern at the head of the clump: the magnetized case has considerably less RT features compared to the non-magnetized. The spatial resolution for such detection is required to be under $0.1mm$.

Reader may wonder whether there is other ways to detect the dynamic effect of magnetic field on plasma in a lab environment. Figure 7.5 shows the alternative setting in the NLUF project where we probe the shock-wire interaction. A strong current (about $20A$ at the wire surface) runs through the wire and produces a toroidal magnetic field. Compared to the non-magnetized case, we observe magnetic “buffer” between the bow shock and the wire surface. The thickness of this buffer zone is directly measurable in the experiment, and can be theoretically calculated through pressure equilibrium condition at the stagnation point. Such design also provides excellent example of theory verification, and is summarized in another NLUF project related paper Andy et al 2014.

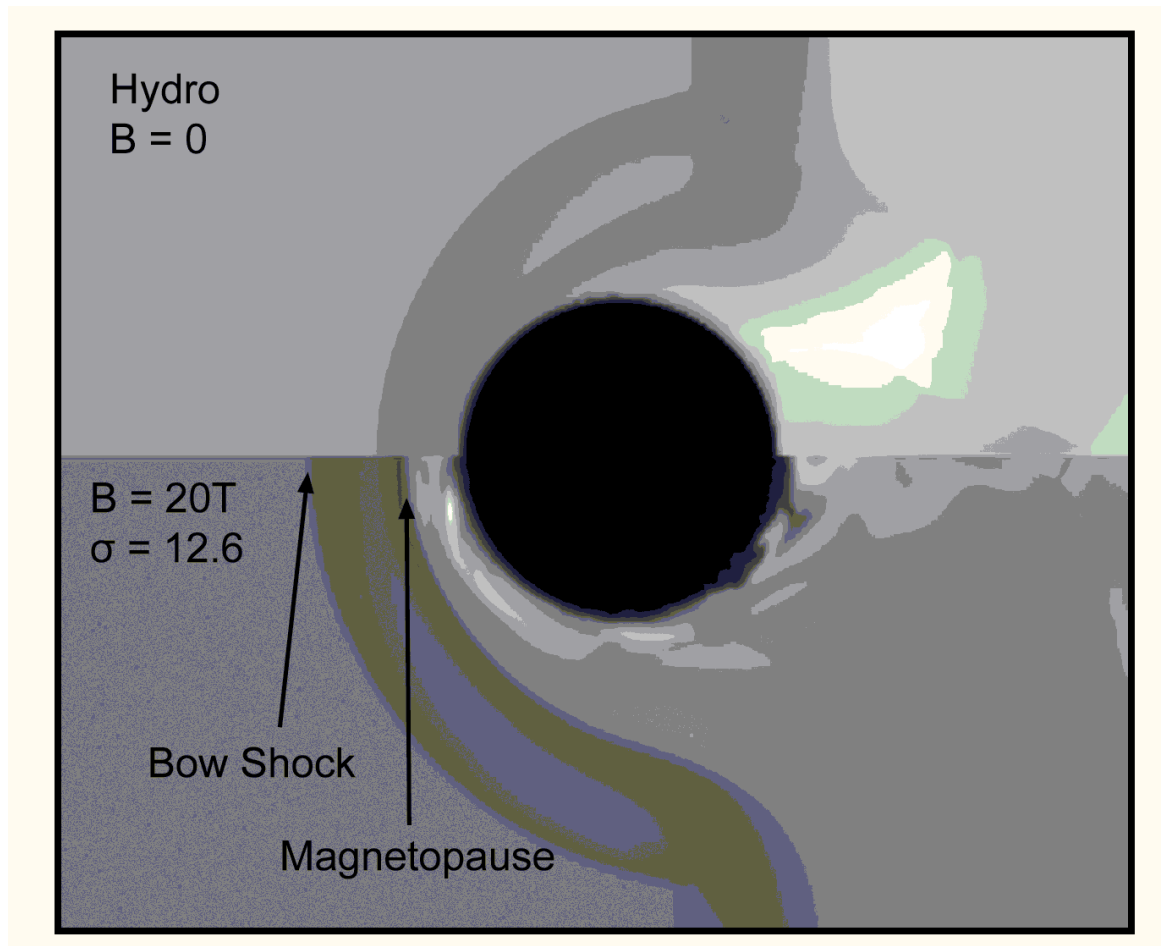


Figure 7.5 Shocked behavior of wire (top down). The wire has 20A surface current running out of the plane. This produces a toroidal magnetic field around 20T at the wire surface. Top: non-magnetized; bottom: magnetized. The magneto-pause is caused by the shifting of the stagnation point by magnetic pressure.

Chapter 8

Summary

In this thesis, we have introduced AstroBEAR, the parallel Eulerian MHD code with multiphysics capabilities, the numerical schemes of some of its most important multiphysics solvers as well as tests, and four interstellar heterogeneous flow problems through AstroBEAR simulations. In this chapter, we summarize what we have learned through these results, and point out future research interests.

8.1 Numerics

AstroBEAR is a grid-based Eulerian code that solves ideal MHD equations. It implements multiple exact and approximate Riemann solvers, as well as a variety of reconstruction schemes. It uses the emf and constrained transport scheme to treat the divergence free magnetic field. AstroBEAR implements load balancing scheme as well as multithreading in order to achieve ideal performance on modern computing architectures. Recent performance tests of AstroBEAR 2.0 has shown excellent scaling result up to tens of thousands of processors based on both weak and strong scaling idioms.

AstroBEAR uses operator splitting to treat its multiphysics components. Under operator splitting, when we take a time step Δt , we first solve the ideal MHD equations for Δt , then we take the physics quantities output from ideal MHD and feed them into the multiphysics solver to evolve another step of Δt . The net effect is that

both MHD and multiphysics evolves for Δt , thus approximating the case in which both solvers are intertwined. It should be pointed out that it is possible to modify the MHD solver such that multiphysics components are built in from the start (Sharma et al 2012). Such solver is usually called an unsplit solver. Intuitively, operator splitting is a simpler though more artificial approach. Certain solvers may raise numerical issues when treated in the splitted fashion, such as the magnetic field: the MHD solver guarantees the divergence free condition by using constrained transport, however, the splitted multiphysics solver is likely a linear system solver thus does not provide such guarantee. When treating multiphysics processes involving magnetic field, one need to explicitly make sure the multiphysics component is on its own divergence free, which usually requires additional numerical mechanisms. On contrary, an unsplit solver always provides multiphysics with divergence free magnetic field as constrained transport can act on both MHD and multiphysics directly. Such unsplit solver may be of interest in the future from both theoretical and application point of view.

The first component we introduced is the implicit heat conduction solver. Through operator-splitting, we solve the following equation:

$$\partial E / \partial t = \nabla \cdot (-\kappa_{\parallel} (\nabla T)_{\parallel}), \quad (8.1)$$

where E can be converted to a linear function of T assuming ideal gas. Thus we have to solve a linear system if κ is constant throughout the grid. The linear system is solved by linear solver package HYPRE. When κ takes the Spitzer value, i.e., a function of T as $\kappa \propto T^{5/2}$, we linearize equation 8.1 and use Crank-Nicholssen scheme. We have introduced the magneto-thermal instability in section 3.1 and verified that the MTI growth rate matches the theoretical value.

The self gravity component is solved in a similar fashion. We solve the poisson equation:

$$\nabla^2 \phi = 4\pi G \rho \quad (8.2)$$

using HYPRE. ϕ is then fed into the next MHD time step to calculate the external force due to gravity as $\rho \phi$. In section 3.2, we used the test from Truelove et al 1994 to verify the collapse rate due to the gas self gravity is correct.

The resistivity component is arguably the most complicated as we are trying to obtain a diffusion of magnetic field which in itself does not preserve divergence numerically. The strategy we adopted is to compute the diffusion current from the existing magnetic field using Ampere’s law:

$$\mathbf{J} = \eta \nabla \times \mathbf{B} \quad (8.3)$$

We then solve the diffused field using:

$$\frac{\partial \mathbf{B}}{\partial t} = \nabla \times \mathbf{J} \quad (8.4)$$

When explicitly solving equation 8.4, we do not have to worry about divergence free condition as the curl of any vector field is inherently divergence free. In section 3.3, we used the Sweet-Parker box model to test the explicit resistivity solver, and found that the velocity of the outflow generated from a resistivity hot spot matches the theoretical value.

Notice that the operator-splitting method introduced here does not explore the numerical difference when applying different operators at different times, as most of the physics we discuss throughout the thesis have been focusing on one type of multiphysics at a time. However, such ordering may be crucial when combining several multiphysics processes into one run. For instance, when combining magnetized thermal conduction with resistivity, there is a difference if one applies the thermal conduction operator or the resistivity operator first during each time step: diffusing the magnetic field first leads to a different field geometry and therefore different temperature distribution for the next hydrodynamic timestep. Intuitively, one may randomize the order of operator application for each time step thus even out the difference during a simulation which likely requires thousands of time steps to complete. The numerical effect of such randomization is not fully explored in the literature, and may lead to new discovery in the numerical front. Such treatment can also benefit the future scientific projects directly as it may be able to render more realistic solutions when multiphysics processes are combined.

8.2 Magnetic Field Regulated Heat Conduction Through Hot-cold Interfaces

In chapter 4, we have investigated the problem of heat transfer in regions of initially arbitrarily tangled magnetic fields in laminar high β MHD flows using simulation results of AstroBEAR code with anisotropic heat conduction. Three conclusions stand out:

(1) Hot and cold regions initially separated by a tangled field region with locally confined field loops may still evolve to incur heat transfer. The local redistribution of fluid elements bend the field lines and lead to magnetic reconnection that can eventually connect the hot and cold regions on the two sides. (2) The temperature gradient through such a penetrated tangled field region tends to reach a steady state that depends on the energy difference between the hot and cold reservoirs on the two ends. (3) equation 4.9, a measure of the initial field tangle, is a good predictor of the ultimate heat transfer efficiencies across the interface for a wide range of R .

A basic limitation of our simulations is that they are 2-D. A 3-D version of this study would be of interest as the field would then have finite scales in the third dimension possibly allowing channels for heat transfer excluded in 2-D. We have also not considered the effects of cooling in our simulations. The absence of cross field diffusion is also not realistic in our parameter regime. Future simulations should include both the diffusion parallel and perpendicular to the field.

Future directions of analysis could also include a multi-mode study, which investigates the effect of the spatial spectrum of the magnetic field distribution on the heat transfer efficiency. When there are multiple modes or a spectrum is continuous, it would be useful to predict how the efficiency would depend on the spectrum. In this context, a more detailed comparison of heat transfer in initially laminar versus initially turbulent systems would be of interest.

8.3 Shock-clump interaction with contained magnetic field

We have studied the evolution of clumps with initially self-contained magnetic fields subject to interaction with a strong shock using both numerical simulations and analytic theory. Our results show a new variety of features compared to previous work on shock-clump interactions with magnetic fields, which considered only cases in which the field threading the clumps was anchored externally [Jones et al (1996), Gregori et al (2000)].

We find that the evolution of the total magnetic energy and kinetic energy of clumps depends primarily on the relative strength of the self-contained magnetic field, the incoming supersonic bulk kinetic energy (characterized by the μ parameter) and the geometry of the magnetic field (characterized by the η and α parameters). We identified two phases in the clump evolution that we characterized by "compression" and "expansion" phases.

In general, we found strong distinctions in clump evolution depending on the relative fraction of field in the clump aligned perpendicular to or parallel to the shock normal. This was demonstrated by considering distinct field configurations that we called "toroidal" and "poloidal" and for each case comparing the shock clump interactions when the symmetry axes were aligned with the shock normal and perpendicular to it. The evolution of the clump magnetic fields seen in our simulations can be described by the mathematical model culminating in equation 5.31 during its compression phase.

The kinetic energy transfer from the supersonic flow to the clumps is similar in the compression phase for all of our cases considered but develop differences in the expansion phase depending on the initial field geometry and orientation, which in turn determines how much field amplification occurs in the compression phase. The evolution of the clump in the expansion phase depends on whether the shock or the magnetic field is dominant at the end of the compression phase.

For the wind-clump material mixing, we found that the more the initial field

is aligned perpendicular to the shock normal, the better the clump can deflect the flow around the clump and the less effective the mixing. Equivalently, the better aligned the field is with the shock normal, the more effective the clump material gets penetrated by the incoming supersonic flow, gains kinetic energy in expansion, and enhances mixing.

These simulations may provide morphological links to astrophysical clumpy environments. In our presented study, we use $150a.u.$ clumps that are typical for young star objects (YSO). However, we also put emphasis on “weakly cooling” condition that the cooling length as indicated by equation 5.7 is not too small compared to the clump radius. For clumps with much higher clump density, the ratio of clump radius to cooling length χ_* can be greatly increased. χ_* can also increase when one tries to scale the simulations to globules that are much larger in size. Therefore in order to gain full understanding of the studied subject, numerical studies that are placed in the parameter regime of “strongly cooling”, where χ_* is several orders of magnitude greater than its current value, are necessary in the future. Future study may also include more realistic radiative cooling using more recently studied emission lines [Wolfire et al (1994)] and equilibrium heating [van Loo et al (2010)], more realistic internal field geometry, for instance, random field; more realistic multi-physical processes such as thermal conduction, resistivity; and more sophisticated mathematical model.

8.4 Triggered Star Formation

Triggered star formation, where an otherwise stable clump collapses because of the compression of an incoming shock, can be used to explain the simultaneous collapse and injection of exotic elements during star formation. Observational evidences for triggered star formation includes Eta Carinae and Cygnus Loop where star forming sites are found tracing a bow shock structure. Because of the higher-than-expected SLRI abundance in the Solar System (10^{-3} according to Imamura et al 2010), one may suspect that shock triggering is the mechanism from which the Solar System is formed, as it is one of the most efficient way to mix the material processed from a supernova

blast wave into the system. One of the key implication is that through numerical modeling, the condition of the triggering shock can be worked out through observable parameters such as dilution ratio and mass. Boss et al 2010 and subsequently Boss et al 2012 conducted numerical simulations to estimate the shock speed needed to trigger a M_{\odot} clump with desired dilution ratio (manifested as the injection efficiency). However, they did not carry out the simulations till the time when a star and an accretion disc is formed due to limitations of numerics.

In chapter 6, we introduced the AstroBEAR simulations with sink particle that for the first time track the entire evolution pattern of shock triggered star formation, and studied the formation and survivability of accretion disc through initial clump rotation. Our model uses a clump that is similar to that of Boss' as a natural progression from their work. We summarise the results below:

(1) By inspecting the sink particle mass, we can directly measure the star mass from the triggered formation. It is concluded that the star reaches an asymptotic mass as the clump material is stripped away by the post-shock wind. The faster the incoming shock, the lower the asymptotic mass and the higher the mixing ratio of the wind material onto the star. The latter observation is in agreement with that of Boss et al 2010.

(2) Bound circumstellar disks form around the newly formed stars, giving initial clump rotation. The disk survivability is similar to that of Ouelette et al 2007: because of the formation of a bow shock around the disk when embedded in the wind, the wind material gets deflected into the downstream and thus does not directly impact the bound mass of the disk: the disk can survive the wind erosion for the entire span of our simulations which is an overestimation compared to realistic supernova blast wave.

One of the drawback of our presented simulations is that the blast wave structure and the shock speed is not realistic. According to Chavalier et al 1986, the blast wave has an inherent structure due to the radiative cooling. It is crucial for the triggered star formation simulations to have correct blast wave structure towards more realistic simulations. By now, no literature has put emphasis on this issue, even in Boss et al 2012 where the effect of shock thickness is explored, the blast wave is still

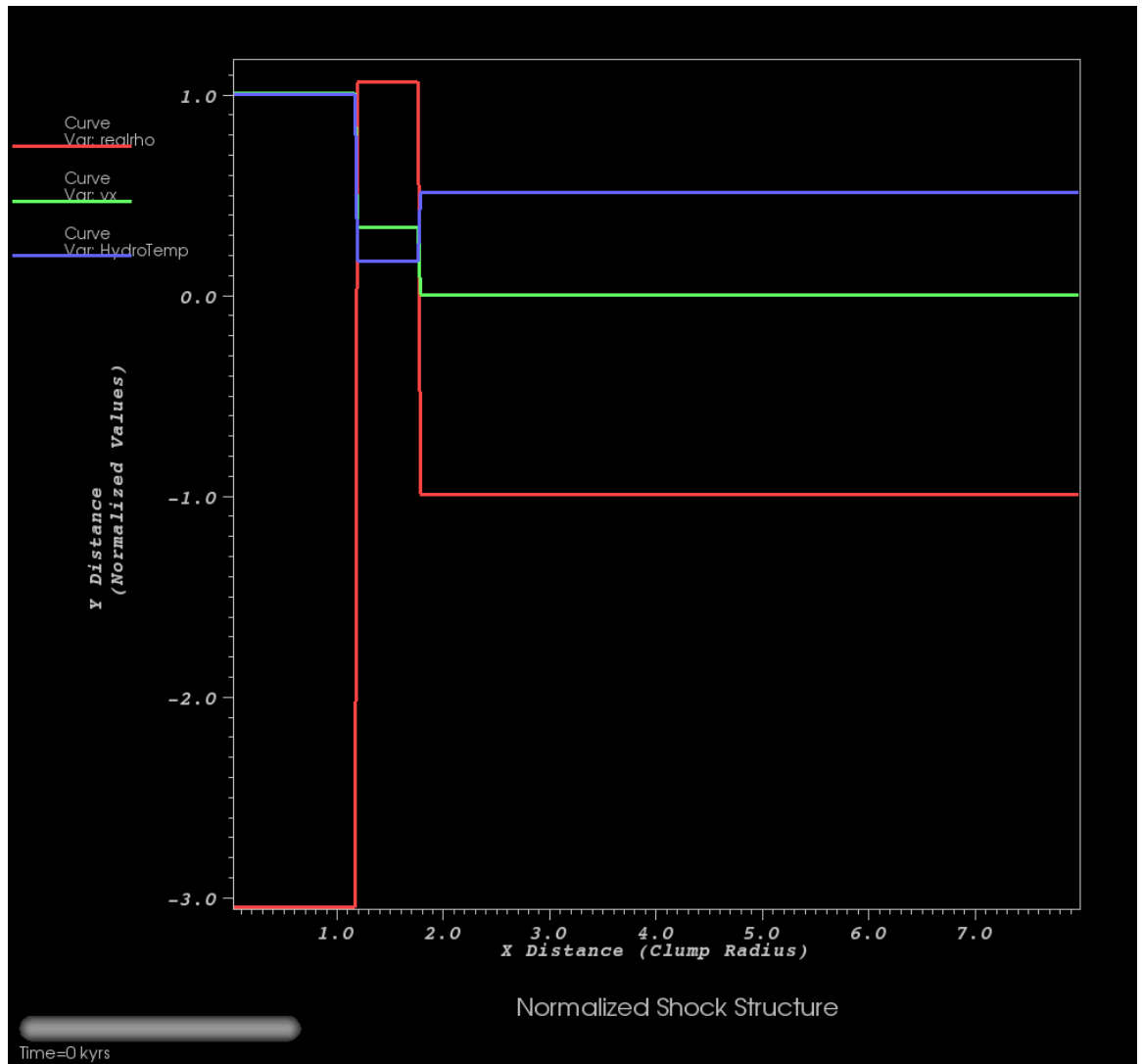


Figure 8.1 Realistic supernova blast wave structure. Red: density; Green: velocity; Blue: temperature.

significantly different than the numerical models of supernova blast. As a next step in the triggered star formation simulation, we adopt the numerical model of supernova blast waves and use it for the next round of investigation. Figure 8.1 plots the blast wave structure adopted from Chavelier et al 1986. The readers can easily observe that the density, temperature and velocity profiles are all significantly different than either the one introduced in chapter 6 or in Boss et al 2010.

Magnetized triggering is briefly presented in chapter 6. The effect of internal magnetic field is demonstrated to be important to the post-formation morphology, and is a key element for the formation of jets. Further numerical simulations in the future will likely explore the various geometric configurations of magnetic field. This direction of study ties back to the study done in chapter 5, and may link some of the findings in shock interaction with magnetized clumps with star formation.

As evidenced by Eta Carinae, triggering can happen on a global scale. It is of great interest on the numerical front to simulate multiple triggering by one single bow shock. Such simulation requires a much greater dynamic range compared to the simulations shown in chapter 6, and requires zoom-in ability so that one can dissect the output from the global simulation and focus on one of the triggering sites. Thanks to the recent advancement in numerics such as AMR and sink particle, we believe such problems can be practically tackled in the near future.

8.5 Resistive Shock-clump interaction

Laboratory astrophysics has seen significant rise of interest over the past 20 years. With better laser and instrumentation technology, people can now build systems that are scalable to astrophysical objects. In chapter 7, we introduced one of such system that is designed to explore the shock-clump interaction problem. The goal of the project is to understand the dynamic effect of magnetic field in such interaction in the lab environment, and thus provide verification to the existing theory and numerics.

In chapter 7, we explored the non-ideal MHD shock-clump interaction because in the experiment, the resistivity cannot be ignored. Such concern raises an issue about scalable lab astrophysics in general: the scalability of the lab astrophysics re-

sults is parameter dependent: some microphysics processes may manifest itself in a completely different way in the lab environment compared to the astrophysics environment. Therefore it is possible to have lab results deviating from the desired model even if all of the dynamic quantities are perfectly scaled. The resistive MHD shock-clump simulations are set to solve two problems regarding the lab design: (1) in what parameter regime can we distinguish the magnetic field effect? (2) in such parameter regime, what flow feature should we observe?

We answered the first question by carrying out a set of simulations with fixed β , but varying R_m . The comparison between different R_m cases gave us clear guidance over the problem of magnetic diffusion: if $R_m \leq 100$, it is impossible to distinguish the downstream flow pattern of non-magnetized cases with that of the magnetized case; if $R_m \geq 1000$, resistive MHD resembles ideal MHD. We also discovered that for vertical field, it is possible to distinguish $R_m = 100$ magnetized case by observing the spread of the head of the clump. These results provide useful clue to solve the instrumentation, but the parameter regime of different R_m values needs to be more thoroughly explored. One of the future project is to build mathematical models as in chapter 5 to derive dimensionless parameters that can characterize the resistive MHD shock-clump interaction. Such models, once verified by the numerical simulations, can provide fast guide towards correct instrumentation design.

The Spitzer resistivity can be used to approximate the realistic situation in the experiment. In chapter 7, we introduced a set of simulations with realistic Spitzer resistivity under varying β . We found that under strong magnetic field, it is only possible to distinguish the magnetized case by observing the fine features of flow at upstream. It is worth noting that such simulations do not take into consideration of the dynamic effect of radiation, which may play an important role in the flow evolution. As the development of AstroBEAR begins to incorporate radiation transfer, we believe that the future lab astrophysics projects can be simulated using an tool equipped with such physics.

8.6 Concluding Remarks

Throughout this thesis, we have introduced a variety of problems related to interstellar heterogeneous flows. It is worth noting that these problems are interconnected through one of their key common properties: the underlying physics is governed by inhomogeneity. In the heating problem of the WBB shell, the magnetic field structure is tangled locally. The local field loops are small enough compared to the length scale of the shell, thus creating clumpy contacting region between the shell and the heat reservoir. Here, we see one of the mechanisms in the interstellar environment that clumps containing tangled magnetic field can be formed. In the shock-clump interaction simulations, we investigated further the shocked behavior of these clumps and derived useful mathematical models that can be used to estimate the dynamic quantities of the clump remnant. We then demonstrated two important applications of the shock-clump interaction model: one with star formation, which can be directly linked to the possible explanation of the Solar System. In those simulations, we have also discovered the importance of contained magnetic field: internal poloidal field leads to stellar jets under triggered star formation. Another important application is in the form of laboratory astrophysics. Heterogeneous flows containing complicated magnetic field structure are found in many lab astrophysics experiments. We introduced one of the leading projects AstroBEAR is involved in that is set to investigate such problem. The problem of interstellar heterogeneous flows is a fascinating subject that is classic among theorists and experimentalists, and yet, as demonstrated by this thesis, still offers abound research opportunities. With the advance of numerical and instrumentation technique, we would like to participate in further progressing this field of research that has a promising future.

Bibliography

- Akashi, M., Soker, N., Behar, E., & Blondin, J. 2007, MNRAS, 375, 137
- Balbus, S. A., & Reynolds, C. S. 2008, ApJ, 681, 65
- Chandran, B. D. G., & Cowley, S. C. 1998, Phys. Rev. Lett., 80, 3077
- Chandran, B. D. G., & Maron, J. L. 2004, ApJ, 602, 170
- Cunningham A. J., Frank A., Varnière P., Mitran S., Jones T. W. 2009, ApJS, 182, 519
- Kastner, J. H., Montez, R., Jr., Balick, B., & De Marco, O. 2008, ApJ, 672, 957
- Maron, J., Chandran, B. D., & Blackman, E. 2004, Phys. Rev. Lett., 92, 045001
- McCourt, M., Parrish, I. J., Sharma, P., Quataert, E. 2011, MNRAS, 413, 1295
- Mikellides, I. G., Tassis, K., & Yorke, H. W. 2011, MNRAS, 410, 2602
- Montez, R., Jr., Kastner, J. H., De Marco, O., & Soker, N. 2005, ApJ, 635, 381
- Narayan, R., & Medvedev, M. V. 2001, ApJ, 562, 129
- Parrish, I. J., & Stone, J. M. 2005, ApJ, 633, 334
- Rechester, A. B., & Rosenbluth, M. N. 1978, Phys. Rev. Lett., 40, 38
- Rosner, R., & Tucker, W. H. 1989, ApJ, 338, 761
- Soker, N. 1994, ApJ, 107, 276

- Steffen, M., Schonberger, D., and Warmuth, A. 2008, *A&A*, 489, 173
- Stone, J. M., & Zweibel, E. G. 2009, *ApJ*, 696, 233
- Stute, M., & Sahai, R. 2006, *ApJ*, 651, 882
- Tao, L. 1995, *MNRAS*, 275, 965
- Tribble, P. C. 1989, *MNRAS*, 238, 1247
- Vlemmings, Wouter H. T., Diamond, P. J., Imai, Hiroshi 2006, *Nature*, 440, 58
- Zhekov, S. A., & Myasnikov, A. V. 1998, *New Astronomy*, 3, 57
- Zhekov, S. A., & Myasnikov, A. V. 2000, *ApJ*, 543, 53
- Zhekov, S. A., & Park Sangwook 2010, *ApJ*, 721, 518
- Zhekov, S. A., & Park Sangwook 2011, *ApJ*, 728, 135
- Cunningham, A.J., Frank, A., Varnière, P., Mitran, S., Jones, T.W. 2009, *ApJS* 182 519
- Dalgano, A., & McCray, R.A. 1972, *ARA&A*, 10, 375
- Fragile, P.C., Anninos, P., Gustafson, K., Murray, S.D. 2005, *ApJ*, 619, 325
- Fragile, P.C., Murray, S.D., Anninos, P., van Breugel, W. 2004, *ApJ*, 604, 74
- Frank, A., Ryu, D., Jones, T.W., Noriega-Crespo, A. 1998, *ApJ*, 494, 79
- Gregori, G., Miniati, F., Ryu, D., Jones, T.W. 2000, *ApJ*, 543, 775
- Jones, T.W., Ryu, D., & Tregillis, I.L. 1996, *ApJ*, 473, 365
- Jun, Byung-Il, Norman, M.L., Stone, J.M. 1995, *ApJ*, 453, 332
- Klein, R.I., McKee, C.F., Colella, P. 1994, *ApJ*, 420, 213
- Klein, R.I., Woods, D.T. 1998, *ApJ*, 497, 777

- Lebedev, S.V., Ciardi, A., Ampleford, D.J., Bland, S.N., Bott, S.C., Chittenden, J.P., Hall, G.N., Rapley, J., Jennings, C.A., Frank, A., Blackman, E.G., Lery, T. 2005, MNRAS, 361, 97
- Li, S., Frank, A., Blackman, E.G. 2012, ApJ, 748, 24
- Lind, K.R., Payne, D.G., Meier, D.L., Blandford, R.D. 1989, ApJ, 344, 89
- Mac Low, M., McKee, C.F., Klein, R.I., Stone, J.M., Norman, M.L. 1994, ApJ, 433, 757
- Mellema, G., Kurk, J.D., Rottgering, H.J.A. 2002, *a*, 395, 13
- Miniati, F., Ryu, D., Ferrara, A., Jones, T.W. 1999, ApJ, 510, 726
- Nakamura, F., McKee, C.F., Klein, R.I., Fisher, R.T. 2006, ApJS, 164, 477
- Orlando, S., Peres, G., Reale, F., Bocchino, F., Rosner, R., Plewa, T., Siegel, A. 2005, A&A, 444, 505
- Orlando, S., Bocchino, F., Reale, F., Peres, G., Pagano, P. 2008, ApJ, 678, 274
- Pittard, J.M., Falle, S.A.E.G., Hartquist, T.W., Dyson, J.E. 2008, MNRAS, 394, 1351
- Poludnenko, A.Y., Frank, A., Blackman, E.G. 2002, ApJ, 576, 832
- Shin, M.S., Stone, J.M., Snyder, G.F. 2008, ApJ, 680, 336
- Stone, J.M., Norman, M.L. 1992 ApJ, 390, 17
- Van Loo, S., Falle, S.A.E.G, Hartquist, T.W. 2010 MNRAS, 406, 1260
- Wolfire, M.G., Churchwell, E. 1994 ApJ, 427, 889
- Yirak, K., Frank, A., Cunningham, A.J. 2010, ApJ, 722, 412

- Baker, A. H., Falgout R. D., Kolev, Tz. V., Yang U. M., 2012, in High Performance Scientific Computing: Algorithms and Applications, eds. Springer, Scaling hypre's Multigrid Solvers to 100,000 Cores, LLNL-JRNL-479591
- Banerjee, R., Pudritz, R. E., Holmes, L., 2004, MNRAS, 355, 248
- Bonnell, I. A., Dobbs, C. L., Robitaille, T. P., Pringle, J. E., 2006, MNRAS, 365, 37
- Boss., A. P., 1995, ApJ, 439, 224
- Boss, A. P., Ipatov, S. I., Keiser, S. A., Myhill, E. A., Vanhala, Harri A. T., 2008, ApJ, 686, 119
- Boss, A. P., Keiser, S. A., Ipatov, S. I., Myhill, E. A., Vanhala, Harri A. T., 2010, ApJ, 708, 1268
- Boss, A. P., Keiser, S. A., 2010, ApJ, 717, 1
- Boss, A. P., Keiser, S. A., 2013, ApJ, 770, 51
- Cameron, A. G. W., Truran, J. W., 1977, Icarus, 30, 447
- Carroll-Nellenback, Jonathan J., Shroyer, Brandon Frank, Adam, Ding, Chen, 2013, J. Comp. Phy., 236 461
- Chevalier, R. A. 2000, ApJ, 538, 151
- Clayton, Donald D., Hartmann, Dieter H., Leising, Mark D., 1993, ApJ, 415, 25
- Cunningham, A.J., Frank, A., Varnière, P., Mitran, S., Jones, T.W., 2009, ApJS, 182 519
- Dhanao, H., Mackey, J., Yates, J., 2014, <http://arxiv.org/abs/1402.1103>
- Federrath, C., Banerjee, R., Clark, P. C., Klessen, R. S., 2010, ApJ, 713, 269
- Foster, P. N., Boss, A. P., 1996, ApJ, 468, 784

- Gritschneder, M., Lin, D. N. C., Murray, S. D., Yin, Q. Z., Gong, M. N., 2012, *ApJ*, 745, 22
- Gong, Hao, Ostriker, Eve C., 2013, *ApJS*, 204, 8
- Hillenbrand, L.A., 1997, *AJ*, 113, 1733
- Jones, T. W., Ryu, Dongsu, Tregillis, I. L., 1996, *ApJ*, 473, 365
- Kaminski, E., Frank, A., Carroll-Nellenback, Jonathan J., Myers, P., submitted to *ApJ*, <http://arxiv.org/abs/1401.5064>
- Kothes, R., Uyaniker, B., Pineault, S., 2001, *ApJ*, 560, 236
- Krumholz, M. R., McKee, C. F., Klein, R. I., 2004, *ApJ*, 611, 399
- Leao, M. R. M., de Gouveia Dal Pino, E. M., Falceta-Goncalves, D., Melioli, C.; Geraissate, F. G., 2009, *MNRAS*, 394, 157
- Li, S., Frank, A., Blackman, E.G., in prep.
- Mac Low, M., McKee, C.F., Klein, R.I., Stone, J.M., Norman, M.L., 1994, *ApJ*, 433, 757
- Ouellette, N., Desch, S. J., Hester, J. J., 2007, *ApJ*, 662, 1268
- Reynolds, R. T., Cassen, P. M., 1979, *Geo. Rev. Lett.*, 6, 121
- Roberts., W. W., 1969, *ApJ*, 158, 123
- Smith, N., Bally, J., & Walborn, N. R. 2010, *MNRAS*, 405, 1153
- Walch, S., Whitworth, A. P., Bisbas, T. G., Wnsch, R., Hubber, D. A., 2013, *MNRAS*, 435, 917
- Vanhala, Harri A. T., Cameron, A. G. W., 1998, *ApJ*, 508, 291
- Vanhala, Harri A. T., Boss, A. P., 2002 *ApJ* 575, 1144

Vaidya, B., Hartquist, T. W., Falle, S. A. E. G., 2013, MNRAS, 433, 1258

van Loo, S., Falle, S. A. E. G., Hartquist, T. W., Moore, T. J. T., 2007, A&A, 471,
213